LLNL-TH-691086

LAWRENCE
LIVERMORE
NATIONAL
LABORATORY

Studies of Positron Generation from Ultraintense Laser-Matter Interactions

G. J. Williams

May 5, 2016

Disclaimer

This document was prepared as an account of work sponsored by an agency of the United States government. Neither the United States government nor Lawrence Livermore National Security, LLC, nor any of their employees makes any warranty, expressed or implied, or assumes any legal liability or responsibility for the accuracy, completeness, or usefulness of any information, apparatus, product, or process disclosed, or represents that its use would not infringe privately owned rights. Reference herein to any specific commercial product, process, or service by trade name, trademark, manufacturer, or otherwise does not necessarily constitute or imply its endorsement, recommendation, or favoring by the United States government or Lawrence Livermore National Security, LLC. The views and opinions of authors expressed herein do not necessarily state or reflect those of the United States government or Lawrence Livermore National Security, LLC, and shall not be used for advertising or product endorsement purposes.

This work performed under the auspices of the U.S. Department of Energy by Lawrence Livermore National Laboratory under Contract DE-AC52-07NA27344.

Studies of Positron Generation from Ultraintense Laser-Matter Interactions

By

Gerald Jackson Williams

B.A. (St. Olaf College) 2008
M.S. (DePaul University) 2010

DISSERTATION

Submitted in partial satisfaction of the requirements for the degree of

DOCTOR OF PHILOSOPHY

in

Applied Science

in the

OFFICE OF GRADUATE STUDIES

of the

UNIVERSITY OF CALIFORNIA

DAVIS

Approved:

Professor Hector A. Baldis, Chair
University of California, Davis

Dr. Hui Chen
Lawrence Livermore National Laboratory

Professor Gregory Miller
University of California, Davis

Committee in Charge

2016

© Gerald Jackson Williams 2016

All Rights Reserved

To Denise, who loves me in spite of rational judgement;

To my mother for passing down her joie de vivre;

To the one sister I like better than the other;

To my father for showing me you can get paid doing what you love;

To the other sister as well.

ACKNOWLEDGEMENTS

As science is never performed in a vacuum, there are many people who have had significant influences on my progression throughout graduate school and have helped to deliver me to this, a postgraduate life. Primarily, I thank Dr. Hui Chen for her endurance in molding me into a physicist, for expecting my best every day, and for never accepting substandard efforts. Thanks to my fellow graduate students, Ed Marley, Shaun Kerr, Alex Steel, and Jaebum Park, all of whom have allowed me to interrupt their work when I needed a break from mine. I would like to thank Michael MacDonald for his valuable suggestions and feedback in preparing this dissertation. Additionally, I thank Prof. Hector Baldis, for taking a chance on me and for the introduction to LLNL.

I had many great discussions with Andy Hazi, Bob Cauble, Tony Link, Brad Pollock, and Riccardo Tommasini as well as my many other colleagues at LLNL and I thank them for their generosity in time and advice. I received exceptional engineering support from Carl Bruns, Rob Costa, Chuck Cadwalader, Ed Magee, and the staff of the Jupiter Laser Facility. I also take this opportunity to thank all of my experimental teammates and P.I.s who let me gain experience from them.

My wife Denise deserves all of my gratitude for keeping me fed, giving me a safe space, and loving me. The dependable encouragement from my family and friends has given me the perseverance to make it through graduate school, and I thank them enormously for that.

Portions of Chapter III are in part reprints of the material contained in the publication: G. J. Williams, B. R. Maddox, Hui Chen, S. Kojima, and M. Millecchia. *Calibration and equivalency analysis of image plate scanners.* Review of Scientific Instruments, 85(11):11E604, 2014. The dissertation author was the primary investigator and author of this paper.

Chapter IV is in part a reprint of the material contained in the publication: G. J.

Williams, B. B. Pollock, F. Albert, Hui Chen, J. Park. *Positron generation using laser-wakefield electron sources*, Physics of Plasmas, 22(10):093115, 2015. The dissertation author was the primary investigator and author of this paper.

Chapter V is in part a reprint of the material contained in the publication: G. J. Williams, D. Barnak, G. Fiksel, A. Hazi, S. Kerr, A. Link, M. J.-E. Manuel, S. Nagel, J. Park, B. B. Pollock, and Hui Chen. *Material dependence of positron generation for mm-scale targets from high intensity laser-matter interactions*, (submitted to Physics of Plasmas). The dissertation author was the primary investigator and author of this paper.

This work was performed under the auspices of the U.S. Department of Energy (DOE) by Lawrence Livermore National Laboratory under Contract No. DE-AC52-07NA27344. This work was funded by the Laboratory Directed Research and Development Program under project tracking codes 12-ERD-062 and by the LLNL Livermore Graduate Scholar Program.

Gerald Jackson Williams
June 2016
Applied Science Engineering

Studies of Positron Generation from Ultraintense Laser-Matter Interactions

ABSTRACT

Laser-produced pair jets possess unique characteristics that offer great potential for their use in laboratory-astrophysics experiments to study energetic phenomenon such as relativistic shock accelerations. High-flux, high-energy positron sources may also be used to study relativistic pair plasmas and useful as novel diagnostic tools for high energy density conditions. Copious amounts of positrons are produced with MeV energies from directly irradiating targets with ultraintense lasers where relativistic electrons, accelerated by the laser field, drive positron-electron pair production. Alternatively, laser wakefield accelerated electrons can produce pairs by the same mechanisms inside a secondary converter target.

This dissertation describes a series of novel experiments that investigate the characteristics and scaling of pair production from ultraintense lasers, which are designed to establish a robust platform for laboratory-based relativistic pair plasmas. Results include a simple power-law scaling to estimate the effective positron yield for elemental targets for any Maxwellian electron source, typical of direct laser-target interactions. To facilitate these measurements, a solenoid electromagnetic coil was constructed to focus emitted particles, increasing the effective collection angle of the detector and enabling the investigation of pair production from thin targets and low-Z materials.

Laser wakefield electron sources were also explored as a compact, high repetition rate platform for the production of high energy pairs with potential applications to the creation of charge-neutral relativistic pair plasmas. Plasma accelerators can produce low-divergence electron beams with energies approaching a GeV at ∼Hz frequencies. It was found that, even for high-energy positrons, energy loss and scattering mechanisms in the target create a fundamental limit to the divergence and energy spectrum of the emitted positrons.

The potential future application of laser-generated pairs was considered by exploring the feasibility of radiographing an imploding inertial confinement fusion capsule at ignition-relevant conditions. For an in-flight areal density of 0.02–0.2 g/cm^2, currently available positron sources can make density and spatial measurements of deuterium-tritium fuel cores where additional complications of full-scale experiments are expected to reduce the measurement sensitivity.

TABLE OF CONTENTS

ACKNOWLEDGEMENTS iii

ABSTRACT v

LIST OF FIGURES viii

LIST OF TABLES x

CHAPTER

I. Introduction 1

1.1 Dissertation Motivation 1
1.2 Summary of Results 4
1.3 Outline 4

II. Physics of Positron-Electron Pair Production 5

2.1 Pair Production 5
  2.1.1 Bremsstrahlung Emission 9
  2.1.2 Pair Production by Photons 11
  2.1.3 Pair Production by Electrons 16
2.2 Electron Acceleration Mechanisms of Ultraintense Lasers 17
  2.2.1 Electron Acceleration in a Laser Field 19
  2.2.2 Ponderomotive Force 21
  2.2.3 Relativistic $\mathbf{J} \times \mathbf{B}$ Mechanism 22
  2.2.4 Laser Wakefield Acceleration (LWFA) 24
2.3 Passage of Particles in Matter 28
2.4 TNSA Positrons 33

III. Experimental Design 39

3.1 Laser Platforms 39
  3.1.1 The Titan Laser 41
  3.1.2 The Callisto Laser 43
  3.1.3 The Omega EP Laser 43

3.2 Diagnostics . . . 44
3.2.1 Image Plate Detector and Scanner Calibration . . . 44
3.2.2 Electron Positron Proton Spectrometer (EPPS) . . . 50
3.2.3 Gamma Crystal Spectrometer (GCS) . . . 55
3.2.4 High Energy Step Filter Spectrometer (HERBI) . . . 58
3.3 Pulsed Power Solenoid Coil . . . 67

IV. Positron Generation from Laser Wakefield Electron Sources . . . 72

4.1 Experimental Conditions of LWFA . . . 73
4.2 Analytic Modeling of LWFA-Produced Positrons . . . 79
4.3 Monte Carlo Modeling of LWFA-Produced Positrons . . . 82
4.3.1 Minimum Achievable Divergences . . . 84
4.3.2 Maximum Achievable Densities . . . 88
4.4 Discussion and Recommendations for Future Experiments . . . 89

V. Target Material Dependence of Positron Generation from Direct Laser-Matter Interactions . . . 91

5.1 Experimental Design . . . 92
5.2 Calculating Particle Trajectories in a Focusing Magnetic Field . . . 94
5.3 Experimental Results . . . 99
5.3.1 Theoretical Expectation of Material Dependent Pair Production Scaling . . . 101
5.3.2 Comparison of Data and Monte Carlo Simulations to Derive an Empirical Scaling Relation . . . 103
5.4 Conclusions . . . 108

VI. Positron Radiography of Ignition-Relevant ICF Capsules . . . 109

6.1 Inertial Confinement Fusion . . . 109
6.2 Positron Radiography of Fuel Capsules . . . 111

VII. Conclusion and Future Work . . . 120

APPENDICES . . . 122

A. Quick References . . . 123
B. Doppler Broadening of Annihilation Radiation . . . 124
C. Uncertainty Propagation for EPPS data . . . 127
D. EPPS Data Analysis Tool . . . 129

BIBLIOGRAPHY . . . 134

LIST OF FIGURES

Figure

2.1 Feynman Diagram for the Trident Pair Production Process 6
2.2 Feynman Diagram for the Bethe-Heitler Process 7
2.3 Bremsstrahlung Cross Section 10
2.4 Cross Section for Pair Production by Photons 12
2.5 Radiation Length of Elemental Materials 13
2.6 Trident vs Bethe-Heitler Pair Yield 17
2.7 Schematic of a Laser Wakefield Accelerator 25
2.8 Electron Stopping in Gold 29
2.9 Photoabsorption Cross Sections for Au 31
2.10 Cartoon of TNSA Mechanism 33
2.11 Density and Field Magnitudes from Ultraintense Laser Matter Interactions 35
2.12 Contribution of TNSA to Positron Spectrum 37
2.13 Control of TNSA Positrons 38
3.1 Janus Amplifier Chain Diagram 40
3.2 Target Area Layout of the Titan Laser 42
3.3 MS Image Plate Sensitivity 46
3.4 GE Image Plate Scanner Sensitivity Function Using Known Source 47
3.5 Determining the Sensitivity Function for a GE Image Plate Scanner 49
3.6 Diagram of Charged Particle Spectrometer (EPPS) 51
3.7 Typical Raw Data from EPPS 52
3.8 Example Analysis of Positron Signal 53
3.9 Typical Electron Spectrum 54
3.10 Geometric Schematic of GCS 56
3.11 Example GCS Data 57
3.12 HERBI Filter Pack Model 59
3.13 Determination of HERBI Channel Mean Energy 61
3.14 Analytic and Modeled HERBI Response Matrix 63
3.15 HERBI Signal and Background Determination 64
3.16 Bremsstrahlung X-ray Spectrum Analysis Using HERBI 65
3.17 Diagram of HERBI Filter Locations 68
3.18 Electromagnetic Coil Construction And Design 69
3.19 Axial Magnetic Field Measurements 70
4.1 Cartoon Schematic of Laser Wakefield Acceleration 73

4.2 Experimental Setup and Focal Spot of the Callisto Laser System 74
4.3 “Low Intensity” LWFA Electron Source 75
4.4 Bootstrap Procedure to Estimate High Intensity Electron Source 76
4.5 Reconstructed “High Intensity” Electron Spectrum 77
4.6 LWFA Electron Source Comparison 78
4.7 Positron Production Using Callisto LFWA Electrons 80
4.8 Positron Beam Profiles and Divergences from LWFA Source 85
4.9 Energy Dependence of Positron Divergence 87
4.10 Time Dependence of Positron Emission 89
5.1 Experimental Setup at the Titan Laser 92
5.2 Reference Electrons and Positron Divergence Measurements 93
5.3 Positron Generation Experimental Setup Using a Collimation Coil 95
5.4 Analytic Particle Trajectories in a Magnetic Lens 97
5.5 Ray Tracing Simulation Demonstrating Realistic Particle Focusing 98
5.6 Dependence of Energy and Divergence on Focusing Condition 99
5.7 Raw Positron Signal with and without a Collimating Magnetic Field 100
5.8 Positron Data and Simulation Results for Material Scan 104
5.9 Positron Yield Scaling For All Elemental Targets 106
5.10 Positron Yield Scaling For Variable Electron Temperatures 107
6.1 Diagram of Positron Radiography for Indirect Drive ICF 111
6.2 ICF Capsule Configurations Throughout the Implosion 113
6.3 Positron Radiographs of Imploded ICF Capsules (Fuel-Only) 115
6.4 Positron Spectrum After Radiographing ICF Capsule 116
6.5 Positron Radiographs of Imploded ICF Capsules (Fuel and Ablator) 118
B.1 Doppler Broadening of Positron Annihilation in a Plasma 126
D.1 Main GUI of EPPS Data Analysis Tool 129
D.2 Metadata GUI of EPPS Data Analysis Tool 130
D.3 Setting Front of Lineout 131
D.4 Cropping Background Lineout Signal 132

LIST OF TABLES

Table

2.1 Physics List for Geant4 32
3.1 Image Plate Fading Fit Coefficients 45
3.2 IP Scanner Source Calibration 48
3.3 Example HERBI Stacks for Orion Edition 66
4.1 Summary of Pair Production Modeling Results 83
4.2 Divergence Contribution From Physics Processes 88
5.1 Pair Production Target List 93

CHAPTER I

Introduction

1.1 Dissertation Motivation

Positron-electron pairs are ubiquitous within energetic astrophysical events where phenomena such as stellar mergers and hypernovae are thought to create and destroy these matter-antimatter pairs near shock fronts of the expanding radiation. Much of the detailed physics of this "fireball" model of gamma ray bursts are experimentally unverified and rely on astrophysical observations. Relativistic positron-electron jets have the ability to recreate such shocks where direct probes of their formation, growth, and dissipation can help answer questions such as: are these astrophysical shock fronts the origin of ultra-energetic cosmic rays and nonthermal radiation from gamma ray bursts?

A great deal of work has been accomplished towards the goal of using positron-electron pairs in laboratory astrophysics experiments. The primary limitation, however, is the spatial scale ($\sim$cm) and densities (10^{13}–10^{17} cm^{-3}) necessary to form shocks within the laboratory. Standard terrestrial sources of positrons are radioisotopes that continuously emit isotropic positrons through the nuclear β-decay process at subrelativistic energies. The subsequent collimation and acceleration of these positrons involves a large investment in hardware to be effectively utilized. The maximum flux from such sources can exceed 10^{15} positrons per second, corresponding to densities of 10^4 cm^{-3} if fully collimated into a 1 cm beam. For some accelerator-based high energy physics facilities, positrons are produced by first accelerating electrons to highly relativistic energies and directing them into a converter target. Positron-electron pairs are created when high energy bremsstrahlung photons or initial electrons interact with target nuclei. The primary energy loss mechanism for photon with energy above a few MeV is pair production and the majority of the positrons produced in these converter target platforms are formed in this manner. This procedure was used by the Stanford Linear Collider [1], where a positron beam with densities up to 10^{13} cm^{-3} in a 1 mm^2 spot could be generated, but necessitated using the entire 3.2 km accelerator.

The limitations of these sources to produce high-density relativistic pairs are overcome by using lasers to generate positrons. First reported by Cowan et al. [2], using the Petawatt laser at Lawrence Livermore National Laboratory, a few hundred positrons were observed from the direct laser illumination of a gold foil, marking the first time laser energy was converted to antimatter. Soon after, positrons were generated from a table-top laser wakefield accelerator where relativistic electrons were directed into a lead target producing an estimated 10^6 positrons per laser pulse [3]. With the commissioning of several petawatt-class lasers around the world and the proliferation of high repetition rate wakefield accelerators, laboratory astrophysics experiments using laser generated pairs became a viable platform, primarily due to the favorable yield scaling with laser intensity.

Two of the first next-generation, near-petawatt class lasers came online between 2006 to 2008 and demonstrated the ability of producing copious amounts of antimatter. The initial study, performed at the Titan laser [4] at the Jupiter Laser Facility at Lawrence Livermore National Laboratory, showed that 10^{10} positrons per steradian can be produced with positron densities inside the target approaching 10^{16} cm^{-3}, the highest ever in a laboratory [5]. A followup experiment, using the Omega EP laser [6] at the Laboratory of Laser Energetics in Rochester, NY, produced an order of magnitude increase in positron yield while only increasing the laser energy by a factor of three [7]. The relatively small angular distribution and spot size produced an emitted pair jet with an overall density of 10^{15} cm^{-3} and a charge ratio of electrons to positrons of 100. Further studies [8] reported a positron emittance between 100–500 mm·mrad, within the limits to be used as the injector to linear accelerators, and argued that the previously created pair jets constituted a relativistic pair plasma by exceeding the number of pairs within a Debye sphere [9]. Recently, the collection of nearly a decade of pair-plasma experiments, performed at three high-energy laser facilities, showed that the positron yield scales as the square of the laser energy [10] and, if the scaling holds, the formation of shocks in the linear stage of Weibel instability growth (filamentation in plasma flows) can be expected from a laser with 7 kJ of energy and the nonlinear growth regime is achievable with a 22 kJ laser. The current generation of high-energy laser facilities have anticipated capabilities of up to 10-13 kJ [11, 12] and, for the first time, laboratory astrophysics experiments using laser-generated pairs will be possible in the foreseeable future.

Much of the effort to fulfill the technical needs for increased pair densities has been performed using high-energy laser facilities. A complementary approach using high-intensity lasers may be capable of creating charge-neutral relativistic pair plasmas, albeit at lower densities. There has been a recent renewed interest in wakefield accelerated electrons as a driver of pair production, where Sarri et al. [13] reported to have produced high density, narrow divergence positrons from a 25 TW, table-top laser. Subsequent studies at a larger femtosecond laser claimed to create a charge neutral pair plasma where, using very thick targets, the initial wakefield accelerated electrons were depleted and only the produced positron-electron pairs escaped the target [14]. The price for charge neutrality, in this case, is the reduction in pair density. The work by Sarri et al. raised questions about the fundamental limitations of creating near-collimated positrons, where the pair production process and other scattering events, such as Coulomb collisions, imposes a non-negligible intrinsic divergence to the particles. Additional experimental and modeling investigations (discussed in Chapter IV and published in Ref. [15]) were warranted to verify and understand the claims made in these studies.

Despite the recent advancements in understanding of pair generation via lasers, several obstacles remain as unmet challenges for the successful design and implementation of future experiments. Marginal improvements to the divergence characteristics can allow colliding jets the interaction time necessary to proceed into nonlinear regimes. Building on initial experiments performed by Hui Chen et al. [16], a particle collimating device was designed and constructed (see Chapter V) to create a narrow divergence positron beam. Furthermore, in the design of future laboratory astrophysics experiments, predictive capabilities of pair generation from arbitrary laser and target configurations must be well known. Positron yield for different target geometries and laser intensities [5, 7, 10] have been investigated, as well as the high energy photon spectrum, which is primarily responsible for the generation of pairs [17]. Pair production efficiencies from various target materials have not, until now, been systematically studied.

This dissertation seeks to improve upon the general understanding of laser-generated positron-electron pairs from both direct laser-target interactions and laser-wakefield sources, as well as provide guidance to the planning of future laboratory astrophysics experiments.

1.2 Summary of Results

This dissertation presents experimental investigations of positron-electron pair generation from ultraintense laser-matter interactions. These results complete the experimental phase space necessary to design and implement laboratory astrophysics studies using relativistic pairs. A laser wakefield accelerator was found to be a viable source of moderate density, relativistic positrons where the fundamental limitation of creating narrow-divergence beams was explored [15]. The material dependence of positron generation from direct laser-matter interactions was found to have an effective scaling proportional to Z^2, reduced significantly from the analytic cross section scaling by attenuation in the target.

1.3 Outline

The structure of this dissertation is as follows: the physics of pair production and the use of ultraintense lasers to produce pairs are presented in Chapter II; the design of experimental facilities and diagnostics are discussed in Chapter III; the results of a study determining the fundamental limitations to pair production using a laser wakefield electron source are presented in Chapter IV; a study on the target material and thickness dependence on effective positron yield is discussed in Chapter V; a study on the feasibility of positron radiography is presented in Chapter VI; conclusions and future work is discussed in Chapter VII.

CHAPTER II

Physics of Positron-Electron Pair Production

This chapter focuses on the theoretical basis of pair production using ultraintense lasers and will focus on contextualizing the experiments, simulations, and results presented in the later chapters. The physics of positron-electron pair generation is fundamentally linked to the topic of energy loss in matter by electrons and photons, which in and of itself is a large and active area of study. The dominant loss mechanisms, such as Coulomb scattering and bremsstrahlung, are discussed within this chapter. The theory and formulation of laser absorption into relativistic electrons, which drives pair generation, and the subsequent acceleration of positrons from the rear target sheath field are also presented.

2.1 Pair Production

Positrons are the antiparticle of electrons where each have a rest mass of $m_{e^-} = m_{e^+} = 511$ keV$/c^2$. When a positron and electron collide, the pair annihilates and their total energy (rest mass energy plus kinetic energy) is converted into characteristic photons emitted in an orientation that conserves momentum. In a center of mass rest frame, a positron and electron annihilating typically produces two photons, emitted with opposite momentum and an energy of 511 keV each. The reverse process, the creation of a positron-electron pair, necessarily requires a minimum threshold energy of $E_{th} = 2mc^2 = 1.022$ MeV.

In the context of an ultraintense laser-matter interaction, candidate particles that initiate pair production are limited tophotons, electrons, and ions. Due to a comparatively large population of relativistic electrons, two processes (electron-ion and photon-ion colli-

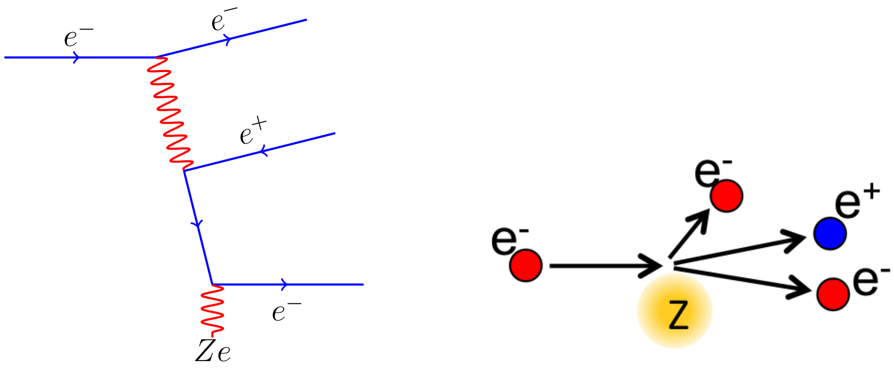

(a) (b)

Figure 2.1: (a) Feynman diagram for the direct (Trident) method of pair production and (b) a real-space cartoon of the prEocess. The Trident process is so called from the three-pronged appearance of the real-space cartoon.

sions) have interaction probabilities significantly larger than the others. In the so-called Trident process (electron-ion) an above-threshold electron scatters from a nuclear charge, exchanging a virtual photon, which then decays into a positron-electron pair. In the Bethe-Heitler process (photon-ion), an electron scattering from an ion produces an above-threshold bremsstrahlung photon (real photon) that decays into a positron-electron pair at the site of a second nuclear charge. The Feynman and real-space diagram of the Trident process is shown in Fig. 2.1 with the Bethe-Heitler process (bremsstrahlung and pair production) shown in Fig. 2.2. In each process, the photon decay into a positron-electron pair must be moderated by a perturbative nuclear charge to conserve momentum as the electron cannot emit a real photon while conserving energy and momentum without reducing its rest mass [18].

The relative occurrence of the Trident and Bethe-Heitler processes is governed by their respective cross sections, σ_T and σ_{BH}, respectively, and scales linearly with the incident particle flux. In general, for a geometry where a beam of particles is incident on a target, the fractional probability is given by $dP = \sigma\, n\, dt$ where n is the number density of the scattering sites (ions in this case) and dt is the distance the particles traverses in the material. The exact functional form of the cross section relies on a number of conditions. A basis of understanding of the scattering events can be established by solving the Schrödingier equation for an arbitrary waveform (the incident particle) with an inhomogeneous source

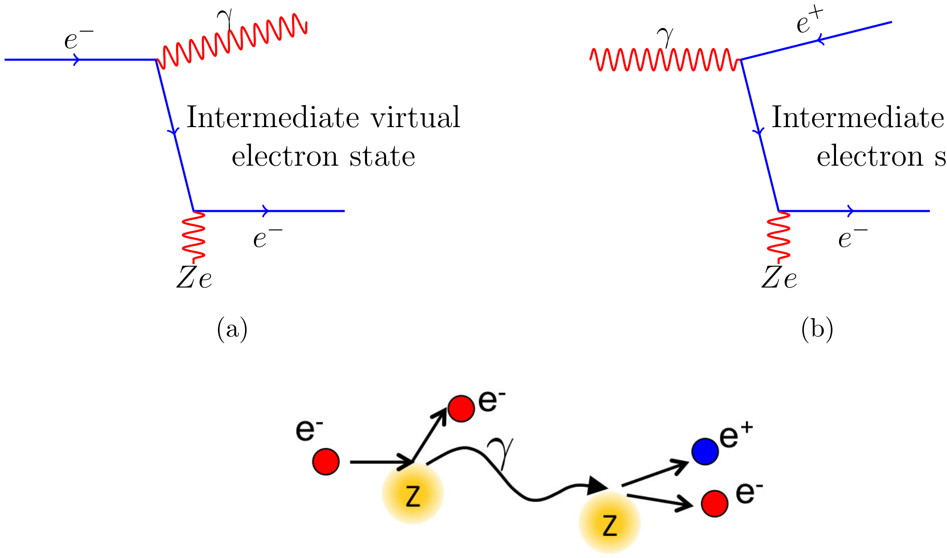
e^-
γ
Intermediate virtual electron state
e^-
Ze
γ
e^+
Intermediate virtual electron state
e^-
Ze
e-
e-
Z
γ
e+
e-
Z

(a) (b)

(c)

Figure 2.2: Feynman diagrams for (a) bremsstrahlung emission and (b) photon-ion pair production are shown. The two processes are very closely related; the pair production interaction can be obtained by the substitution of an incoming electron with an outgoing positron. A real-space cartoon of the process is shown in (c).

term (e.g., a scattering event) [19, 20]. A Green's function approach, accepting any form of the inhomogeneous driving term can be solved for the cases presented here, namely the Coulomb potential between an ion and incident electron. The time-independent Schrödingier equation is

$$-\frac{\hbar}{2m}\nabla^2\psi + V\psi = E\psi, \tag{2.1}$$

or more succinctly,

$$(\nabla^2 + k_0^2)\psi = Q, \tag{2.2}$$

where $k_0 \equiv \sqrt{2mE}/\hbar$ and $Q \equiv 2mV\psi/\hbar^2$. Here, k_0, E, and ψ are the wave number, kinetic energy, and wavefunction of the incident particle, respectively, and V is the interaction potential. Equation (2.2) has the form of the Helmholtz equation and has a solution of

$$G(\mathbf{r}) = -\frac{e^{ik_0 r}}{4\pi r}, \tag{2.3}$$

where the general solution to the Schrödingier equation is given by

$$\psi(\mathbf{r}) = \psi_0(\mathbf{r}) - \frac{m}{2\pi\hbar^2}\int \frac{e^{ik_0|\mathbf{r}-\mathbf{r}_0|}}{|\mathbf{r}-\mathbf{r}_0|}V(\mathbf{r}_0)\psi(\mathbf{r}_0)d^3\mathbf{r}_0, \tag{2.4}$$

centered at $\mathbf{r}_0$. The incident wavefunction, ψ_0, is the solution to the homogeneous solution (steady state). In this exact solution, however, and the ψ within the integral in Eq. (2.4) requires that we already know the wavefunction. We now invoke the Born approximation, which assumes that the potential V is weak and does not meaningfully change the incident wavefunction. If the incident particle can be expressed as a plane wave then the first term in the Born expansion is $\psi(\mathbf{r}) \approx \psi_0(\mathbf{r}) = Ae^{i\mathbf{k}\cdot\mathbf{r}}$. For a particle traveling in the $+z$ direction encountering a finite extent potential centered at the origin,

$$\psi(\mathbf{r}) \cong Ae^{ikz} + \frac{e^{ikr}}{r}\underbrace{\frac{-m_e}{2\pi\hbar^2}\int e^{i(\mathbf{k_0}-\mathbf{k})\cdot\mathbf{r}_0}V(\mathbf{r}_0)d^3\mathbf{r}_0}_{f(\theta,\phi)}, \tag{2.5}$$

where the bracketed term, f, is defined as the scattering amplitude. By taking the absolute square of the scattering amplitude, the probability of scattering into a given angle is

$$\frac{d\sigma}{d\Omega} = |f(\theta,\phi)|^2 \propto |V(r)|^2 \tag{2.6}$$

and defines the differential cross section. In the following sections, we address the three relevant scattering interactions to both Bethe-Heitler and Trident pair production: (1) bremsstrahlung emission; (2) pair production by a photon; (3) pair production by an electron. For each of these cases, the perturbative potential is the Coulomb potential between the target ion and the incident particle,

$$V(r) = \frac{1}{4\pi\epsilon_0}\frac{q_i q_t}{r} \tag{2.7}$$

where q_i, q_t are the charges of the incident and target particle and $\epsilon_0 = e^2/(2\alpha hc)$ is the vacuum permittivity. It can be seen from this description that the cross sections will follow the derivation $d\sigma \propto (q_i q_t)^2 = Z^2 e^4$ for cases (1) and (2), and $d\sigma \propto Z^2 e^2$ for case (3).

2.1.1 Bremsstrahlung Emission

Bremsstrahlung, a German word that translates directly to "breaking radiation," refers to the energy radiated by a charged particle under acceleration in a Coulomb field. A deflected electron conserves energy by emitting a photon that obeys the relationship

$$E + k = E_0, \tag{2.8}$$

where E_0 and E are the initial and final energy of the electron, respectively, and k is the energy of the photon. The influence of the nucleus means that the momentum is not necessarily conserved between electron and photon where the final energy of the photon can be any continuous energy below E_0. For nonrelativistic electron energies the bremsstrahlung cross section can be solved exactly [21], yet for relativistic initial energies, which are the only such interactions that pair production depends on, a solution is only possible using approximation methods. The complicated nature of bremsstrahlung comes from the continuous final energy of the electron. For each emission energy there exists a unique transition matrix element between initial and final state of the electron. In the high energy limit, this becomes computationally prohibitive where the number of states is $\sim 137E_0/mc^2$, such that a 12 MeV electron has ~3300 states with a transition matrix of 10^7 elements [22].

To reduce the computational overhead of bremsstrahlung cross section expressions, Born approximation is used. These most faithfully represent the experimental data while also being compact. However, 'Born' breaks down when the atomic number or electron energy increases, as well as at the high energy photon tail when $k/E_0 \rightarrow 1$, where the wavefunction is significantly altered by the perturbative potential. The approximations maintain an order of magnitude agreement with experiments over nearly all conditions where, if further assumptions are chosen correctly, the errors approach only a few percent. A complete reference for all bremsstrahlung calculation techniques are detailed in Koch and Motz [23]. The current

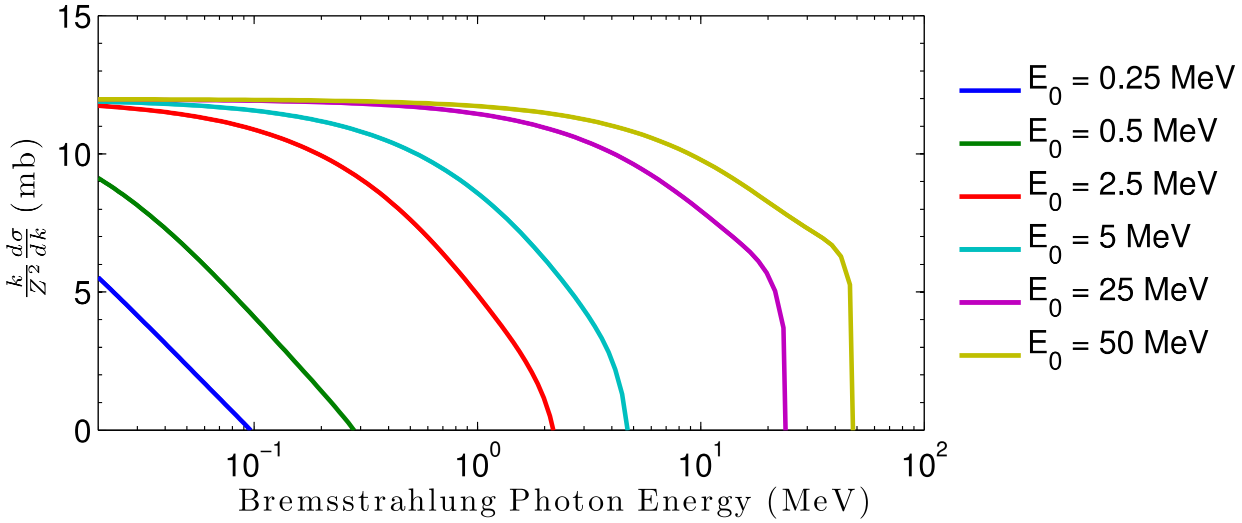

Figure 2.3: Bremsstrahlung cross section for the relativistic Born approximation with nuclear screening effect.

derivation will only present the Born approximation closest to the experimental working conditions explored in this work in order to understand the dependencies on parameters such as target material. The bremsstrahlung cross sections can be derived in differential forms with respect to any combination of the relevant parameters: scattered electron energy; photon energy; photon emission angle; electron emission angle. By integrating over these parameters, the total radiation cross section is calculated, dependent on only the initial electron energy and material.

For the purposes of current study, only above-threshold photons are of interest, and so the relativistic ($E_0, E, k \gg mc^2$), partially screened Born approximation is chosen. Screening is an important factor, as most of the source electrons will not be above the critical energy for complete screening (∼30 MeV for gold). The approximate screening assumption accounts for the finite size of the electron-ion Coulomb potential,

$$V_{\text{screened}} = \frac{1}{4\pi\epsilon_0}\frac{Ze^2}{r}\exp(-r/a).$$

This Born approximation has a differential cross section with respect to photon energy of

[24]

$$d\sigma_k = \frac{2}{137}\frac{Z^2e^4}{m^2c^4}\frac{dk}{k}\left\{\left[1+\left(\frac{E}{E_0}\right)^2-\frac{2}{3}\frac{E}{E_0}\right]\left(\ln M+1-\frac{2}{b}\tan^{-1}b\right)\right.$$
$$\left.+\frac{E}{E_0}\left[\frac{2}{b^2}\ln(1+b^2)+\frac{4(2-b^2)}{3b^2}\tan^{-1}b-\frac{8}{3b^2}+2/9\right]\right\} \qquad (2.9)$$

where

$$b=\left(\frac{2E_0EZ^{1/3}}{111k}\right);\quad \text{and}\quad M=\left[\left(\frac{k}{2E_0E}\right)^2+\left(\frac{Z^{1/3}}{111}\right)^2\right]^{-1}.$$

The numerical calculation of this cross section is shown in Fig. 2.3 for initial electron energies within the range produced by ultraintense lasers, normalized to the atomic number of the target material. In the relativistic case, the angular emission is centered around the initial electron trajectory with a cone angle of $\theta_k \simeq \gamma^{-1} = mc^2/E$ and expressed as [25]

$$d^2\sigma_k = \left[\frac{3}{2\pi}\gamma^2\frac{(1+\gamma^4\theta^4)}{(1+\gamma^2\theta^2)^2}\right]d\sigma_k d\Omega. \qquad (2.10)$$

For 5 MeV electrons, the bremsstrahlung cone angle is $\theta_k \simeq 5.3°$ and decreases to $\theta_k \simeq 1.5°$ for $E_{e^-} = 20$ MeV.

2.1.2 Pair Production by Photons

As visually shown in Feynman diagrams in Fig. 2.2, bremsstrahlung and pair production are very closely related and the considerations in calculating the cross sections are nearly identical. In any Feynman diagram, the electron can be replaced by a negative energy positron moving backwards in time. With appropriate substitutions of the incident and scattered particles, the differential pair production cross section will be equivalent to Eq. (2.9). The conversion follows as

	Particle	Energy
Incident	$e^- \rightarrow e^+$	$E_0 \rightarrow -E_+$
Scattered	$e^- \rightarrow e^-$	$E \rightarrow E_-$
Created	photon → photon	$k \rightarrow k$

where a phase-space ratio of $E_+dE_+/(k^2dk)$ term is necessary to relate the differential pho-

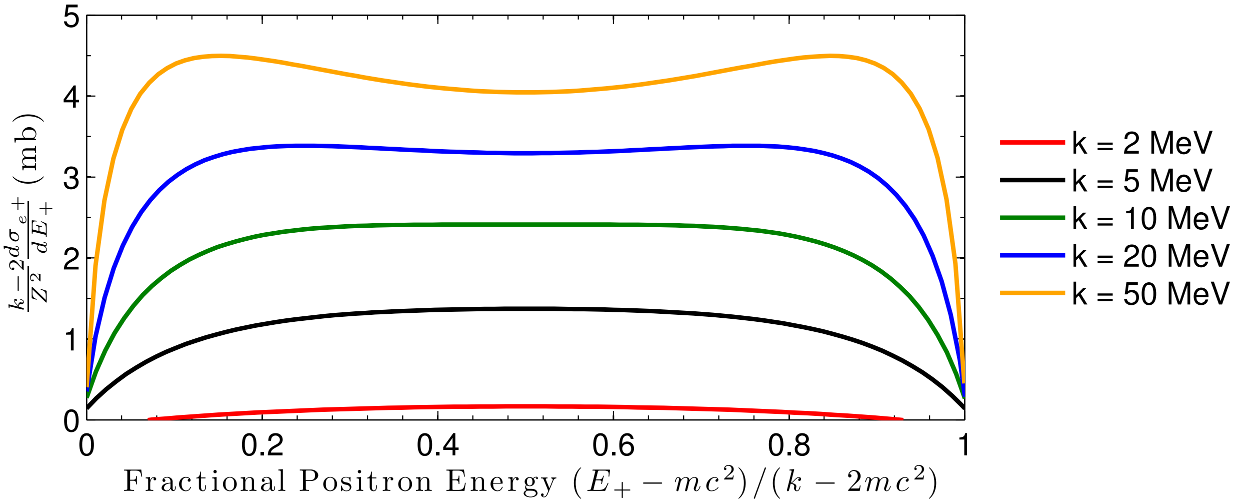

Figure 2.4: Pair production cross section for the relativistic Born approximation, plotted against the fractional kinetic energy the positron retains from the incoming photon. The pair creation threshold requires that photons carry at least $2mc^2$ of energy.

ton energy to particle energy. The pair production cross section for the relativistic Born approximation with atomic screening is given by [26]

$$d\sigma_{e^+/e^-} = \frac{2}{137}\frac{Z^2e^4}{m^2c^4}\frac{dE+}{k^3}\left\{\left[E_+^2 + E_-^2 + \frac{2E_+E_-}{3}\right]\left(\ln M + 1 - \frac{2}{b}\tan^{-1}b\right)\right.$$
$$\left. -E_+\left[\frac{2}{b^2}\ln(1+b^2) + \frac{4(2-b^2)}{3b^2}\tan^{-1}b - \frac{8}{3b^2} + 2/9\right]\right\} \qquad (2.11)$$

where

$$b = \left(\frac{2E_+E_-Z^{1/3}}{111k}\right); \quad \text{and} \quad M = \left[\left(\frac{k}{2E_+E_-}\right)^2 + \left(\frac{Z^{1/3}}{111}\right)^2\right]^{-1}.$$

The angular distribution of pair creation similarly follows from bremsstrahlung where $\theta_{e^+/e^-} \simeq \gamma^{-1} = mc^2/E_+$. The pair production cross section is shown in Fig. 2.4 for a selection of incident photon energies.

For the Bethe-Heitler process, the number of pairs produced within a target of marginal thickness, dt, is a function of the incident number of photon, N_k, where the fractional yield can be expressed as $dP_{BH} = N_k n_i \sigma_{e^+/e^-} dt$. The number of the bremsstrahlung photons created by a single electron can be expressed in a similar form as $dP_k = n_i\sigma_k dt$. For the

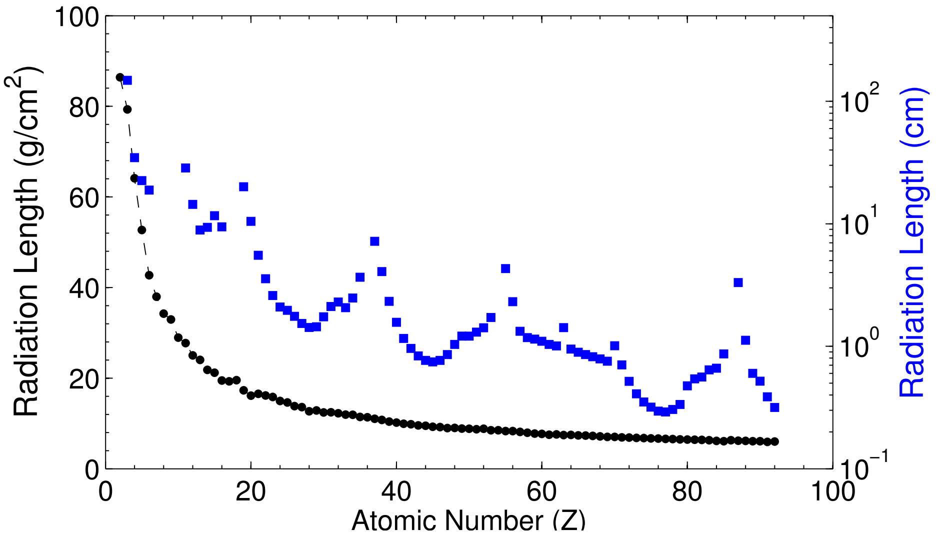

Figure 2.5: Radiation Length for various elements $Z = 2$–92 in units of g/cm^2 (dots) and normalized to the standard densities in units of cm (squares).

moment, if we are not concerned about the cross section energy dependence, the Bethe-Heitler yield scales as

$$dP_{BH} \propto n_i^2 dt^2 Z^4, \tag{2.12}$$

given the material dependence of Eq. (2.9) and (2.11).

A more precise estimate of pair production begins by considering an approximate expression for the bremsstrahlung intensity, as only the above-threshold photons contribute. The objective here is to show the scaling dependencies of experimental parameters to reasonable accuracy. To this effect, a complete screening approximation is used for its compactness and error within an order of magnitude [23, 27, 28] and is given in terms of the target's radiation length. The radiation length unit is a very helpful measure, denoting the mean distance over which a high energy electron will lose all but $1/e$ of its energy, as well as $7/9^{\text{th}}$ of the mean free path of a photon before pair producing (another consequence of bremsstrahlung and pair production being linked). The radiation length of a material, X_0, is shown for all elemental materials in Fig. 2.5, and given by [29]

$$\frac{1}{X_0} = 4\alpha r_0^2 \frac{N_A}{A} \left\{ Z^2 \left[L_{\text{rad}} - f(Z) \right] + Z L'_{\text{rad}} \right\}, \tag{2.13}$$

where $f(Z) = (\alpha Z)^2[(1 + (\alpha Z)^2)^{-1} + 0.20206 - 0.0369(\alpha Z)^2 + 0.0083(\alpha Z)^4 - 0.002(\alpha Z)^6]$, $L_{\text{rad}} = \ln(184.15 Z^{-1/3})$, $L'_{\text{rad}} = \ln(1194 Z^{-2/3})$, and r_0 is the classical electron radius.

A simple expression of the bremsstrahlung cross section, which best illustrates pair production dependencies for cases of very high energy incident particles, is given as [28, 30]

$$\left[\frac{d\sigma_k}{dk}\right]_{HE} = \frac{A}{X_0 N_A}\frac{1}{k}\left[\frac{4}{3}\frac{k/E_0}{\ln\left[(1/(1-k/E_0)\right]}\right]. \tag{2.14}$$

Normalized units are now used to simplify the following integrals where E, E_0, k, are measured in units of mc^2 and the target thickness is given by t in units of radiation length. The intensity of the produced bremsstrahlung becomes

$$\begin{aligned}[I_k]_{HE} &= n_i \int dt \int \frac{d\sigma}{dk} dk \\ &= \frac{1}{k}\int_0^t e^{-7/9(t-t')} dt' \int_k^{E_0} \left[\frac{4}{3}\frac{k/E_0}{\ln\left[(1/(1-k/E_0)\right]}\right] dE,\end{aligned} \tag{2.15}$$

where first integral accounts for the attenuation in the target through a thickness $(t - t')$. With additional approximations to the magnitude of the terms at the high energy limit, the integrals can be evaluated to [28]

$$[I_k]_{HE}^{\text{approx}} = \frac{1}{k}\frac{(1-k/E_0)^{4t/3} - e^{-(7/9)t}}{\left[7/9 + \frac{4}{3}\ln(1-k/E_0)\right]}. \tag{2.16}$$

The Bethe-Heitler pair yield for a single electron of energy E_0 can be expressed as

$$Y_{BH} = \int_0^T dt \int_{2mc^2}^{E_0} I_k \sigma_{e^+e^-} dk$$

so that

$$[Y_{BH}]_{HE}^{\text{approx}} = \int_{2mc^2}^{E_0} \frac{\sigma_{e^+/e^-}}{k\left[7/9 + \frac{4}{3}\ln(1-k/E_0)\right]} \int_0^T (1-k/E_0)^{4t/3} - e^{-(7/9)t} dk dt.$$

The integration over target thickness can be performed exactly,

$$[Y_{BH}]_{HE}^{\text{approx}} = \int_{2mc^2}^{E_0} \frac{\sigma_{e^+/e^-}}{k\left[7/9 + \frac{4}{3}\ln(1-k/E_0)\right]} \left\{\left[\frac{(1-k/E_0)^{4T/3}-1}{\frac{4}{3}\ln(1-k/E_0)}\right] - \left[\frac{9}{7}\left(1-e^{-(7/9)T}\right)\right]\right\} dk,$$

and the substitution of $f = -\frac{4}{3}\ln(1-k/E_0)$ simplifies the expression to

$$[Y_{BH}]_{HE}^{\text{approx}} = \int_{2mc^2}^{E_0} \frac{\sigma_{e^+/e^-}}{k\,[7/9-f]} \left\{\left[\frac{1-e^{-fT}}{f}\right] - \left[\frac{9}{7}\left(1-e^{-(7/9)T}\right)\right]\right\} dk. \tag{2.17}$$

Assuming that the full thickness of the target, T, is small, we can expand out the exponentials, keeping the first three terms, where the inner terms with T dependencies become

$$\begin{aligned}\left[\frac{1-e^{-fT}}{f}\right] - \left[\frac{9}{7}\left(1-e^{-(7/9)T}\right)\right] &= \left[\frac{1-(1-fT+\frac{1}{2}f^2T^2)}{f}\right] - \left[\frac{9}{7}\left(1-\left[1-\frac{7}{9}T+\frac{7^2}{9^2}\frac{T^2}{2}\right]\right)\right] \\ &= \frac{7}{9}\frac{T^2}{2} - \frac{fT^2}{2} = \frac{T^2}{2}\left(\frac{7}{9}-f\right),\end{aligned}$$

such that as $T \to 0$, the approximate pair yield is

$$[Y_{BH}]_{HE}^{\text{approx}} \xrightarrow[T \to 0]{} \frac{T^2}{2}\int_{2mc^2}^{E_0} \frac{\sigma_{e^+/e^-}}{k} dk, \tag{2.18}$$

which follows from the scaling of the probability densities in Eq. (2.12). For the case with a thick target, however, the exponential terms in Eq. (2.17) evaluate to zero, and after some algebra,

$$[Y_{BH}]_{HE}^{\text{approx}} \xrightarrow[T \to \infty]{} \int_{2mc^2}^{E_0} \frac{9}{7f}\frac{\sigma_{e^+/e^-}}{k} dk. \tag{2.19}$$

The independence of target thickness on pair yield at the infinite limit is to be expected since in this case, all initial electrons have depleted their energy in the first few radiation lengths of the target and no additional gain is possible from these primary particles by increasing the target thickness. In physical units, the target thickness scaling of Eq. (2.18) is $(T/X_0)^2 \propto (Z^2 + Z)^2$, which is consistent with out previous assumption that the Bethe-Heitler pair yield scales as Z^4.

2.1.3 Pair Production by Electrons

Trident pair production, or the creation of leptonic pairs (electron-positron here) by virtual photons in Coulomb fields, is not expected to play a large roll within the context of thick target, laser-produced pairs since radiative energy loss dominates electron dynamics. In cases of thin targets, however, Trident becomes an appreciable component of the total pair yield. The experiments performed in this study do not explore this thin-target regime, where we include a discussion of pair production by electrons for completion and to compare the dominance of Bethe-Heitler process over Trident.

The Trident pair production process was first considered by Bhabha [31] and is often approximated by the Bhabha cross section. Numerically evaluated descriptions have been offered that significantly reduce the uncertainties in the MeV energy range [32, 33]. From the results discussed earlier, we expect that the interaction cross section will have a proportionality of Z^2 since the scattering occurs in the nuclear Coulomb field. For electrons with energies away from the creation threshold, $2mc^2$, the total Trident cross section is approximated by

$$\sigma_{eZ} = \frac{28}{27\pi}\left(\frac{Ze^2}{137mc^2}\right)^2 \ln^3\left(\frac{E_0}{mc^2}\right), \tag{2.20}$$

where E_0 is the incident electron energy. Comparing this result to the Bethe-Heitler cross section, using a relativistic unscreened point nucleus approximation, gives

$$\frac{\sigma^{e^- - Z}_{e^+/e-}}{\sigma^{k-Z}_{e^+/e-}} = \frac{\left(\frac{Zr_0}{137}\right)^2 \frac{28}{27\pi}\ln^3\left(\frac{E_0}{mc^2}\right)}{\frac{Z^2 r_0}{137}\left[\frac{28}{9}\ln\left(\frac{2E_0}{mc^2}\right) - \frac{2}{27}\right]} \approx \frac{1}{3\pi}\frac{1}{137}\ln^2\left(\frac{E_0}{mc^2}\right), \tag{2.21}$$

where the photon pair production is always more probabilistic for a given initial energy. Between 10–100 MeV, Eq. (2.21) ranges from 0.007–0.02. It is clear from these cross sections that photo-production of pairs is more efficient by about two orders of magnitude.

The pair yield from each process is shown in Fig. 2.6 for two high-Z elements, tantalum and gold, where the quadratic dependence on target thickness is observed for the Bethe-

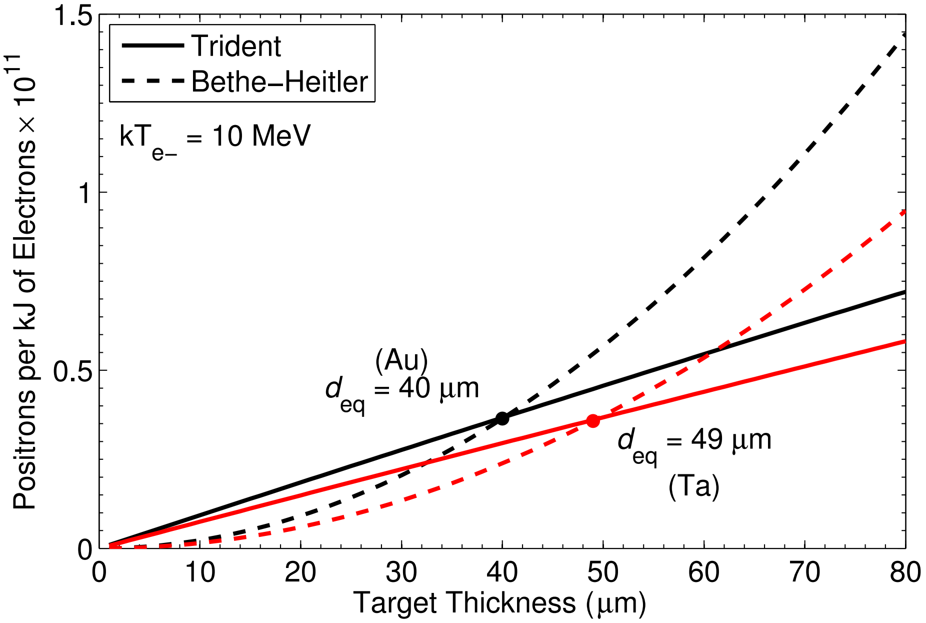

Figure 2.6: Analytic comparison between Trident and Bethe-Heitler pair production processes for tantalum and gold using a 10 MeV exponential electron spectrum as the source input. As the target thickness increases, Bethe-Heitler overtakes Trident at a thickness of d_{eq}.

Heitler and linear dependence for Trident. The thickness at which the two pair production processes contribute equally, d_{eq}, is on the order of 40-50 μm for a 10 MeV exponential electron source. The material dependence of the equivalent thickness is due to the roughly 20% difference in their radiation lengths. This equivalent thickness result is consistent with previous numerical studies [34], where it was found that for a 4 MeV electron temperature in gold, $d_{eq} = 20$ μm.

2.2 Electron Acceleration Mechanisms of Ultraintense Lasers

Both the Bethe-Heitler and Trident pair production mechanisms rely on initialized relativistic electrons to drive the respective reactions. These electrons can be created by many acceleration mechanisms where here, we have defined our scope to investigate pair production using ultraintense lasers. This platform has intrinsic advantages for not only the creation, but also the utilization and application, of the resulting relativistic pair plasma.

The working definition of an 'intense' laser is one that has an electric field intensity sufficient to field ionize a target atom. The atomic radius of most elements is on the order of a few times the Bohr radius,

$$a_{\text{Bohr}} = \frac{\hbar}{mc\alpha} = 5.3 \times 10^{-9} \text{ cm} = 0.53 \text{ Å}, \tag{2.22}$$

where $\alpha = 1/137$ is the fine structure constant. Taking the minimum case of hydrogen, the atomic electric field is

$$E_{\text{a}} = \frac{1}{4\pi\epsilon_0} \frac{e}{a_{\text{Bohr}}^2} \simeq 5.1 \times 10^9 \, \frac{\text{V}}{\text{m}}. \tag{2.23}$$

The field intensity to overcome the binding energy of the electron is then

$$I_{\text{a}} = \frac{c\epsilon_0}{8\pi} E_{\text{a}}^2 \simeq 3.5 \times 10^{16} \, \frac{\text{W}}{\text{cm}^2}. \tag{2.24}$$

For higher-Z elements, single electron ionization occurs at lower intensities due to screening from the nucleus, allowing outer electrons to be removed more easily. The ionization of inner-shell electrons of these nuclei requires higher intensities where a Ne^{7+} requires fields of $I \simeq 10^{17}$ W/cm^2. In the case of a laser field, ionization of atoms begins significantly below this intensity limit due to multiphoton absorption, which occurs at intensity of only 10^{14} W/cm^2.

Achieving such high intensities is only possible using short-pulsed lasers. There have been many significant advancements to laser technology since the first laser was demonstrated in 1960. While many pulsed laser systems exist, there are only three main classes of lasers capable of producing very high fields, up to 10^{22} W/cm^2, which are in wide usage today. These are generally grouped based on the active laser medium and the amplification processes: (1) Neodymium glass (long pulse); (2) Nd:glass using chirped pulse amplification (short pulse); and (3) titanium doped sapphire (ultrashort pulse).

Neodymium doped glass amplifiers were developed in the 1980's and quickly became the system of choice for high-power laser facilities. Their fundamental wavelengths are near ∼1 μm and have pulse lengths of ∼1 ns, reaching intensities of 10^{17} W/cm^2. Chirped pulse amplification, which is discussed further in Chapter 3.1, allowed the temporal compression of Nd:glass pulses into ∼1 ps durations, inaugurating the "short pulse" laser regime, and pushed the intensity limits to 10^{21} W/cm^2. "Ultrashort" lasers use a different active laser medium, titanium doped sapphire (Ti:sapphire) which, at the forefront of the technology, can produce pulses on the order of 10 fs. These lasers typically only have a few joules of energy but can reach intensities above 10^{22} W/cm^2. Unlike Nd:glass systems, however, Ti:sapphire lasers can operate at repetition rates on the order of hertz instead of a few shots per hour.

The physics of depositing laser energy into a target changes significantly for each of these laser systems, depending on the pulse duration and intensity. This study uses the later two, and will focus on the energy conversion to relativistic electrons in the following sections.

2.2.1 Electron Acceleration in a Laser Field

The ultraintense laser regime begins when the electric field is large enough to drive electron oscillation velocities approaching c. Following Gibbon [35], the Lorentz equation for an electron in an electromagnetic field is

$$\frac{d\mathbf{p}}{dt} = -e\left(\mathbf{E} + \mathbf{v} \times \mathbf{B}\right). \tag{2.25}$$

where $\mathbf{v}$ and $\mathbf{p}$ are the quiver velocity and quiver momentum of the electron with $\mathbf{p} = \gamma m \mathbf{v}$ and γ is the Lorentz factor. The change in the potential energy of the particle is given by

$$\frac{d}{dt}U = \frac{d}{dt}(\gamma mc^2) = -e(\mathbf{v} \cdot \mathbf{E}). \tag{2.26}$$

In the low energy limit of $|\mathbf{v}| \ll c$, the term $|\mathbf{v} \times \mathbf{B}| \ll |\mathbf{E}|$, and the electron oscillates in only the direction of the electric field. As $|\mathbf{v}|$ becomes appreciable to c, the magnetic field imparts a longitudinal force on the electron. If we assume an incident plane wave traveling in the positive x direction, where the electron is initially at rest, we can use the identities

$$\mathbf{E} = -\frac{\partial \mathbf{A}}{\partial t} \quad \text{and} \quad \mathbf{B} = \nabla \times \mathbf{A} = \left(0, \frac{-\partial A_z}{\partial x}, \frac{\partial A_y}{\partial x}\right) \tag{2.27}$$

such that the momentum perpendicular to the direction of propagation becomes

$$\frac{d\mathbf{p}_\perp}{dt} = e\left(\frac{\partial \mathbf{A}}{\partial t} + v_x \frac{\partial \mathbf{A}}{\partial x}\right),$$

and results in

$$\mathbf{p}_\perp - e\mathbf{A} = \mathbf{p}_{\perp 0} = 0, \tag{2.28}$$

where $\mathbf{p}_{\perp 0}$ is the initial perpendicular momentum which was chosen to be at rest. Here, we have assumed that the scalar potential is negligible and the electron's electric field is much less than the electric field of the incident EM wave. Combining Eq. (2.25) and Eq. (2.26),

$$\frac{dp_x}{dt} - mc\frac{d\gamma}{dt} = -v_y\left(\frac{d\mathbf{A}_y}{dt} + \frac{d\mathbf{A}_y}{dx}\right) - v_x\left(\frac{d\mathbf{A}_z}{dt} + \frac{d\mathbf{A}_z}{dx}\right) = 0 \tag{2.29}$$

since $|\mathbf{A}| = A_x$. Integrating Eq. (2.29) gives

$$mc(\gamma - \delta) = p_x, \tag{2.30}$$

where δ is a constant of integration. At $t = 0$, $\delta = 1$ since the electron is initially at rest ($p_{x,t=0} = 0$). Using the identity $\gamma^2 = 1 + (p_\perp^2 + p_x^2)/(m^2c^2) = p_x^2/(m^2c^2) + 2p_x/(mc) + 1$, Eq. (2.30) becomes

$$p_x = \frac{p_\perp^2}{2mc} = \frac{(eA_x)^2}{2mc} = mc\frac{a_0^2}{2}, \tag{2.31}$$

where a_0 is the normalized vector potential of the laser. For a laser of frequency ω_L and wavelength λ_L, the definition of a_0 becomes

$$a_0 = \frac{e|\mathbf{A}|}{mc} = \frac{e|\mathbf{E}_L|}{\omega_L mc} = \frac{e\lambda_L}{2\pi mc^2}\sqrt{\frac{2I_L}{\epsilon_0 c}}. \tag{2.32}$$

As electrons in the laser focus are accelerated, the perpendicular and parallel momenta are coupled according to Eq. (2.31) with a characteristic angle of emission given by

$$\tan\theta = \frac{p_\perp}{p_\parallel} = \sqrt{\frac{2}{\gamma - 1}}. \tag{2.33}$$

Also from Eq. (2.31), as the perpendicular momentum approaches mc, $a_0 \approx 1$ and defines the relativistic regime of laser intensity. At laser wavelengths near 1 μm, the relativistic intensity limit begins at $I_L \simeq 10^{18}$ W/cm^2. The linear relationship between a_0 and wavelength has consequences to laser-to-electron energy conversion where, for applications such as inertial confinement fusion, it is favorable to minimize the production of energetic electrons. As such, the third harmonic wavelength (3ω) is used, reducing the a_0 of the laser, and therefore the coupling into energetic electrons.

2.2.2 Ponderomotive Force

The ponderomotive force, defined as the time averaged force perpendicular to the direction of travel, is an important concept in laser-accelerated electrons. In the nonrelativistic regime for a plane wave traveling in the $+x$ direction, Eq. (2.25) becomes

$$\frac{\partial v_y}{\partial t} = -\frac{e}{m} E_y, \tag{2.34}$$

where the electric field can be Taylor expanded to

$$E_y \simeq E_0 \cos\phi + y \frac{\partial E_0}{\partial y} \cos\phi + \ldots$$

with $\phi = \omega_L t - kx$ and k is the wavenumber of the laser. Solving Eq. (2.34) using the first order approximation of E_y gives $v_y^{(1)} = -eE_0/m\omega \sin\phi$, and $y^{(1)} = -eE_0/m\omega^2 \cos\phi$. Here, $|v_y^{(1)}|$ is defined as the quiver velocity of the electron. The second order solution to the equation of motion is

$$\frac{\partial v_y^{(2)}}{\partial t} = \frac{-e^2}{m^2\omega^2} E_0 \frac{\partial E_0}{\partial y} \cos^2\phi,$$

where the time averaged acceleration gives the ponderomotive force on the electron,

$$f_p \equiv \frac{-e^2}{4m\omega^2} \frac{\partial E_0^2}{\partial y} = \frac{-2\pi e^2}{\epsilon_0 m c \omega^2} \nabla I. \tag{2.35}$$

Since the ponderomotive force is proportional to the radial gradient of an incident laser intensity, electrons will be preferentially accelerated from the highest intensity regions, which is on-axis for Gaussian profiles.

In the relativistic regime when the $|\mathbf{v} \times \mathbf{B}|$ term becomes non-negligible, the oscillatory motion of the electron is converted through this term into parallel motion. This can be very substantial, as we will see below, where in the case of a laser interacting with a bulk plasma, the electrons can be thought of as an ensemble of current density, $\mathbf{J}$.

2.2.3 Relativistic $\mathbf{J} \times \mathbf{B}$ Mechanism

When incident on a solid target the intrinsic intensity pedestal of the main pulse, typically between 10^{10}–10^{13} W/cm^2, will ionize the front surface. The plasma pressure and resulting heating causes ions to ablate at roughly the speed of sound calculated by

$$c_s = \left(\frac{Z^\star k_B T}{m_i}\right)^{1/2} \simeq 3.1 \times 10^7 \left(\frac{T}{\text{keV}}\right)^{1/2} \left(\frac{Z^\star}{A}\right)^{1/2} \frac{\text{cm}}{\text{s}}, \tag{2.36}$$

where k_B is the Boltzmann constant, T_e is the ensemble electron temperature, m_i is the ion mass, and $Z^\star$ is the effective ion charge [35]. With an isothermal expansion, the density profile exponentially decreases away from the surface with a characteristic scale length $L = c_s \tau_L$, where τ_L is the pulse duration of the laser. As the laser enters the density ramp of the ablated volume, it encounters an electron density of $n_e = Z^\star n_i = Z^\star N\rho/A$, and drives electron oscillations according to the ponderomotive force. The coherent plasma oscillations are dependent on the electron density where

$$\omega_p^2 = e^2 \frac{n_e}{\epsilon_0 m} \tag{2.37}$$

is the plasma frequency of the free electrons. The incident laser will propagate though plasma densities when $\omega_L > \omega_p$, above which the laser is reflected. The critical density (i.e., when these frequencies are equal) is

$$n_c \simeq \frac{1.1 \times 10^{21}}{\lambda_{\mu\text{m}}} \text{ cm}^{-3}, \tag{2.38}$$

where $\lambda_{\mu\text{m}}$ is the laser wavelength in units of microns. The density isosurface at n_c is referred to as the critical surface. The laser will penetrate beyond this density as an evanescent wave and falls off exponentially with a characteristic length, referred to as the collisionless skin depth. In the relativistic limit, the effective critical density is increased by a factor of γ and can propagate within the overdense plasma region. This is due to the mass correction of the electron with the increased inertia inhibiting a plasma current from forming to reflect incident light.

In the underdense volume ($n_e < n_c$) at the focus of the laser, regions of higher local intensities will drive electrons in the forward direction nonuniformly, where $|\mathbf{v} \times \mathbf{B}|$ becomes appreciable. This $|\mathbf{J} \times \mathbf{B}|$ electron acceleration is controlled by the ponderomotive force, which must be accounted for in the relativistic regime. We begin with the equation of motion, where the velocity and electromagnetic fields have been substituted for the relativistic momentum and vector potential, respectively, so that,

$$\frac{\partial \mathbf{p}}{\partial t} + \frac{\mathbf{p} \cdot \nabla \mathbf{p}}{\gamma m} = -e\left(-\frac{1}{c}\frac{\partial \mathbf{A}}{\partial t} - \nabla\phi + \frac{\mathbf{p} \times \nabla \times \mathbf{A}}{\gamma m c}\right). \tag{2.39}$$

Taking the longitudinal component of the momentum, $\mathbf{p}_{\|}$, and using Eq. (2.28), the above expression can be reduced to

$$\frac{\partial p_{\|}}{\partial t} = e\nabla\phi - \left[\frac{(\mathbf{p} \cdot \nabla \mathbf{p}) + (\mathbf{p} \times \nabla \times \mathbf{p})}{\gamma m}\right]. \tag{2.40}$$

Using the vector identity, $\frac{1}{2}\nabla(\mathbf{p} \cdot \mathbf{p}) = \mathbf{p} \times (\nabla \times \mathbf{p}) + \mathbf{p} \times (\nabla \times \mathbf{p})$ and $\mathbf{p} \cdot \mathbf{p} = m^2c^2(\gamma^2 - 1)$, the force on an electron in the forward direction of the electromagnetic wave is then

$$\left\langle \frac{\partial p_{\|}}{\partial t} \right\rangle = -\frac{mc^2}{2\langle\gamma\rangle}\nabla\langle\gamma^2 - 1\rangle. \tag{2.41}$$

In the above expression, the brackets denote a temporal average over the frequency of the wave. Physically, at the critical surface, electrons will experience a ponderomotive force $\mathbf{F_p} \propto \nabla\langle E^2\rangle$, where for a linearly polarized laser field, the longitudinal term is

$$f_x = \frac{-mc^2}{2\langle\gamma\rangle}\frac{\partial\langle a_0^2\rangle}{\partial x}(1 - \cos 2\omega t) \tag{2.42}$$

Since f_x implicitly relies on n_c/n_e, the magnitude of the acceleration decreases as the electron density increases. Equation (2.41) can be rewritten in terms of the normalized vector potential of the laser to be [36–38]

$$T_{\text{Pond}} = mc^2\left(\sqrt{1 + \frac{I_L\lambda_{\mu\text{m}}^2}{1.37 \times 10^{18}}} - 1\right) \tag{2.43}$$

where I_L is in units of W/cm^2. This potential is the maximum energy that can be transferred to the electrons via the ponderomotive force. If we take the energy gain for an ensemble of the electrons in the field of the laser, then this potential can be used as an effective temperature of the nonthermal electron population with an exponential distribution.

However, Eq. (2.43) relies on a very steep density gradient with decay lengths on the order of a laser wavelength. If the density profile is an extended many times this, the acceleration mechanism scales to much hotter temperatures than that of the ponderomotive scaling. Particle-in-cell simulations reveal that the nonthermal electron temperature has an effective scaling of [39]

$$T_{\text{Pukhov}} = 1.5 \text{ MeV } \times \sqrt{\frac{I_L}{1 \times 10^{18}}}. \tag{2.44}$$

This is known as the Pukhov scaling and relies on the stochastic acceleration of electrons within plasma channels in the underdense region where the laser self-focuses to very high intensities.

2.2.4 Laser Wakefield Acceleration (LWFA)

A pulse of electromagnetic radiation in an underdense plasma leaves behind it a wake caused by the ponderomotive force. If the (laser) pulse has as a radial Gaussian profile with an intensity $I(r) = I_L e^{-2r^2/w_0^2}$, the electrons are expelled away from the axis, where $\mathbf{f}_p \propto -\nabla I/n_c$ and w_0 is the radial spot size defined as the $1/e^2$ intensity limit. An electron, initially at $r = 0$ will oscillate away from an area of higher electric field to lower field in one half of a wavelength, λ_L, and cannot make the round trip in the second half from the reduction in ponderomotive force on the wings of the intensity profile. The plasma wave, or wake, has a phase velocity, v_p, equal to the group velocity of the radiation in the medium, v_g^{EM}, where

$$v_p = v_g^{\text{EM}} = c\left(1 - \frac{\omega_p^2}{\omega^2}\right)^{1/2} \tag{2.45}$$

and ω is the photon frequency with ω_p is given by Eq. (2.37). The wake is efficiently created when the driver pulse is less than the half length of the plasma frequency, $L_{\text{EM}} < \pi c/\omega_p$, otherwise the extended pulse will eventually destroy the coherence of the wake. For an intense laser pulse, the interior of the wake becomes devoid of electrons where only bare ions

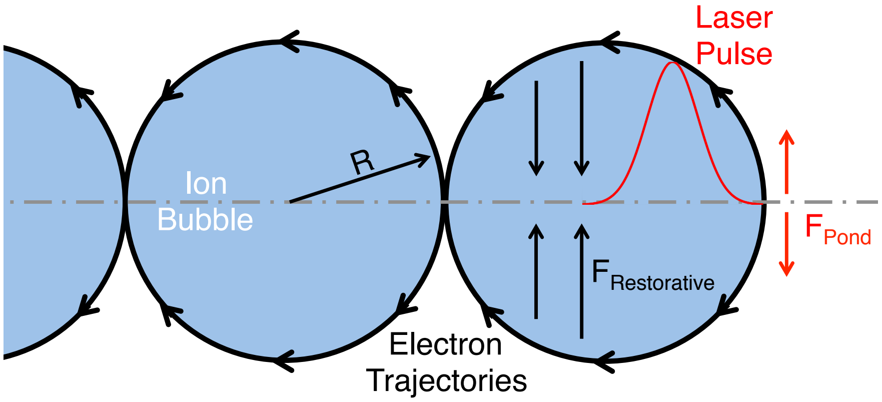

Figure 2.7: The ponderomotive force of the laser creates a wake behind the pulse and expels electrons to form an ion bubble. In an idealized scenario, the electrons make circular orbits and oscillate from the restorative Coulomb force of the ions.

remain, having inertia too large to be affected by the rapid oscillation of the laser's electric field. The positive charge of the ion bubble electrostatically pulls the sheath of electrons at the exterior towards the axis to complete a near-circular orbit. However, because of the inertia mismatch between the ions, the electrons overshoot and the oscillation of the electrons drive a many-period plasma wave after the laser has passed. A cartoon of this process is shown in Fig. 2.7. The electric field in the wake can be estimated by Gauss's law for a uniform sphere of charge where $E(r) = en_e r/3\epsilon_0$. Electrons on a circular orbit only feel the radial electric field whereas if an electron happens to be on-axis, displaced from the center of the bubble and with nonzero longitudinal momentum, it will feel an accelerating potential in the laser direction.

Suppose now that the electron's longitudinal velocity matches the phase velocity of the wake, the electrons would be trapped in the wake. This is the case for some non-circular orbits which were caused by perturbations in the laser and plasma profiles at the leading edge. The high concentration of electrons arriving back on axis from these non-circular orbits, along with the ion bubble density, can support accelerating potentials of ~500 kV over half of the plasma period (the radius of the bubble) [40, 41]. For an electron density of $n_e = 2 \times 10^{19}$ cm^{-3} the ion bubble radius is approximately $\pi c/\omega_p = 3.7$ μm, which gives an an accelerating potential of ~100 GeV/m.

In order to capitalize on the full extent of the accelerating gradient, the wake must stay intact for as long as possible, which is limited by the longitudinal extent of the laser focal spot, depletion the laser energy, and the dephasing of the electrons from the plasma periodicity. The focus of a laser in vacuum is limited to a few Rayleigh lengths, z_R, before refracting where $z_R = \pi w_0^2/\lambda$. However, the beam can be guided without expanding if traveling through a medium with a radially parabolic index of refraction. The index of refraction in a plasma is given by [42]

$$\eta(r) = \frac{ck}{\omega} \simeq 1 - \frac{1}{2}\frac{\omega_p^2}{\omega^2}\left[1 + \frac{\Delta n_{ch}}{n_e}\frac{r^2}{w_0^2} + \frac{\Delta n}{n_e} - \frac{a_0^2}{8}\right], \tag{2.46}$$

where Δn is the density depletion from the ponderomotive force and Δn_{ch} is the plasma channel density depression. Solving the paraxial wave equation with $a_0^2 \ll 1$, a constant radial spot size is can be produced when

$$\Delta n_{ch} = \frac{4\epsilon_0 m c^2}{e^2 w_0^2}, \tag{2.47}$$

or if the laser is of relativistic intensity ($a_0^2 \geq 1$) the mass correction from the ponderomotive acceleration gives the self-guiding conditions to be $a_0^2 \gtrsim 32/(k_p^2 w_0^2)$ [43]. Using the definition of a_0 from Eq. 2.32, a power threshold for self-guiding results in

$$P_c = \frac{n_c}{n_e}\frac{8\pi\epsilon_0 m^2 c^5}{e^2} \simeq 17\frac{n_c}{n_e} \times 10^9 \text{ W}. \tag{2.48}$$

Matching the laser intensity and focal spot size is necessary for self-guiding and the creation of the ion bubble where simulations have found the most stable bubble is formed when $k_p R \simeq k_p w_0 = 2\sqrt{a_0}$, and creates a near-spherical wake when $2 < a_0 < 4$ [43]. For this condition, the normalized laser vector potential can be rewritten as $a_0 \simeq 2(P/P_c)^{1/3}$.

The energy supplied to the plasma to create the wake comes from the energy lost by the laser. Since there is no appreciable absorption in the far underdense plasma, the number of photons is conserved and the net energy loss comes from the red-shifting of photons to longer wavelengths [44]. The group velocity of the laser, $v_g = \partial\omega/\partial k$, is dependent on the energy of the photons and the leading edge of the pulse, which drives the wake, slows in the plasma effectively eroding away the tip of the pulse. The speed at which the laser 'etches' is given by $v_{\text{etch}} = cn_e/n_c$, where the laser pump depletion length is determined by pulse duration τ by

$$L_{PD} \simeq \left(\frac{c}{v_{\text{etch}}}\right) c\tau \simeq \frac{n_c}{n_e} c\tau. \tag{2.49}$$

The depletion of the laser will alter the wake phase velocity away from the laser group velocity such that $v_\phi = v_g - v_{\text{etch}} = c(1 - 3n_e/2n_c)$.

As the electrons are accelerated on axis, they begin to outrun the plasma wave, traveling at $v_g < c$, eventually making their way to the center of the bubble and maximizing the energy gain. Beyond the $r = 0$ point of the bubble they decelerate or "dephase" away from the acceleration region. If the electron speed is approximated as c, the distance it travels while in the acceleration phase is R for a single bucket, which is related to the laboratory-frame distance over which it travels before dephasing as [45]

$$L_{\text{dephase}} = \frac{c}{c - v_\phi} R = \frac{2n_c}{3n_e} R = \left(\frac{P}{\text{TW}}\right)^{1/6} \left(\frac{10^{18}\ \text{cm}^{-3}}{n_e}\right)^{4/3} \text{ mm}. \tag{2.50}$$

The dephasing and pump depletion lengths limit the laser-plasma interaction, where the desired acceleration length is the maximum value of either, ideally matching both. The total energy gain by an electron in the case of $L_{\text{dephase}} > L_{PD}$ is

$$E_{\max} = e\langle E\rangle L_{\text{acc}} = 1.7 \left(\frac{P}{100\ \text{TW}}\right)^{1/3} \left(\frac{10^{18}\ \text{cm}^{-3}}{n_e}\right)^{2/3} \text{ GeV}, \tag{2.51}$$

where we have assumed $\lambda_L = 800$ nm and $\langle E\rangle$ is the average linear electric field over the dephasing length. According to Eq. (2.51), energy gain can be achieved by reducing the electron density and increasing laser power. However, the combined factors of the self-guiding condition ($P > P_c$) and the desire to create spherical wakes and limit the number of plasma periods the laser fits into, constrains the experimental choices in designing a wakefield accelerator. Typical ultrafast lasers have pulse durations of 30–60 fs at 800 nm, where a large fraction of the rising edge of the pulse fits within the wake, and have 1–10 J of laser energy corresponding to a power of ~200 TW. If we choose $a_0 = 2$, the plasma density corresponding to the critical power for self-guiding is 1.5×10^{17} cm^{-3}, although the condition to efficiently trap requires slightly higher densities [46, 47].

It has been demonstrated in many experiments that for densities of 3–20 × 10^{18} cm^{-3} and various laser conditions, electron beams can be produced with energies up to 1 GeV. These highest energy electrons come from the first bucket (∼10 fs) and have beam currents of 1–100 pC. Such beams are potentially very useful as drivers of positron production since the laser systems are typically small scale and have high repetition rates (∼1 Hz).

2.3 Passage of Particles in Matter

Electrons, positrons, and photons undergo many scattering processes and lose energy while traversing a target where these dynamics have a large influence on the resulting parameters of laser-produced positrons. Here, we explore the dominant processes for each particle in the moderately relativistic regime.

Light, charged particles (electrons and positrons) below a threshold energy primarily lose energy through inelastic Coulomb collisions which ionize and excite atomic electrons. Above energies of a few MeV for most materials, the dominant energy loss mechanism is the emission of bremsstrahlung photons, where the total energy loss per unit pathlength can be summarized by [30, 48]

$$\frac{1}{\rho}\left(\frac{dE}{dx}\right)_{\text{total}} = \frac{1}{\rho}\left(\frac{dE}{dx}\right)_{\text{collisional}} + \frac{1}{\rho}\left(\frac{dE}{dx}\right)_{\text{radiative}} . \tag{2.52}$$

The radiative energy loss can be estimated using the bremsstrahlung cross section to be

$$\begin{aligned}\left(\frac{S}{\rho}\right)_{\text{rad}} &= \frac{1}{\rho}\left(\frac{dE}{dx}\right)_{\text{rad}} \\ &= \frac{N_A}{A}\int_0^{E_0} k\frac{d\sigma_k}{dk}dk = \frac{4r_0^2\alpha}{\beta}N_A\frac{Z(Z+1)}{A}(E_0+mc^2)\ln\left(\frac{183}{Z^{1/3}}+\frac{1}{18}\right),\end{aligned} \tag{2.53}$$

where we have used the relativistic, complete screening expression as an illustration of the material and initial energy dependence. An approximation for very high energy electrons and positrons, $(S/\rho)_{\text{rad}} \approx E_0/X_0$, which has an accuracy of ∼15–30% between 20–50 MeV.

The collisional mass stopping power, $(S/\rho)_{\text{col}}$, can be calculated given the cross section

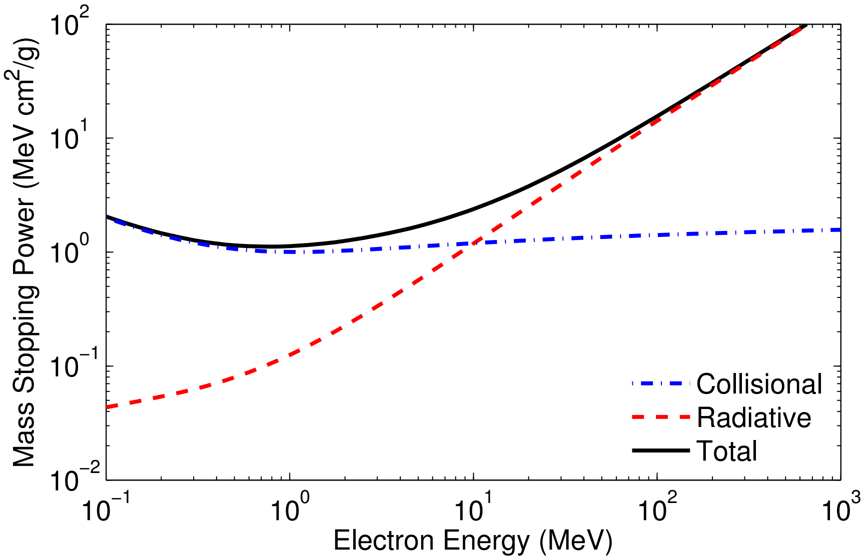

Figure 2.8: Collisional (dash-dot), radiative (dashed), and total (solid) energy loss for an electron in gold. Mass stopping power data taken from Ref. [49].

for inelastic scattering [50],

$$\left(\frac{S}{\rho}\right)_{\text{col}} = \frac{2\pi r_0^2 mc^2 NZ}{\beta^2 A}\left[\ln\left(\frac{E_0^2(E_0/mc^2+2)}{2I_E^2}\right) + F(E_0) - \delta\right], \tag{2.54}$$

where I_E is the mean excitation energy of the material, δ is a density correction factor, and

$$F(E_0) = 1 - \beta^2 + \frac{E_0^2/8mc^2 - (2E_0/mc^2)\ln 2}{(E_0/mc^2+1)^2}.$$

The density effect becomes appreciable as the energy of the particle increases and the electric field flattens and extends, which changes the interaction lengths of the collisions. There are several theoretical models that accurately predict this density correction. The exact value of I_E is dependent on the electronic structure and molecular binding of the target material and is very difficult to calculate theoretically, particularly for higher-Z materials where the recommended values have changed over time [30, 48, 50]. In practice, I_E is a free variable of the stopping power experiment and is determined by proton and alpha-particle stopping data. The Bethe equation, Eq. (2.54), has a logarithmic dependence on energy compared to the linear relation of the radiative stopping power. The relative magnitudes of the collisional and radiative energy losses are shown in Fig. 2.8.

The reciprocal of the energy loss can be integrated to give the path length an electron travels on its way to rest. The continuous slowing down approximation (CSDA) assumes the energy loss events are not discrete, where a particle's range is estimated by

$$R_{CSDA} = \int_{0}^{E_0} \left(\frac{S}{\rho}\right)^{-1}_{\text{total}} dE, \tag{2.55}$$

is not necessarily equal to the penetration depth of the particle since the integration includes the transverse motion in the particle's track. There are subtle but important differences when considering particle energy loss for positrons and electrons. If screening of the nucleus is taken into account, positrons, in contrast to electrons, feel an attractive pull towards the electron cloud, reducing the effect of screening. This acts to increase the relative energy loss for the positron. The ratio of the radiative energy loss of electrons to positrons has an empirical scaling relation proportional to E_0/Z^2 [51]. This extends the phase space in which these differences are appreciable to low-energy and high-Z. For the case of a 1 MeV positron and electron in gold, the ratio of radiative energy loss is 0.976, or a 2.4% difference.

Photon energy loss is dominated by the atomic photoelectric effect at low energies, incoherent scattering at moderately high energies, and pair production at very high energies. A summary of all energy loss processes for photons in gold is shown in Fig. 2.9. As discussed above, the focus of these studies are photons with energies greater than $2mc^2$. Near this threshold energy, it is most likely that photons will Compton scatter (incoherent scattering from valence electrons). Due to conservation of momentum, a scattered photon, emitted at an angle θ will be downshifted in energy where the difference is energies is given by

$$\frac{1}{k} - \frac{1}{k_0} = \frac{1 - \cos\theta}{mc^2} \quad \text{or} \quad \lambda = \lambda_0 + \frac{h}{mc}(1 - \cos\theta), \tag{2.56}$$

where k_0 (k) and λ_0 (λ) are the incident (scattered) photon energy and wavelength respectively. The cross section of this interaction is given by the Klein-Nishina differential cross

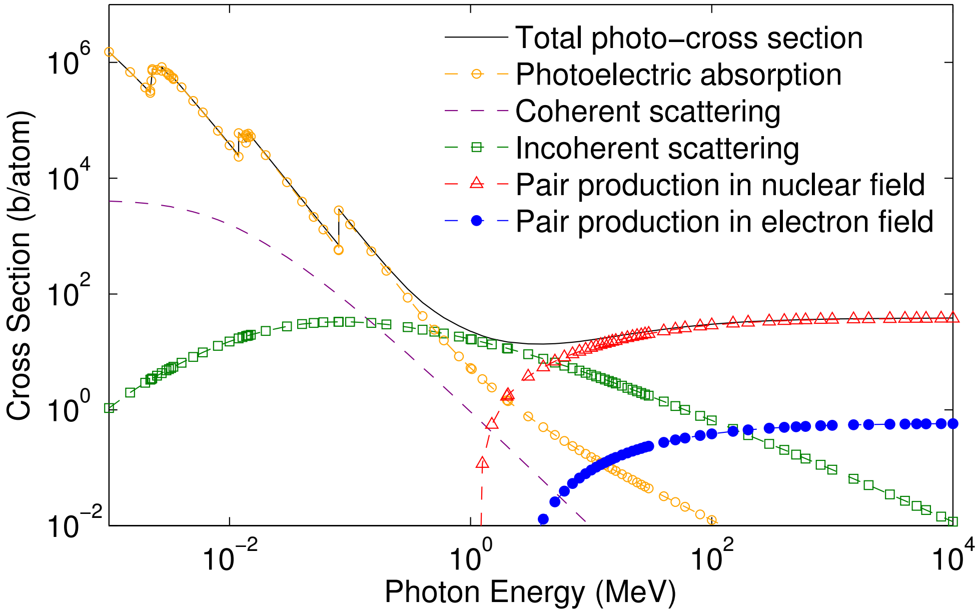

Figure 2.9: Photoabsoprtion cross section for gold for all relevant physical processes in the range of 1 keV to 1 GeV. Data taken from NIST Photon Cross Sections Database [52].

section,

$$\frac{d\sigma}{dk} = \pi r_0^2 \frac{mc^2}{k_0} Z \left(1 + \frac{k^2}{k_0^2}\right)\left(1 - \frac{k \sin^2\theta}{k_0 + k^2/k_0}\right). \tag{2.57}$$

Substituting the scattered photon energy in Eq. (2.56) into Eq. (2.57) gives [53]

$$\frac{d\sigma}{d\theta} = r_0^2 Z \frac{1+\cos^2\theta}{2[1+\gamma'(1-\cos^2\theta)]^2}\left\{1 + \frac{\gamma'^2(1-\cos\theta)^2}{(1+\cos^2\theta)[1+\gamma'(1-\cos\theta)]}\right\}, \tag{2.58}$$

where $\gamma' = k_0/mc^2$. Equations (2.57) and (2.58) are known as the Klein-Nishina formula which give a measure of the relative probability of Compton scattered photons at a given angle and energy.

The formulations of pair production at relevant energies were discussed in Chapter 2.1.2, and will not be covered again, except to say that, as seen in Fig. 2.9, pair production by free electrons is a factor of Z^2 below that of the nuclear charge.

The scattering processes described in this chapter are heavily dependent on approximations of the cross sections. Parameterizing these processes can yield high-accuracy results

Photons	Electrons and Positrons	Atomic
Photoelectric effect Rayleigh scattering Compton scattering Bethe-Heitler pair production	Energy loss by ionization Coulomb scattering Bremsstrahlung	Fluorescence Line radiation Auger electrons

Table 2.1: List of particle processes for the 'Standard Physics List' in Geant4. Only the photon-ion (Bethe-Heitler) pair production process is included.

over a wide range of conditions. The coupled creation and transport problem of pair generation can best be modeled by a Monte Carlo code where here, we have chosen to use Geant4 [54, 55]. Geant4 is an object-oriented toolkit for the simulation of particles passing though matter and managed by a collaboration which began at CERN (European Organization for Nuclear Research) in 1993. Geant4, originally designed for high energy physics, has a flexible 3D cartesian geometry and interchangeable physics packages based on the needs of the simulation, extendable down to thermal energies. The physics models used have been exhaustively benchmarked for all physics subcategories within electromagnetic and hadronic interactions [56–58].

The "standard physics" package option are electromagnetic models optimized for accuracy above the absorption edges of materials (∼100 keV) up to the TeV energy level. All scattering processes can be controlled independently with a comprehensive list of the individual physics components listed in Table 2.3. The cross section databases have been validated for particle interactions with cold matter and do not have beam interactions such as space-charge and collective effects. Although the front and rear surface of a target subjected to an ultraintense laser is dominated by collective physics with high fields, the interaction within the target can be reduced to particles traversing cold material. A Monte Carlo code such as Geant4 is ideally suited to model this physics. The front surface, laser-matter interaction physics was described in the previous sections, while the physics of the rear surface is covered in the following.

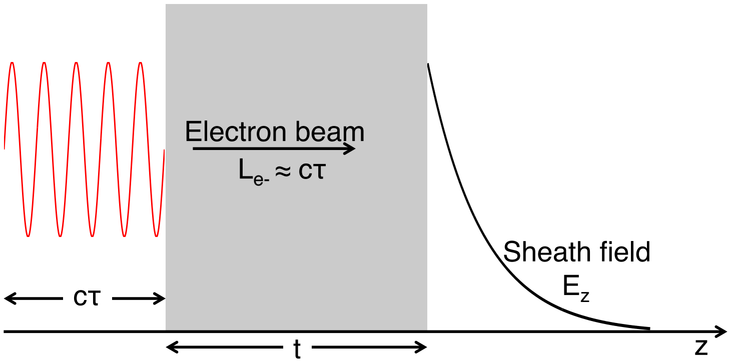

Figure 2.10: Schematic of sheath field development on the rear surface of a target. Relativistic electrons stream through the target and create a charge imbalance where the sheath electric field accelerates positive particles at the edges and rear target normal direction.

2.4 TNSA Positrons

The large charge buildup and beam currents created in direct laser-target interactions significantly affect the characteristics of emitted positrons. The main pulse of the laser interacts with a preformed plasma near the critical surface and creates a large flux of relativistic electrons with a conversion efficiency of 20–40% [59]. The target is nearly transparent to the hot electron cloud that propagates beyond the rear side to create an electric field gradient between the target and cloud. Positively charged particles on the surface of the target feel this sheath potential and are accelerated into the electron cloud, reducing the field magnitude over time. Because of the finite inertia of the electrons, the accelerated positive particles eventually catch up and propagate together. This process is know as target normal sheath acceleration (TNSA) [60] and was first used to describe the observation of high energy protons and ions from some the earliest experiments using relativistic laser intensities [61, 62]. A sketch of the process is shown in Fig. 2.10.

We can estimate, using a very simple model, the magnitude of the accelerating field, $|\mathbf{E}|$, by assuming a characteristic temperature of the hot electrons, T_{hot}, and knowing the plasma scale length, L, where

$$|\mathbf{E}| = \frac{T_{\text{hot}}}{eL}. \tag{2.59}$$

The ponderomotive scaling for a laser operating at 10^{19} W/cm^2 is $T_{\text{hot}} = 5$ MeV. The plasma scale length on the rear surface is given by hydrodynamic expansion of the ions and related to the ion sound speed. A long scale length acts to inhibit acceleration from the electron cloud where the most efficient TNSA occurs when the rear target surface has a steep ion density gradient (i.e., at early times before the target blows down). Positron production has a temporal duration on the order of the fast electron lifetime, which is approximately the laser pulse length. At the tail end of a 1 ps laser striking a gold target, the scale length is

$$L = \tau c_s = \tau \sqrt{\frac{Z T_{\text{hot}}}{m_i}} = 14 \ \ \mu\text{m}, \tag{2.60}$$

where m_i is the ion mass. For this simple model, we can see that the TNSA acceleration can reach up to a ~MV/μm for short pulses and high electron temperatures. Positrons, following very closely behind the hot electrons, exit the target before the sheath has time to decay and is effectively accelerated by a static potential. This feature of positrons make the mean energy of their energy spectrum a direct measurement of the peak sheath potential. A more complicated model would take into account the rear plasma cooling, shape of the density gradient, and the finite inertia of electrons compared to ions.

To demonstrate the complexity of the sheath field buildup and associated magnetic fields of the particle currents, an example using the self-consistent particle-in-cell code LSP was used to simulate an ultraintense laser incident on a thick gold target. A surrogate 10 ps laser pulse produced an exponential electron distribution with 550 J of beam energy and a temperature of $T_{\text{hot}} = 4.5$ MeV. The electrons were initialized in the forward z direction with unique temporal, angular, and energy components derived from a separate laser-plasma interaction simulation. All electrons originated from a 5 μm spot size on the surface of a 1 mm diameter, 1 mm thick gold target in a 2D cylindrically symmetric geometry ($\hat{r}$-$\hat{z}$) and three vector dimensions $\left(\hat{r}\text{-}\hat{\theta}\text{-}\hat{z}\right)$ which described the electromagnetic fields. A particle-in-cell code propagates energy and mass through a grid structure obeying Maxwell's equations where collisional interactions are governed by Monte Carlo databases. Additional details about the simulation can be found in Ref. 10 and 63 where all LSP simulations were done by Dr. Anthony Link. A snapshot of the region around the target at 12.5 ps after the arrival

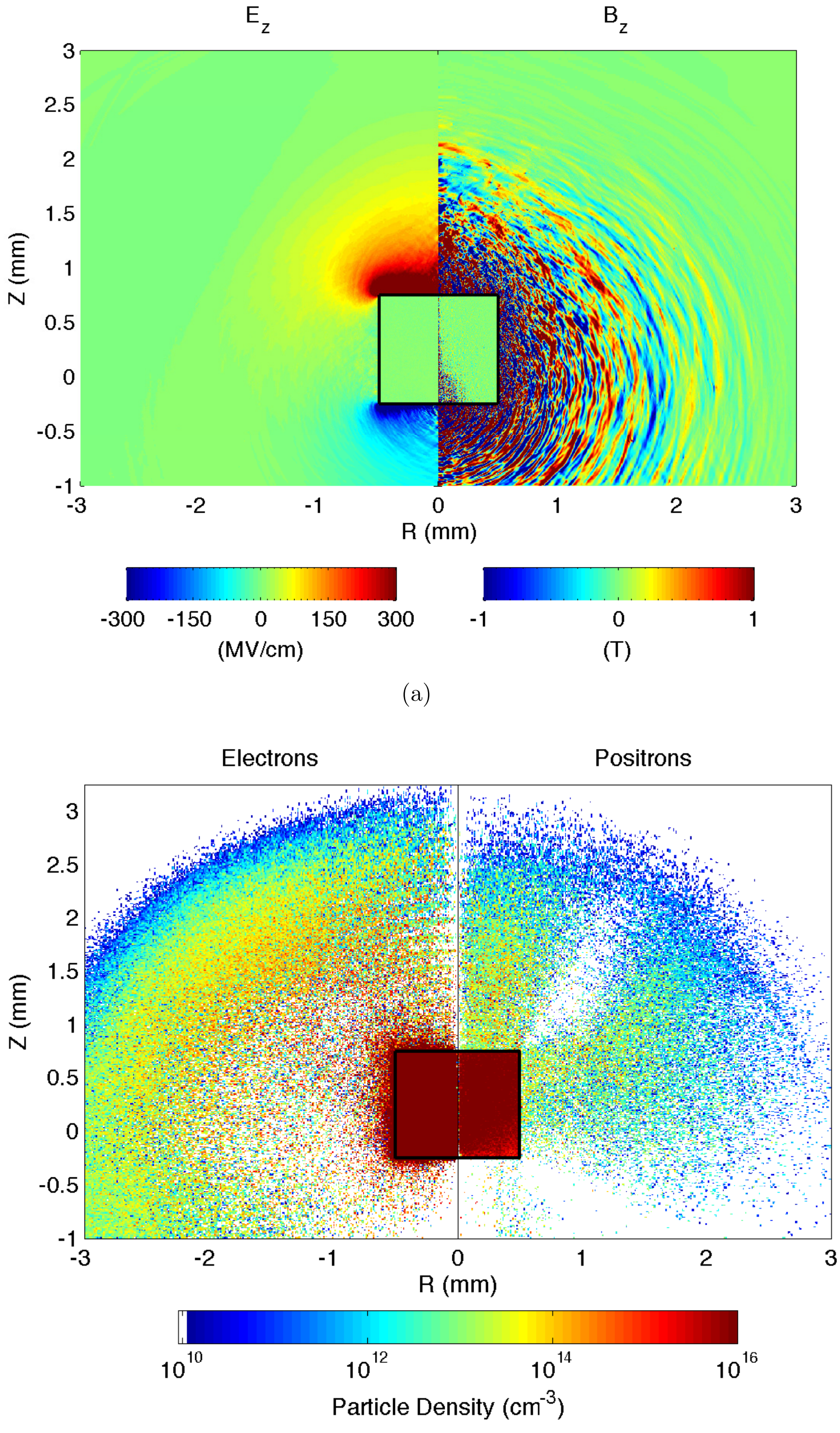

(a)

(b)

Figure 2.11: (a) Electric and magnetic fields for a surrogate Titan laser electron source on a gold target (outlined in black) at 12.5 ps from a 2D 3V LSP simulation. (b) Electron and positron densities for the same source. Simulations courtesy of Tony Link.

of the laser pulse is shown in Fig. 2.11.

From Fig. 2.11(a), the axial electric field is of the order 1 MV/μm, as predicted, and has a near-uniform distribution over the rear surface extending over a few hundred microns. The magnetic fields generated by the escaping electrons show very fine and complex structure. Because of the modest magnitude (~1 T) and small spatial extent, however, the electric fields dominates the equation of motion of the positively charged particles.

Fig. 2.11(b) shows the electron and positron densities around the target. Fast electrons stream through the target into a large cloud emitted into high angles. The large electron densities on the outer surface of the target establishes the sheath field. This sheath field also acts to recirculate electrons with energies below that of the field magnitude back into the target. This cutoff energy and recirculation is well explained by a capacitor model [64] and effectively truncates the flux of low energy electrons during the first half of the laser pulse duration. The vast majority of the positrons generated do not escape the target where it is only those particles that reach the back surface who feel the uniform, target-normal acceleration gradient. It is also of note that the positrons are temporally and spatially delayed from the electrons and will copropagate. For these densities and temperatures, the Debye length is on the order of 1 mm and the number of particles within a Debye sphere is around 10^{11}, constituting a non-neutral pair plasma [9].

Positron momentum is controlled mainly by the sheath field and as such has a narrow divergence from the rear while a small positron population is also ejected radially from the edges of the target. An absence of positrons around a ±45° cone is evident, near the corners, demonstrating that the emission is in the target-normal directions.

The magnitude of the sheath potential can also be investigated by comparing measured data and Monte Carlo simulations, which do not take into consideration collective field effects. A 5 MeV electron source incident on a 1 mm thick gold target was modeled where the total number of positrons created within the target and the number exiting the target were measured. These three spectra can be seen in Fig. 2.12. Positrons that migrate to the outer surfaces of the target have a distribution peak at 2 MeV. The peaked shape comes from the nonlinear effect of collisional energy loss for low energy positrons and electrons. This simulation result is compared to experimental data which records the positron peak

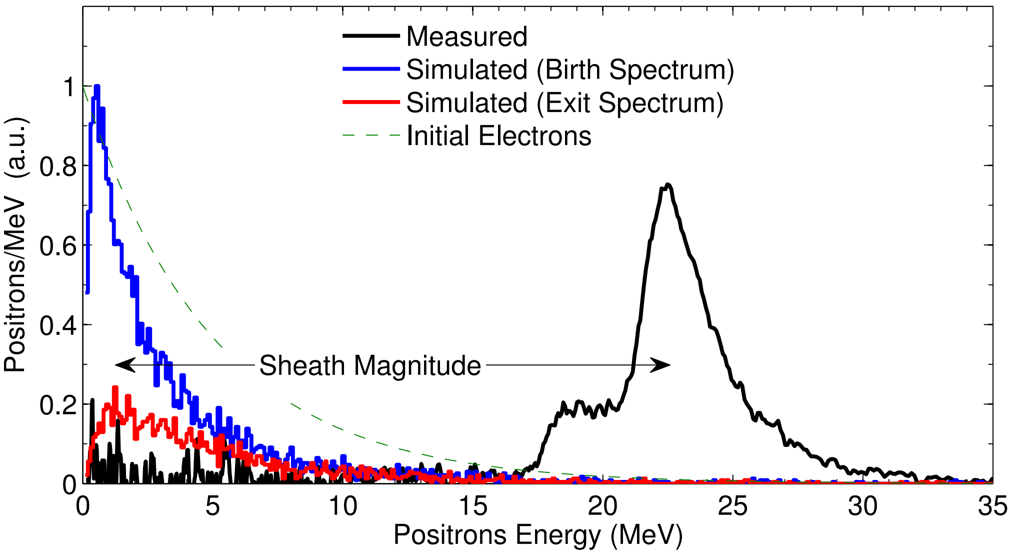

Figure 2.12: Positron production results from a Monte Carlo Geant4 simulation of a 5 MeV electron beam incident on a gold target. The positrons are born with a near-exponential spectrum (blue), reflecting the electron source, while positrons that are emitted from the target (red) are shifted out in energy by 2 MeV. Experimentally measured positrons (black), using the same target geometry and similar electron source, shows spectrum with a peak at 22 MeV.

energy to be 22 MeV. The 20 MeV energy gain comes from the TNSA fields which can be controlled by two experimental factors: the target size and electron beam properties. The relationship between peak energy location and the rear target surface area, S, was shown to be $E_{\text{peak}} \propto 1/S$ [7]. The number of electrons passing through the target, according to a capacitor model, linearly increase the sheath field by $E_{\text{peak}} = e^2 N_{e^-}/C$ where C is the effective dynamic capacitance of the target [64].

The combined effects of modifying both electron flux and target surface area is shown in Fig. 2.13. As the target dimension decreases from a 10 mm radius to 1 mm ('A' to 'B'), the mean energy of the emitted positrons increases while maintaining roughly the same total number of observed particles. Increasing the electron flux, assuming a nominally constant laser conversion efficiency, leads to a further shift upwards in peak energy while also increasing the total positron yield ('C'). The laser energy, indirectly, dictates the divergence angle of the positron beam. Since TNSA only accelerates longitudinally, the transverse component of the momentum remains constant. That is, the emittance of the beam stays

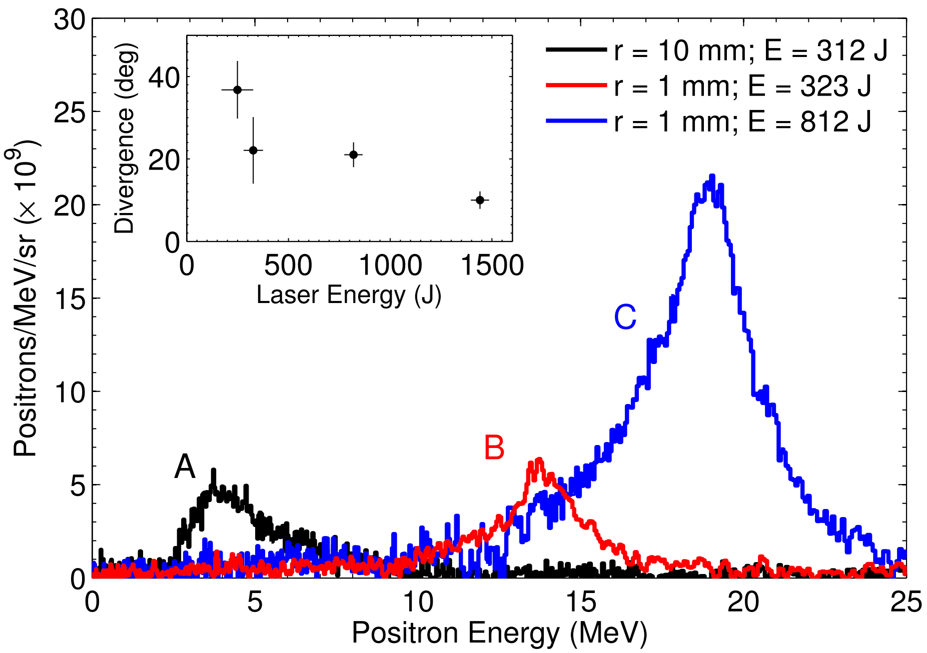

Figure 2.13: Experimental positron spectra from a 1 mm thick gold target with varying radial dimensions using the Omega EP laser with a pulse duration of 10 ps. Divergence angle of the beam (inset) is highly influenced by the mean energy of the positrons. Figure adapted from Ref. 7 and inset adapted from Ref. 63.

constant while the divergence angle decreases (see inset of Fig. 2.13) [8].

The accurate control of positrons, both spectrally and spatially, is critical to the future application of laser-produced positrons. Manipulating the TNSA effect is the largest tool towards this goal, where we will see in the later chapters of this dissertation, externally applied magnetic fields can also provide a significant amount of control.

CHAPTER III

Experimental Design

This chapter discusses the experimental facilities, diagnostics, and methods used to obtain the results described in this dissertation. The Titan and Callisto laser systems were primarily used for this work while both the Omega EP and LFEX lasers hosted complementary experimental campaigns. An existing electron-positron-proton spectrometer was the principal charged particle spectrometer, while novel designs of a transmission crystal and step filter spectrometers were developed specifically for this project to diagnose high-energy x-rays. The construction and application of a large-scale, high-field Helmholz coil is also described.

3.1 Laser Platforms

The data and results described in this dissertation were performed on two laser systems whose final pulse parameters differ significantly yet are amplified by the same platform, namely the Janus laser at the Jupiter Laser Facility. The Janus laser bay services up to three target areas with an amplified ns-long pulse centered at 1054 nm. The front end is a commercial GLX-200 master oscillator producing 300 fs pulses (with 6 nm of bandwidth) at a repetition rate of 82 MHz. A two-pass reflecting diffraction grating stretcher increases the pulse duration to 2.2 ns in order to be amplified by a process known as optical parametric chirped pulse amplification (OPCPA). Chirped pulse amplification (CPA) [65] is used to create high-power lasers while keeping its intensity below the damage threshold of downstream optics. The basis of CPA is to temporally stretch a pulse, decreasing the average intensity,

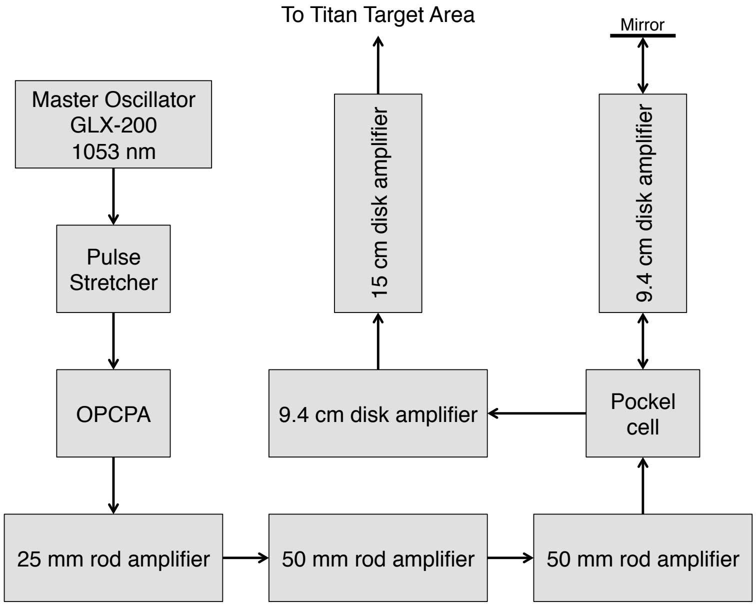
To Titan Target Area
Mirror
Master Oscillator
GLX-200
1053 nm
Pulse
Stretcher
OPCPA
15 cm disk amplifier
9.4 cm disk amplifier
9.4 cm disk amplifier
Pockel
cell
25 mm rod amplifier
50 mm rod amplifier
50 mm rod amplifier

Figure 3.1: Block diagram of the Janus front end and amplifier chain.

followed by amplification and recompression. Without first stretching the pulse, high intensity pulses traveling through the amplifying medium (Nd:glass in this case) will self-focus, creating hot spots in the beam and damage to the optic. Before CPA the state-of-the-art laser technology could only achieve intensities of 10^{15} W/cm^2 since the only other method to avoid damaging nonlinear effects was to scale the size of the optics, a prohibitively expensive solution.

Optical parametric amplification (OPA) is used in conjunction with CPA to increase the gain bandwidth in the pump lasing material. For the Janus system, the stretched seed pulse is cotimed to a pump beam that crosses within a nonlinear β-barium borate (BBO) crystal. The pump energy is parametrically converted to the seed energy within the crystal, facilitated by an idler beam to conserve energy in an intensity-dependent process. In amplifiers, for which the gain medium is also the lasing medium, amplified spontaneous emission (ASE) will produce small levels of energy before and after the seed pulse. After compression, pedestals or prepulses caused by ASE can be intense enough, once focused, to ionize the front layer of a target and create μm-scale plasmas.

The OPCPA beam in Janus is amplified in series through three rod amplifiers and sent into a Pockel cell whose polarization allows the beam to be transmitted. A block diagram is shown in Fig. 3.1. After two passes through a 9.4 cm disk amplifier, the Pockel cell is switched to send the beam through two additional disk amplifiers before entering the switchyard which routes the beam to the various target areas at JLF. At this point the beam is spectrally chirped with energies of up to 600 J in 1 ns and a diameter of 20 cm. The final amplifier chain imposes significant thermal lensing to a beam in the gain medium after the flashlamps fire. The disk amplifiers are therefore cooled using air jets that run for approximately 10 minutes, followed by cooling in ambient air. The minimum time between shots is determined by the heat capacity and is set to one shot per 30 minutes.

3.1.1 The Titan Laser

The Titan laser at JLF [4] operates at a wavelength of 1054 nm and a pulse length between 0.7-10 ps with maximum energies between 150 J (0.7 ps) and 350 J (10 ps). A long-pulse beam (a few ns in duration) is delivered from the JLF main laser bay through an overhead beam pipe into a mezzanine in the Titan target chamber room. The chirped beam enters a vacuum chamber holding 60×30 cm^2 dielectric reflective diffraction gratings arranged to do the inverse function of the stretching performed in the laser bay before the final amplification chain. The laser enters the target chamber after the four-bounce compressor and two turning mirrors.

The Titan target chamber is a 2 meter diameter, 1 meter tall cylindrical vacuum vessel with a mechanically isolated optical table. The 40 ports around the perimeter of the chamber and on the pitched ceiling give ample flexibility for externally mounted diagnostics where the only obstruction in the chamber is the laser beam path and the focusing optic, a $f/3$ off-axis parabola (OAP). The best-focus spot size of 10 μm FWHM is approximately twice the diffraction limit of 6.4 μm. The beam enters the chamber on a south-to-north axis with the final focusing rotated by 15 degrees. A layout of the Titan chamber room is given in Fig. 3.2.

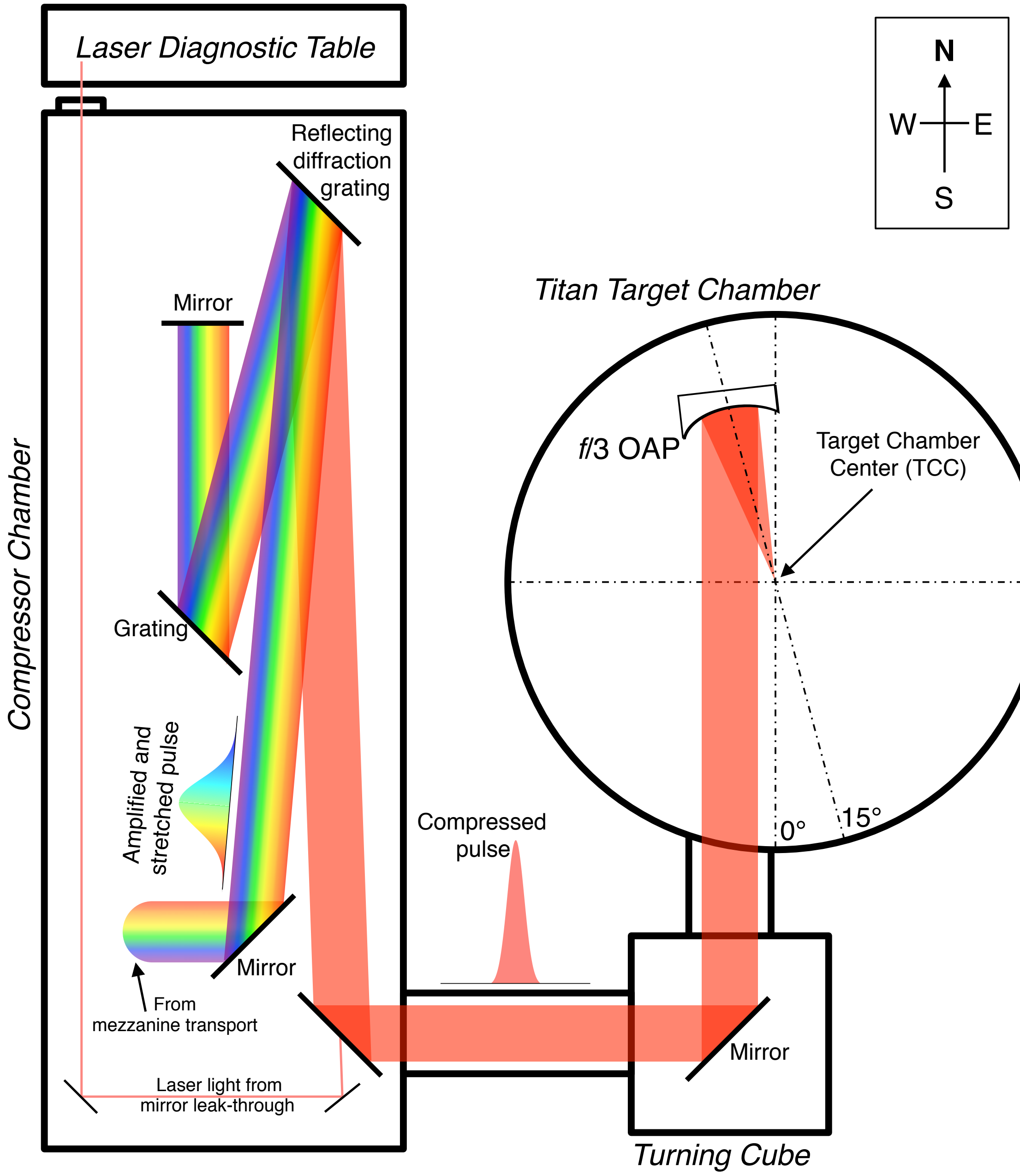
Laser Diagnostic Table
Reflecting diffraction grating
Mirror
Grating
Compressor Chamber
Amplified and stretched pulse
Mirror
From mezzanine transport
Laser light from mirror leak-through
N
W
E
S
Titan Target Chamber
f/3 OAP
Target Chamber Center (TCC)
Compressed pulse
0°
15°
Mirror
Turning Cube

Figure 3.2: Titan laser target area layout, showing the west beam compression and transport into the target chamber. A stretched and amplified pulse is relayed from the laser bay at air pressure into the room, arriving in a diagnostic mezzanine. The beam is directed down into a vacuum chamber and is dispersed in the opposite direction to temporally compress the pulse. The laser is aligned through a turning cube and focused by an off axis parabolic mirror within the target chamber. Layout is approximately to scale.

3.1.2 The Callisto Laser

The Callisto laser is another target area within the Jupiter Laser Facility at LLNL, delivering an ultrafast (fs) pulse with peak powers up to 200 TW. The front end of Callisto is a standalone titanium sapphire oscillator emitting a few nJ of laser energy per pulse at a central wavelength of 800 nm at a repetition rate of 82.2 MHz. The large bandwidth of approximately 40 nm is an intrinsic feature to the gain medium and is directly proportional to the ultrashort pulse length of 30 fs. The master oscillator pulse is temporally shaped, amplified by a 5-pass amplifier to a few μJ per pulse, and stretched to a duration of 1 ns. It then passes through a regenerative amplifier, making 25 round trips, which produces a 1 mJ, 10 Hz pulse train. Another bowtie-layout 5-pass diode-pumped amplifier brings the beam up to 100 mJ per pulse. The energy for the final amplification is provided by the Janus laser system using roughly 100 J of frequency doubled laser light producing up to 20 J of energy per pulse. This pulse is recompressed using gold diffraction gratings, reversing the initial chirp imposed before the regenerative amplifier. The final parameters of the Callisto beam is a full width at half maximum pulse duration of 60 fs (bandwidth of 20 nm) and up to 15 J of energy. The beam is transported to a target chamber to be focused by an $f/8$ off-axis parabolic mirror to a spot size of on the order of 10 μm. These parameters correspond to a normalized vector potential of $a_0 \simeq 10$.

3.1.3 The Omega EP Laser

While none of the results presented in this dissertation use the Omega EP laser system, supplemental experiments and development of diagnostics were performed at the facility. The Omega EP (extended performance) petawatt laser [6] at the Laboratory for Laser Energetics (LLE) in Rochester, NY was designed to produce high energy x-rays and protons for radiographic purposes and as a platform for HED experiments. The two short pulse arms of EP begin as an OPCPA beam and amplified through booster and main amplifiers, both Nd:glass technology. After final amplification, the lasers are routed into a spherical, 2 meter diameter target chamber and focused by $f/3$ OAPs in an orthogonal geometry along the equator. Omega EP is capable of 800 J of on-target energy in 1 ps or 1.5 kJ in 10 ps, focused into a 20 μm spot size, all in the fundamental wavelength of 1054 nm.

3.2 Diagnostics

There are many standard laser, optical, x-ray, and particle diagnostics typically fielded for ultraintense laser experiments and the choice of instrumentation is optimized based on goals of the specific campaign. Here, we discuss the primary diagnostics critical to the positron-generation experiments, namely a charged particle spectrometer, transmission crystal x-ray spectrometer, and step filter x-ray spectrometer. The detector in all three cases is image plate, originally developed as an alternative to x-ray film for medical applications [66, 67] and quickly employed in experimental physics [68, 69]. Image plates (typically model Fujifilm BAS-SR or BAS-MS), which are sensitive to all types of ionizing radiation, are excellent choices for detectors because they can be reused and are robust against electromagnetic pulses with linearity and repeatability over a large range of particle energies and have high dynamic range. A large amount of absolute calibration work has been performed for electron [70–72], proton [73], and x-ray data [74–78].

3.2.1 Image Plate Detector and Scanner Calibration

Much of the work describing procedures of scanner calibration in this section are in part reprints of the material contained in the publication Williams et al. [79], where the dissertation author was the primary investigator and author of this paper.

The active layer of an image plate consists of a phosphor crystal [$BaF(Br_x,I_{1-x}):Eu^{2+}$] suspended in a plastic binder. Incident radiation further ionizes Eu^{2+} dopant atoms and generates photoelectrons which remain in a metastable excited state. These electrons recombine either through thermal excitation or after being stimulated, emitting a blue photon at a wavelength of $\lambda \simeq 390$. This process is called photostimulated luminescence (PSL). The blue light is then collected by a filtered photomultiplier tube (PMT) internal to a flatbed scanner. A rotating prism scans in the vertical direction and rasters horizontally to digitize the exposed image plate into a two-dimensional image. The image plate has a ferromagnetic backing layer which holds it to a 20 × 40 cm^2 magnetic tray allowing for arbitrary detector

Image plate type	A_1 (PSL)	τ_1 (min)	A_2 (PSL)	τ_2 (min)	y_0 (PSL)
MS	0.175 ± 0.009	23.0 ± 2.7	0.315 ± 0.009	615.9 ± 42.1	0.511 ± 0.005
SR	0.436 ± 0.016	18.9 ± 1.5	0.403 ± 0.013	1641.5 ± 152.3	0.162 ± 0.010

Table 3.1: Double exponential fit coefficients for empirically derived image plate fading factor at ambient room temperature. Data taken from Ref. 77.

geometry.

Since metastable electrons can be de-excited by thermal noise, the ambient temperature and time between exposure and scan are important considerations in the calibration of the data. In addition, the conversion from PMT signal to physical dose units is dependent on scanner spatial resolution, digital precision, and PMT voltage gain (sensitivity). Image plate signal decay has been expressed as a two-component exponential of the form $f(t) = y_0 + A_1 e^{-t/\tau_1} + A_2 e^{-t/\tau_2}$ with coefficients given in Table 3.1 for the two image plate types used in these studies [77]. The sensitivity of the image plates depends on the incident particle species. Electrons (and positrons) have a nearly constant sensitivity curve between 1 and 1000 MeV, spanning the energy bandwidth of interest for pair production studies. Image plates become less sensitive as photon energy increases while retaining enough resolution to measuring the peak bremsstrahlung radiation created by relativistic electrons (∼100 keV). A summary of the simulation and data of the sensitivity function for photons on MS image plate is shown in Fig. 3.3.

The standard image plate scanner used in experimental physics facilities is the Fuji FLA 7000 flatbed scanner which compresses the pixel values logarithmically. The physical dosage units of PSL can be found with the conversion,

$$\mathrm{PSL}_{\mathrm{Fuji}} = \left(\frac{R_{\mu\mathrm{m}}}{100}\right)^2 \left(\frac{4000}{S}\right) 10^{L\left[F/(2^B-1)-\frac{1}{2}\right]}, \tag{3.1}$$

where $R_{\mu\mathrm{m}}$ is the pixel resolution in microns, S is the sensitivity setting (1000, 4000, or 10000), L is the digital precision (4 or 5), B is the dynamic range (8-bit or 16-bit), and F is the pixel value.

The scanning sensitivity is calibrated by creating a known exposure value on an image

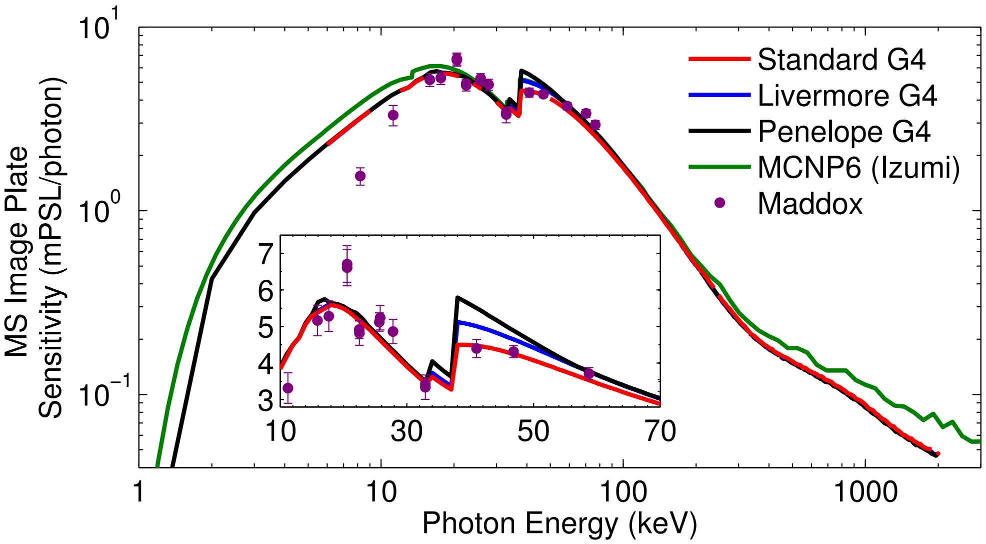

Figure 3.3: Calculated and measured sensitivity of MS image plate to incident photons. Geant4 calculations were repeated for the Standard, Livermore, and Penelope physics packages, where significant deviation occurs only around the barium K-edge at 37 keV (see inset). The Geant4 calculations are also compared to another Monte Carlo code, MCNP6, taken from Izumi et al. [78]. Data points are taken from Maddox et al. [77].

plate and compensating the PMT voltage of the scanner to match the expected PSL value. This is an important step, as it has been found that some Fuji FLA 7000 scanners are in need of recalibration after only three months. The standard calibration procedure uses MS image plate placed in direct contact to a carbon-14 impregnated acrylic sealed source with a 1 cm diameter active area with a total activity of 60 μCi for an exposure time of 20 minutes. After a 5 minute rest, away from the source and stored in a light-tight container, the image plate is scanned. This exposure procedure has a known value of 100 PSL/mm^2 or 0.25 PSL mean pixel value for a spatial resolution of 50 μm.

Recently, Fuji sold their image plate scanner business to GE Healthcare, which still manufactures the hardware albeit with small software changes which require a different conversion than Eq. (3.1). Instead of three discrete sensitivity settings, the GE Typhoon 7000 scanner allows the user to have direct control of the PMT voltage, ranging from 500–1000 V [80]. As well, the grayscale pixel values are compressed quadratically and stored as

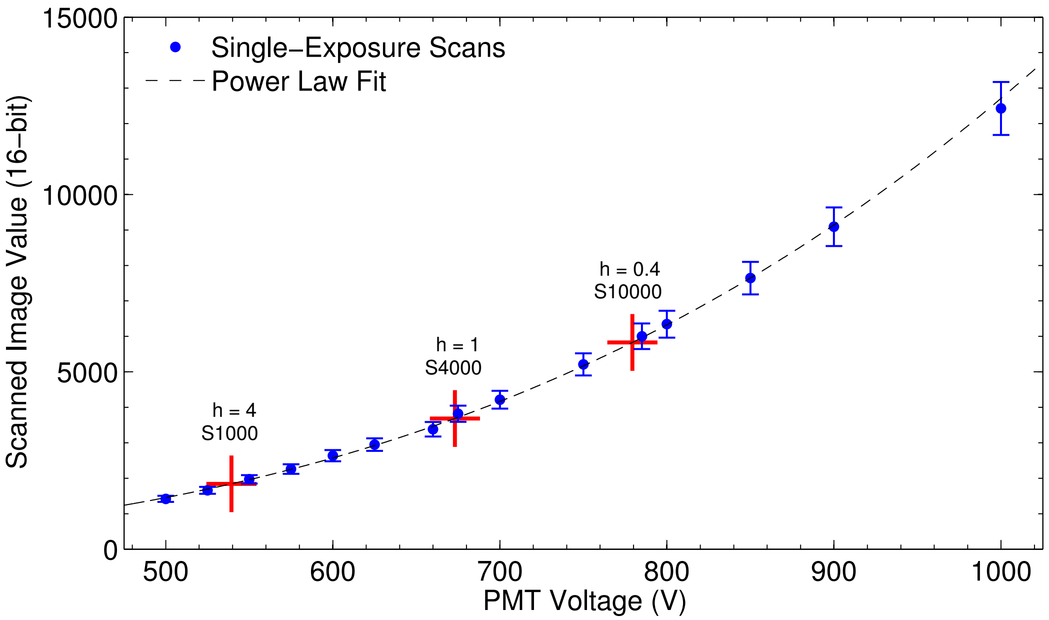

Figure 3.4: Grayscale image values (dots) for a 100 PSL/mm^2 dose for various PMT voltage settings on a GE Typhoon 7000 Image Plate Scanner. Fuji-equivalent sensitivity voltages are shown in red crosses. Power fit (dashed) allows for equivalent sensitivity calibrations at arbitrary voltage settings.

16-bit images. The conversion to PSL is then

$$\mathrm{PSL_{GE}} = \left(\frac{G}{2^{16}-1}\right)^2 \left(\frac{R_{\mu\mathrm{m}}}{100}\right)^2 h(V)\ 10^{L/2} \tag{3.2}$$

where $h(V)$ is the sensitivity response function of the particular scanner PMT and G is the pixel value. The exact value of h must be determined in order to directly compare data digitized at different facilities and to make absolute measurements. Here, it is convenient to make a connection with the more widely used Fuji sensitivity standard for backwards compatibility, where the $S1000$, $S4000$, and $S10\,000$, settings correspond to $h = 4$, 1, and 0.4, respectively. Using three GE scanners located at the National Ignition Facility at LLNL, the exposure procedure described above was repeated for various PMT voltages, with the results of a single scanner shown in Fig. 3.4, where the exposure was a known constant of 100 PSL/mm^2. An equivalent voltage can be found by solving Eq. (3.2) for the known dose, scan resolution, and latitude. In the case shown in Fig. 3.4 using the standard calibration source, $R_{\mu\mathrm{m}} = 50$, $\mathrm{PSL_{source}} = 0.25$ PSL/pixel, and $L = 5$ so that $G = 1843$, 3685, 5827 for

Source Activity (μCi/g)	Recorded Dosage (PSL/mm^2)	Corrected Dosage (PSL/mm^2)
Fuji Source	117.2 ± 9.3	100.0 ± 13.2
400	1051.2 ± 74.8	896.9 ± 96.0
280	835.2 ± 50.8	712.6 ± 71.6
220	662.0 ± 40.0	564.8 ± 56.6
117	364.8 ± 29.2	311.3 ± 35.2
51.6	184.8 ± 14.8	157.7 ± 17.8
35.0	104.0 ± 8.3	88.7 ± 10.0
18.4	76.8 ± 6.1	65.5 ± 7.4

Table 3.2: Results of cross-calibration scans between the Fuji (100 PSL/mm^2) and ARC sources. The recorded dose was scaled by 17.2% to match the expected calibrated dosage. Scanned dose readout was assumed to be linear so that the same procedure could be repeated for the ARC source to recover a corrected calibrated dosage.

h = 4, 1, 0.4 (S1000, S4000, S10 000) and have equivalent voltages of V = 539 V, 673 V, 779 V, respectively.

The GE Typhoon scanner has several advantages at low-signal levels. Due of the increased control over PMT voltages, an equivalent sensitivity on the order of S45000 can be reached at the highest gain setting, reducing the scanning detection threshold. The square-root compression also increases the resolution (PSL/δPSL) at low signal to resolve small variations. In the cases of high signal levels however, the GE scanner has decreased resolution and a lower sensitivity ceiling, which in cases where an S1000 equivalent voltage can not be achieved, may result in saturated images for signals that could be resolved in a Fuji scanner.

Procuring the Fuji-standard calibration source has recently been difficult and another radioisotope source was acquired in order to calibrate new or future image plate scanners. A carbon-14 standard on a plastic strip, containing 16 individual source regions, was chosen to replace the Fuji-standard source. This source was manufactured by American Radiolabeled Chemicals, Inc (ARC) [81] with carbon-14 impregnated paper squares 5 × 5 mm^2 with radioactive concentrations between 0.035 to 400 μCi/g and a total activity of 20 μCi. A schematic of this source is shown in Fig. 3.5(b). A cross-calibration scan was performed using the exposure technique described above with both the Fuji and ARC sources and,

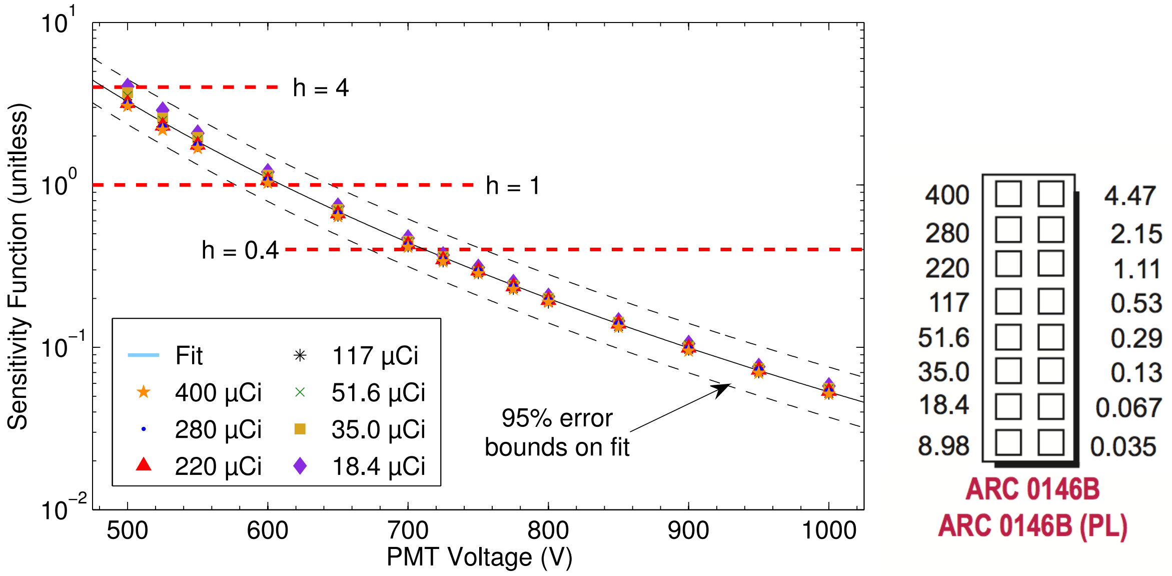

(a) (b)

Figure 3.5: (a) Scanner sensitivity function for a GE Typhoon 7000 scanner at ILE (markers). Equivalent-sensitivity voltages are shown (red dashed) corresponding to $h = 4$, 1, and 0.4. A power law fit provides calibrated dose conversion for arbitrary PMT voltage settings. The confidence bounds on the fit (black dashed) reflects the 8% uncertainty in the digitization process.
(b) Diagram of the ARC source, noting the radioactive concentration of the ^{14}C-impregnated patches. Image taken from the ARC catalog [81].

since the scanner used was consistently over-reporting the dose from the Fuji source, the measured results were normalized to the expected value and summarized in Table 3.2.

A GE Typhoon 7000 image plate scanner was calibrated using the ARC source at the Institute of Laser Engineering (ILE) at Osaka University, Japan. The sensitivity function of the scanner was determined by simultaneously fitting the image pixel values, G, to a power law function where

$$h(V) = \mathrm{PSL}^{i}_{\mathrm{ARC}} \times 10^{-L/2} \left(\frac{2^{16}-1}{G}\right)^{2} \left(\frac{100}{R_{\mu\mathrm{m}}}\right)^{2} \tag{3.3}$$

and $\mathrm{PSL}^{i}_{\mathrm{ARC}}$ is the ith activity of the ARC source. The continuous sensitivity function is shown in Fig. 3.5(a), where the confidence bands in the fit correlate to the roughly 8% uncertainty in the digitization process, as measured by the standard deviation of the mean pixel value from repeated scans of identical dosage. For the case of the ILE scanner, $h =$

$3.5(\pm 0.1) \times 10^{16}\ V^{-5.9\pm 0.1}$.

3.2.2 Electron Positron Proton Spectrometer (EPPS)

In the pair-generation experiments presented here, all positrons are detected directly using a time-integrated, absolutely calibrated charged particle spectrometer [71]. This spectrometer, referred to as the electron, positron, proton spectrometer (EPPS), is an established diagnostic and copies of the original design are qualified as facility diagnostics at the Omega facility at LLE, Orion facility at the Atomic Weapons Establishment in Aldermaston, England, and the NIF at LLNL. It was built specifically to simultaneously measure multiple species of charged particles produced in laser-generated pair experiments, where the accelerated electrons streaming though the target and emitted positrons provide a measure of the initial condition and final result of the experiment, respectively.

The principle of species separation relies on the differing charge-to-mass ratio of the electron, positron, and proton. Charged particles entering a constant, orthogonal magnetic field will undergo cyclotron motion given by the Lorentz force, $\mathbf{F}_B = q(\mathbf{v} \times \mathbf{B})$, which is balanced by centripetal force. For relativistic particles, the mass is adjusted by the Lorentz factor and we define $\beta = v_{\perp}/c$ such that

$$r = \frac{\gamma \beta m c}{q|\mathbf{B}|}. \tag{3.4}$$

Then, as particles enter the magnetic field region of the spectrometer, positrons and protons will curl one way while electrons curl the other.

The EPPS was designed to have relatively high resolution over the central energy region of interest in ultraintense laser-matter interactions of ∼1 to 30 MeV. Two pairs of $2 \times 2 \times \frac{1}{2}$ in^3 neodymium magnets, with a maximum field strength of 0.7 T, are installed inside a soft carbon steel alloy yoke to mechanically hold the magnets while constraining the magnetic field within the spectrometer housing. The magnetic field strength varies by 10% of the maximum value at the center where the two magnets butt against each other. When fielded on experiments, the steel housing is typically placed inside a lead enclosure, 25 mm thick on all sides except for the front, where the shielding is 50 mm thick with a collimation aperture

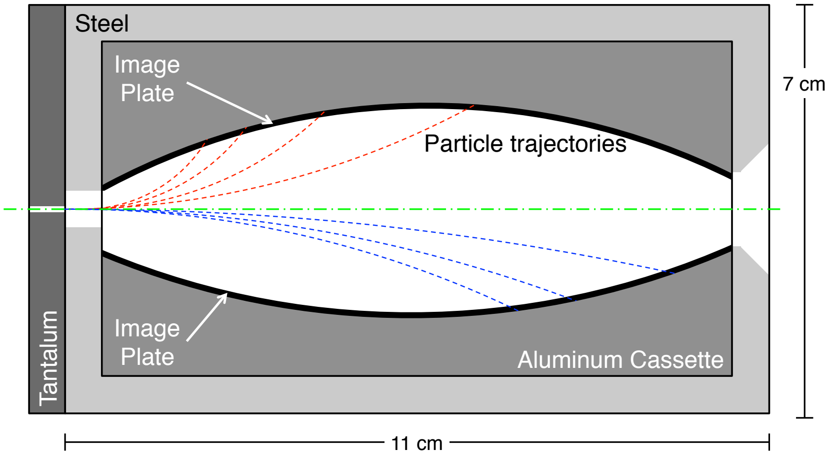

Figure 3.6: Physical layout of the EPPS core showing example particle trajectories (dashed lines) deflected by the magnetic field to hit the image plate detector. The image plate is held by an aluminum cassette away from the walls of the core to ensure and fluorescence background is isotropic. The compact design minimizes the area consumed by the diagnostic in the target chamber. The permanent magnetics sit above and blow the aluminum cassette, in and out of the page for this diagram

6.3 mm wide (dispersion direction) and 25 mm tall. An adjustable tantalum slit assembly, 6.3 mm thick, attaches to the front of the steel housing that acts as the final aperture, typically set to be 1 mm wide in the dispersion direction. A cross section of the EPPS core is shown in Fig. 3.6. The energy coverage of the spectrometer varies for the mass and charge of the incident particle where electrons and positrons can be measured between 0.1–300 MeV and protons between 1–30 MeV. The energy resolving power, $E/\Delta E$, is determined by the aperture slit and detector resolution and varies nonlinear with energy. For a 1 mm entrance slit and 100 μm detector resolution, electrons and positrons with energies above 3 MeV have a resolving power between 100–300.

The detector plane is an arc length with a constant radius where the origin is offset asymmetrically from the centerline of the EPPS. This minimizes potential signal bleed in the detector pixel elements from a grazing incident particle while maintaining a very small form factor. The aluminum cassette holder keeps the image plate away from the steel walls such that any fluorescence signal from transmitted particles is relatively isotropic on the detector.

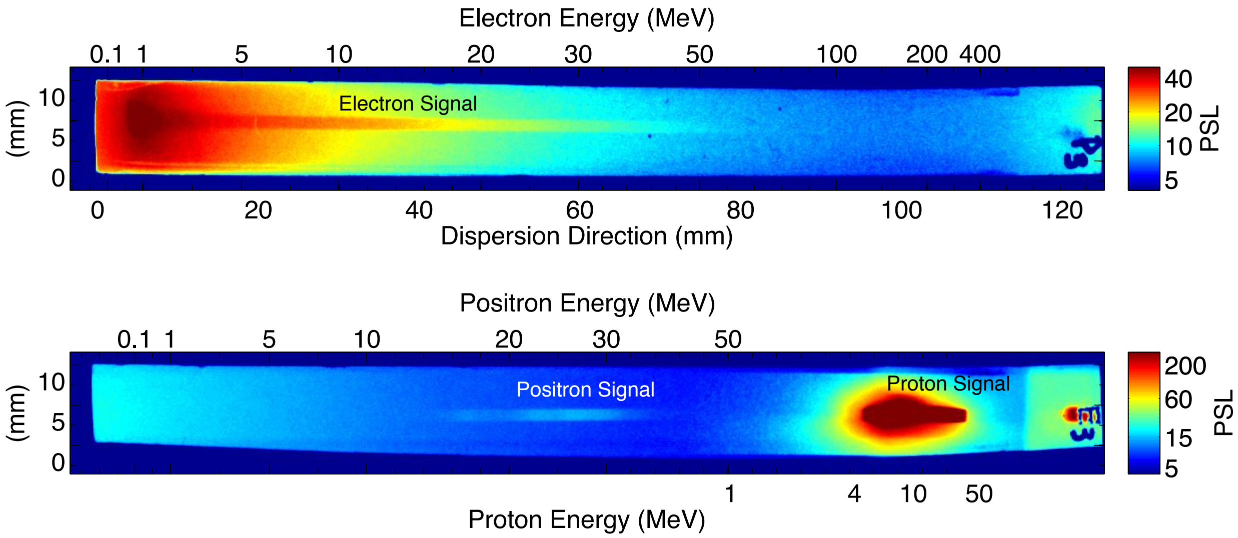

Figure 3.7: Typical raw image data from EPPS on SR image plate. Isotropic noise is seen at the low-energy portion of the image plate where particle and x-rays collide with the collimator and slit assembly. Electrons (top image) can be seen in the center of the image plate extending in a continuous spectrum out to 50 MeV. Positrons and protons (bottom image) have similar energies but appear at different positions due to their mass difference. For this scanning sensitivity, the proton signal was saturated. Data was taken from Omega EP shot 10189 for a 10 ps pulse duration delivering 1500 J of laser energy onto a 1 mm Au disk.

Figure 3.7 shows a typical example of the raw data from EPPS for a shot in which positrons, electrons, and protons were observed. Since the two detector planes have differing radii of curvature, the dispersion for positrons and electrons differ slightly in the low-energy region of the image plate. The proton signal is saturated for this shot where significant vertical bleed is observed. This is a function of the vertically-rotating prism in the image plate scanner where, for saturated signals, the scanner has greater spatial resolution in the horizontal direction. Each of the particle species appear near the center of the image plate with the total dose being a superposition of signal and background noise. Above and below these regions, the slit aperture ensures the dose is only background.

To extract quantitative information from an EPPS data shot, a lineout is taken of the signal area, D, and averaging over the size of the slit aperture, after rotating the image if necessary. A second lineout, of identical vertical size, is taken just below or above the signal region as a measure of the background dose, BG. Horizontally overlapping these lineouts

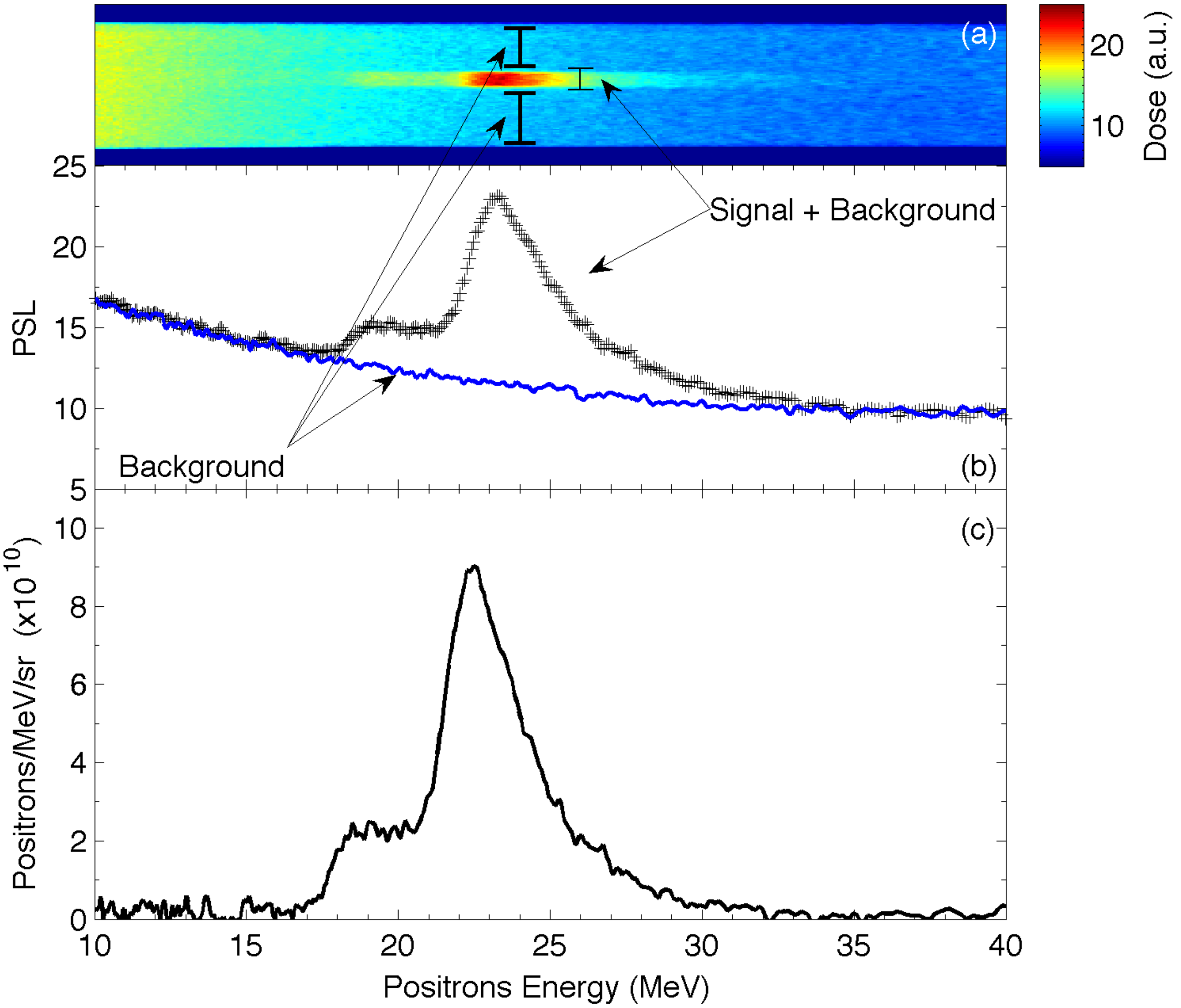

Figure 3.8: (a) Raw positron data from an Omega EP shot 20946 with the signal and background regions identified by black bars. The dispersion and color scale have been linearized.

(b) Lineouts of the signal (crosses) and background (solid) regions.

(c) Final reduction of the positron data folds in the detector solid angle, energy binning, signal width, and image plate fading factor and sensitivity. The total number of positrons can be found by integrating under the signal where, for this example and assuming the FWHM emission angle is 40° as reported by Ref. 7, $N_{e^+} = 4.7 \times 10^{11}$ positrons.

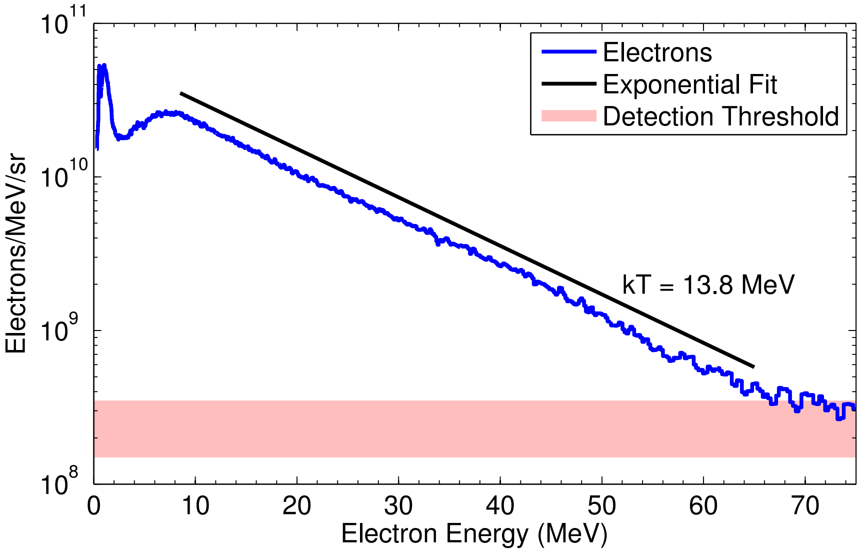

Figure 3.9: Typical electron spectrum measured by the EPPS. The high energy region is fit to an exponential function, offset in the plot for clarity. Data was taken from Omega EP shot 13451 for a 10 ps pulse duration delivering 430 J of laser energy onto a 100 μm Au disk.

and taking the subtraction of the two provides a measure of the signal-only dose on the image plate. Many times, the background signal can be well-represented by a double-exponential fit and is used to reduce the stochastic low-dose noise. The conversion to physical units in number of particles per unit energy per steradian is given by

$$\frac{dN}{dE} = \frac{1}{\Omega\ f(t)\ \Phi(E_i)} \frac{D_i - BG_i}{(E_{i+1} - E_i)}\ \Delta D_y, \tag{3.5}$$

where E_i is the ith dispersion energy, Φ is the energy-dependent image plate sensitivity, $f(t)$ is the time-dependent image plate fading factor, Ω is the geometric solid angle of the slit opening, and ΔD_y is the vertical width (in pixels) of the signal. The individual terms of Eq. (3.5) carry uncertainties between 5% and 15% with the total propagated error of ~20%. A full derivation of the uncertainty analysis is given in Appendix C. The analysis progression, from raw image plate to number of particles is visually shown in Fig. 3.8 for an example shot where positrons were observed from the target.

The total number and average energy of the positron (or electron) beam can be found by integrating under the region of signal where

$$N_{e^\pm} = \int_{E_1}^{E_2} \frac{dN_{e^\pm}}{dE'} dE' \tag{3.6}$$

$$\langle E_{e^\pm} \rangle = \int_{E_1}^{E_2} \frac{dN_{e^\pm}}{dE'} E' dE'. \tag{3.7}$$

The integration bound E_1 is nominally 2 MeV (the energy at which instrumentation noise significantly falls off) and E_2 is the energy at which the signal falls below the detection threshold of $\sim 10^8$ particles/MeV/sr. The positron signal, as seen from Fig. 3.8(c), has a near-Gaussian spectral shape imposed by the accelerating sheath potential, while the electrons have a exponential Maxwellian functional form. The characteristic temperature of the electrons is most evident on a log-linear plot. For a data set that appears linear in such a plot, a single-exponential decay coefficient is given by the slope of the fit line and is equivalent to the temperature. An electron spectrum featuring a Maxwellian high energy tail is shown in Fig. 3.9 with a temperature of 13.8 MeV, and 1.3 J of hot electron energy per steradian.

3.2.3 Gamma Crystal Spectrometer (GCS)

As electrons are a measure of pair production initial conditions, so too are the high energy x-rays indicative of positron generation via the Bethe Heitler process. The photometrics of the bremsstrahlung emission, as well as the positron annihilation radiation, can help qualify both pair production and laser-plasma interaction conditions. A challenge exists, however, to develop high resolution x-ray instruments capable of measuring high energy photons in laser-produced plasma experiments. This is due to the short-lived and high flux nature, where detector techniques such as scintillation or energy discriminating high purity germanium are overwhelmed by flux, and Compton electrons. Nuclear activation schemes fail to provide high enough resolution. A Laue transmission crystal spectrometer, in contrast, disperses high energy photons with reasonable efficiency and can use a time-integrated detector (e.g., image plate). Such a spectrometer was developed by Artep Inc., based on a Cauchois geometry

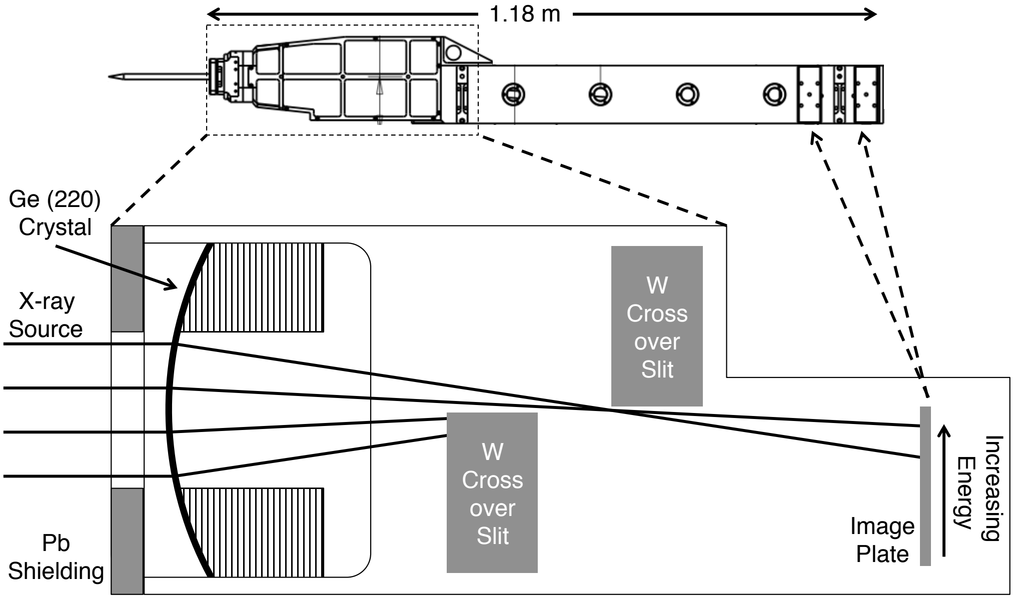

Figure 3.10: Geometric schematic of the GCS. Crystal geometry is rotated slightly within the housing to maximize the distance between crystal and image plate. An engineering drawing of the housing is shown above where the crystal and crossover slits are in the head of the instrument and the image plate is roughly 1 m behind the crystal in the rear.

[82] to measure very high x-rays in a footprint small enough to fit within the diagnostic cradle used by the Omega Laser Facility. A diagram of the instrument is shown in Fig. 3.10. This spectrometer, known as the Gamma Crystal Spectrometer (GCS), uses a cylindrically bent 400 μm thick Ge (220) crystal to resolve high energy photons in the range of 50 to 300 keV from a first order diffraction and greater than 600 keV in second order. This provides spectral coverage to include K_α and K_β transitions for mid-to-high Z elements and the 511 keV annihilation radiation. Bragg's law can be expressed $\sin\theta = n\lambda/2d$ where λ is the wavelength of the photon and θ_B is the Bragg angle. To maximize the spectral coverage, the crystal lattice spacing, d, must be minimized. The Ge (220) crystal used has a $2d$ spacing of 3.99 Å, which is nearly a factor of two smaller than other more common choices of crystals such as quartz (10-11) with $2d = 6.87$ Å.

Since Cauchois geometry spectrometers do not focus for point-like sources, the resolving power can be improved by placing the detector plane well behind the typical focal circle of

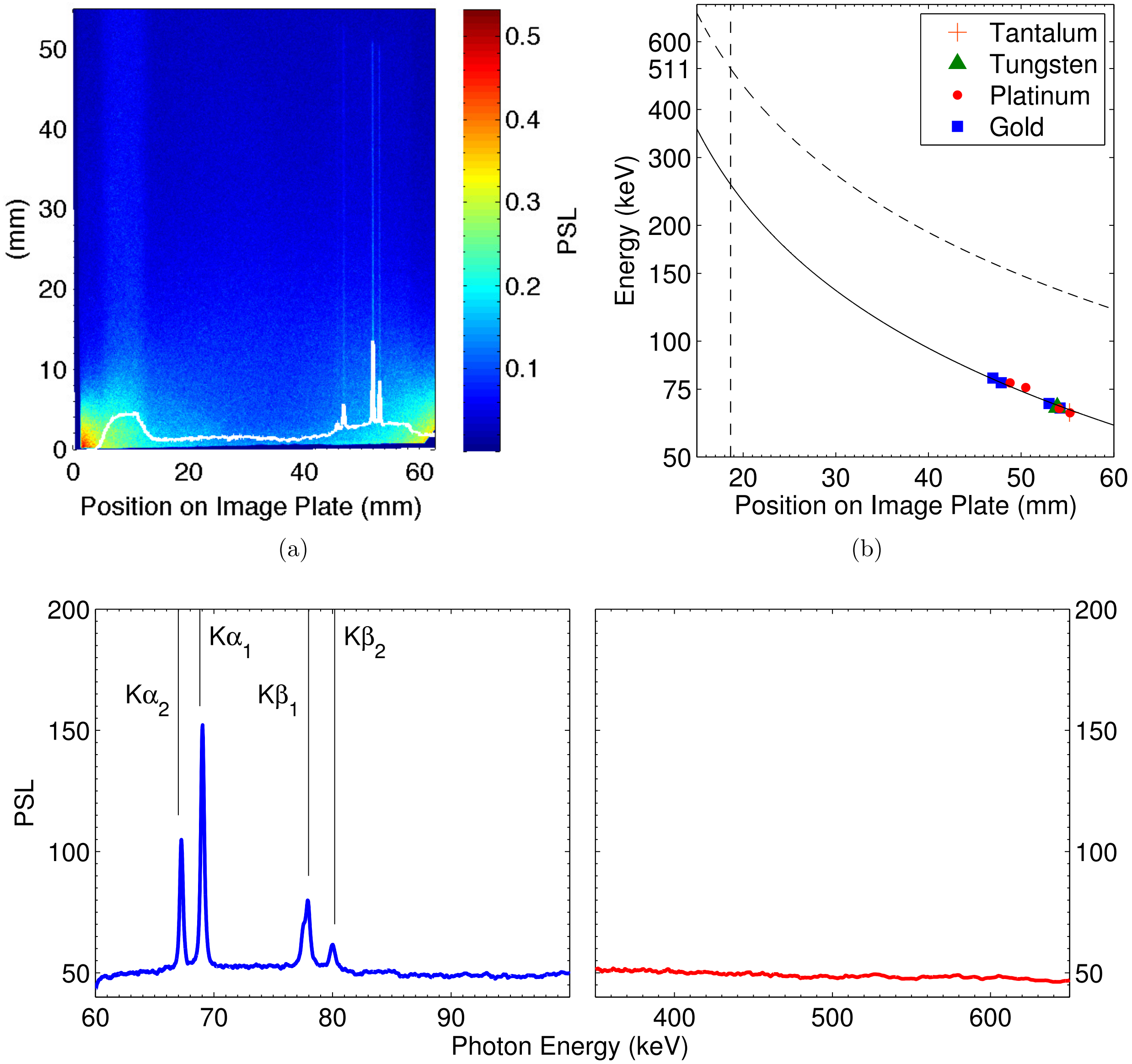

(a)

(b)

(c)

Figure 3.11: (a) Raw image plate data and a vertically averaged lineout (white) for a gold target. Signal from the cross over slits can be seen as a wide band near 10 mm while the signal near the bottom edge and corners are shielding fluorescence.
(b) Characteristic line emission from various targets are used to calibrate the analytic dispersion curve. Annihilation radiation at 511 keV can only be observed in second order.
(c) Data for a gold shot showing the K_α, K_β line emission (left panel) yet no evidence of the annihilation radiation (right panel). The laser energy was approximately 300 J in 10 ps.

the crystal [83]. The dispersion relation in this layout can be expressed as

$$X_d = R\left(\frac{n\lambda}{2d}\right)\left(1+\frac{D}{B}\right), \tag{3.8}$$

where R is the radius of curvature of the crystal, and D is the distance from the crystal to detector. B is a function of R and D_s, the distance from the source to crystal, given by

$$B = R\left(\frac{R+D_s}{R+2D_s}\right). \tag{3.9}$$

In order to observe the annihilation radiation with GCS, the detection threshold and background noise must be overcome. Using the sensitivity provided in Fig. 3.3 and assuming a 25 μm scanning resolution, MS image plate should be sensitive to a single 511 keV photon. However, the background originating from electrons colliding with the crystal and slit assembly and photons scattering within the housing contribute an average dose of 0.04 PSL, requiring roughly 200 photons per pixel element to overcome the noise. The solid angle of a detector element is 4.5×10^{-10} and the diffraction efficiency of a Ge (220) crystal is $\sim$30%. If we assume an isotropic distribution of the annihilation radiation, which would be the case for positrons that are contained and thermalize within the target, and that 90% of the positrons born are not emitted from the target, the pair generation yield must exceed 2×10^{13}. An example shot using a 1 mm Au target, irradiated by a 300 J 10 ps laser, is shown in Fig. 3.11 where strong line emission is observed but shows no evidence of the 511 keV annihilation radiation. Using generous approximations for this condition, we would only expect a pair yield of 1×10^{11}. For laser energies of 1500 J in 10 ps, the maximum pair production approaches the generation threshold of $\sim 10^{13}$ [10] but introduces significantly more noise and the GCS has yet to record signal consistent with annihilation radiation.

3.2.4 High Energy Step Filter Spectrometer (HERBI)

As described above, x-rays in the spectral range of keV to MeV are critically important in the diagnosis of HED conditions but also extremely difficult to measure. Complementary to the GCS, a second spectrometer was constructed that is well suited for the large photon en-

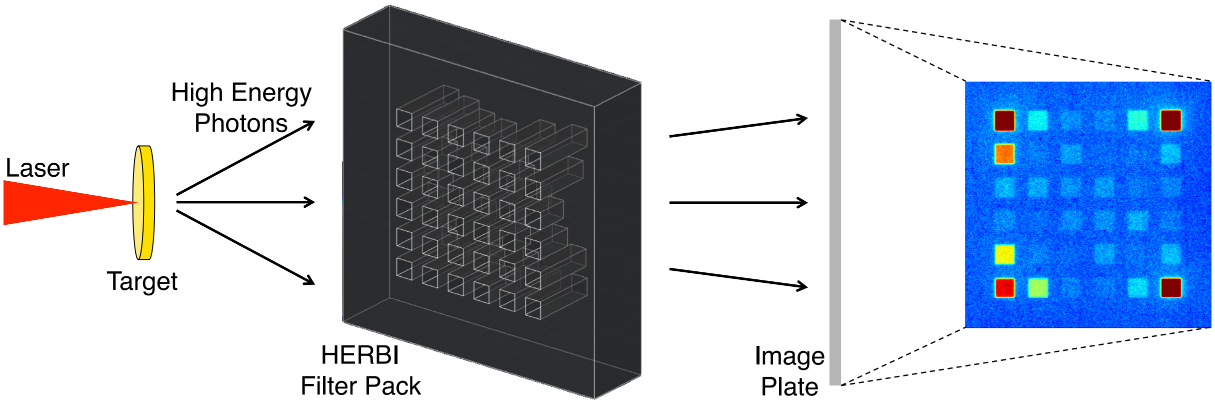

Figure 3.12: High energy photons are differentially filtered by high-Z masks of various thicknesses. An image plate detector measures the transmitted photons from which an estimation of the bremsstrahlung emission can be made.

ergies and fluxes experienced in positron production experiments. A multichannel step filter described here is optimized to measure the high energy tail of bremsstrahlung emitted from ultraintense laser-matter interactions including the 511 keV annihilation energy peak, albeit with coarse resolution. A step filter, or differential attenuation filter, uses increasing thickness steps and offers spectral sensitivity between the filter K-edge up to ∼2 MeV. Variations of the step filter or wedge filters have long been used in HED experiments but typically have a modest number of steps [84, 85] or are complicated by signal interference between discrete filters [86]. This design allows for independent determination of a local background noise for each channel, significantly reducing the systematic error in the reconstructed spectra.

The High Energy Bremsstrahlung Instrument (HERBI) is shown in Fig. 3.12 within an experimental diagram of its use. The filter channels are laser cut from 50×50 mm^2 tantalum sheets in a 6×6 orientation. The 26 unique channels are assembled using different masks on each of the filter layers where the total substrate thickness is 12.5 mm. The channels are offset from each other to allow for the accurate differentiation between signal that passes through the channel and background noise from fluoresces or high-angle scattering. Therefore, this design does not suffer from compounding uncertainties within the analysis, as is the case for “cannon”-like designs [87] or channel-adjacent designs [86]. Low-Z prefilters are installed at the front of the filter pack to reduce fluoresces within the Ta substrate, stopping electrons below ∼1 MeV and removing low-energy photons below 30 keV. Additional filters at the rear of the stack further mitigates fluorescence signal. The detector is a single Fuji BAS-MS image plate housed in a light-tight black thermoplastic enclosure which, after exposure, is read out using a calibrated image plate scanner.

The spectrometer channel thicknesses were chosen by accounting for the spectral range of interest and the expected range of photon emission profiles. For experiments with laser-solid interactions such as x-ray backlighters on high-Z materials or pair generation, the high energy portion of the expected photon emission can typically be described as a single-component exponential profile of the form $\exp(-E/kT)$ with a characteristic "temperature," kT. To design spectral coverage within the energy band of interest, we must consider that the spectrometer resolution is a function of both the channel thickness and emission profile. That is, for a given channel thickness, the average energy of the transmitted spectrum shifts to higher energies compared to the incident spectrum.

The energy-dependent spectral response profile, S, is the multiplicative function of the initial emission profile, all filters, and the detector response. For an example with a fixed Al and Cu prefilter, and assuming a single-temperature emission profile of temperature kT, the ith channel of the filter pack has an absorption profile of

$$S^i \times f(E,kT) = T_{Cu} \times T_{Al} \times T^i_{Ta} \times \Phi_{IP} \times f(E,kT), \tag{3.10}$$

where T is the transmissivity of the filter material, taken from the NIST XCOM database [52], and Φ_{IP} is the energy-dependent image plate sensitivity [77, 78]. Therefore, we can associate a mean photon energy to the ith channel, by calculating the center of mass of the spectrum,

$$\langle E^i(kT)\rangle = \frac{\int_0^\infty S^i(E',kT) \times f(E',kT) \times E'\, dE'}{\int_0^\infty S^i(E',kT) \times f(E',kT)\, dE'}. \tag{3.11}$$

As a continuous function of the channel thickness, $\langle E\rangle$ is shown in Fig. 3.13 for range of single-temperature emission profiles along with examples of individual absorption profiles, $S^i(E,kT)$. For a filter pack with prefilters of 2 mm Al and 0.5 mm Cu, a 0.5 mm Ta filter, and a $kT = 500$ keV emission profile, the mean energy of the absorption is $\langle E\rangle = 425$ KeV. At the extremes of the estimated photon profiles shown, $kT = 0.1$ and 2 MeV, the step filter has a spectral coverage between 100–500 keV and 0.5–1.5 MeV, respectively, while the more

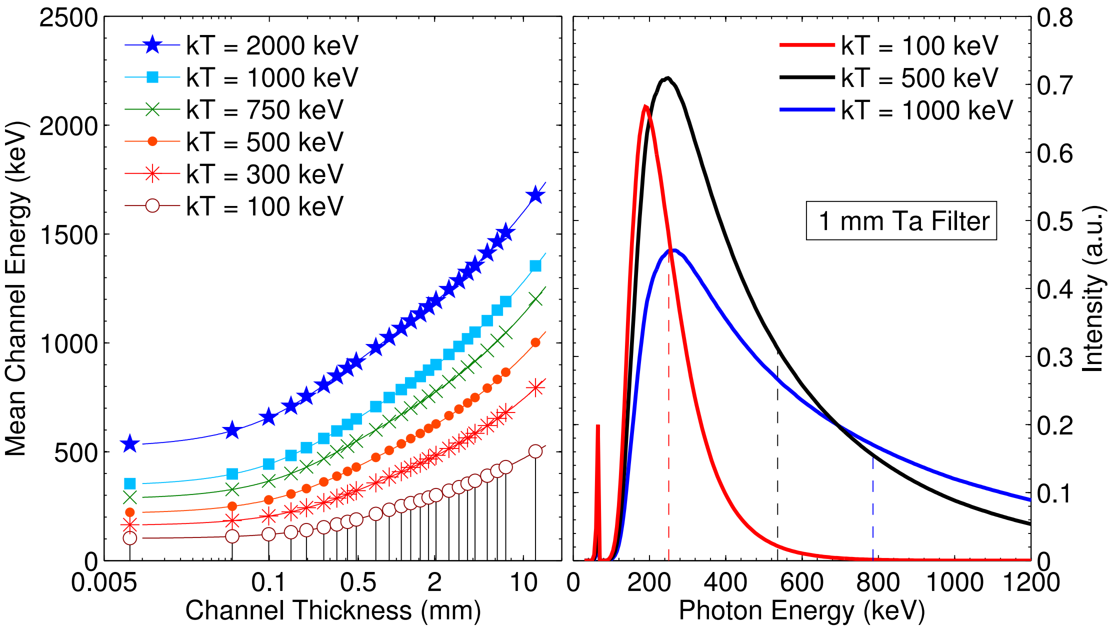

Figure 3.13: (Left) Mean photon energy detected by an MS-type image plate through Ta channels for various initial photon spectral temperatures. For each test emission profile, markers denote the mean energy of the existing diagnostic at the actual thicknesses.
(Right) Photon absorption profile on the detector for three emission profiles through the 1 mm Ta channel, where the dashed lines show the mean channel energy for the example emission. For all data shown here, a 2 mm Al and 0.5 mm Cu prefilters were assumed.

moderate temperatures have excellent coverage within the region of interest (100s of keV). The diminishing returns of increased channel thicknesses can be easily seen here, where the energy sensitivity of the step filter method becomes inefficient.

Step filters do not rely on absorption edges to discriminate photon energies; as such, the choice of material used for the substrate is arbitrary where energy resolution is determined only by the total absorption of the photon beam. The only consideration for material choice is the total thickness of the diagnostic where very large thicknesses should be avoided to minimize Compton scattering. For our spectrometer, Ta was chosen due to its machinability characteristics and high attenuation coefficient.

Using the analytic absorption model described above, an emission spectrum can be reconstructed by simultaneously solving for the fit parameters. This is a backwards fitting technique that relies on the input spectral shape to be chosen as a free parameter. That is, for a data set comprised of the absorbed dose on the image plate, D^i, with m distinct channels, the reconstructed emission profile is the one that simultaneously solves the system of linear equations,

$$\begin{pmatrix} S_1^1 & S_2^1 & ... & S_n^1 \\ S_1^2 & S_2^2 & ... & S_n^2 \\ \vdots & \vdots & \ddots & \vdots \\ S_1^m & S_2^m & ... & S_n^m \end{pmatrix} \begin{pmatrix} f(E_1) \\ f(E_2) \\ \vdots \\ f(E_n) \end{pmatrix} = \begin{pmatrix} D^1 \\ D^2 \\ \vdots \\ D^m \end{pmatrix}, \tag{3.12}$$

where f has been discretized into n energy bins. The response matrix, $\mathbf{S}$, has also been discretized, where S_j^i is the detector response for photons of energy E_j that have traveled though the ith spectrometer channel. This reconstruction method, using an analytically-derived spectral response matrix, is valid for cases without large contributions from scattering and fluoresces, such as signal originating from another channels or the image plate enclosure. To account for these secondary processes, Monte Carlo simulations are necessary.

Simulations were performed using the particle transport code Geant4 [55] with the included Standard database of electromagnetic interaction cross sections. Photons were initialized with logarithmically spaced energy bins from 5 keV to 10 MeV, where the bin width was set to a small fraction of the mean energy to blur any contributions from absorption edges or characteristic x-ray line emission. The photon divergence angle is set to overfill the filter substrate. Photons are subjected to photoelectric absorption, Compton scattering, Rayleigh scattering, and Bethe-Heitler pair production. Fluorescence photons can also be created in the filter material through radiative decay of excited electronic configurations. Free electrons, liberated by photons, lose energy though bremsstrahlung, Coulomb scattering, and ionization events.

Initial photons and secondary particles are propagated through a 3D model of the experiment, including all secondary filters, image plate enclosures, and room air at atmospheric pressure. The image plate is modeled using the recipe given in Maddox et al. [77], where the energy deposited within the active layer of the image plate is recorded. The average dose

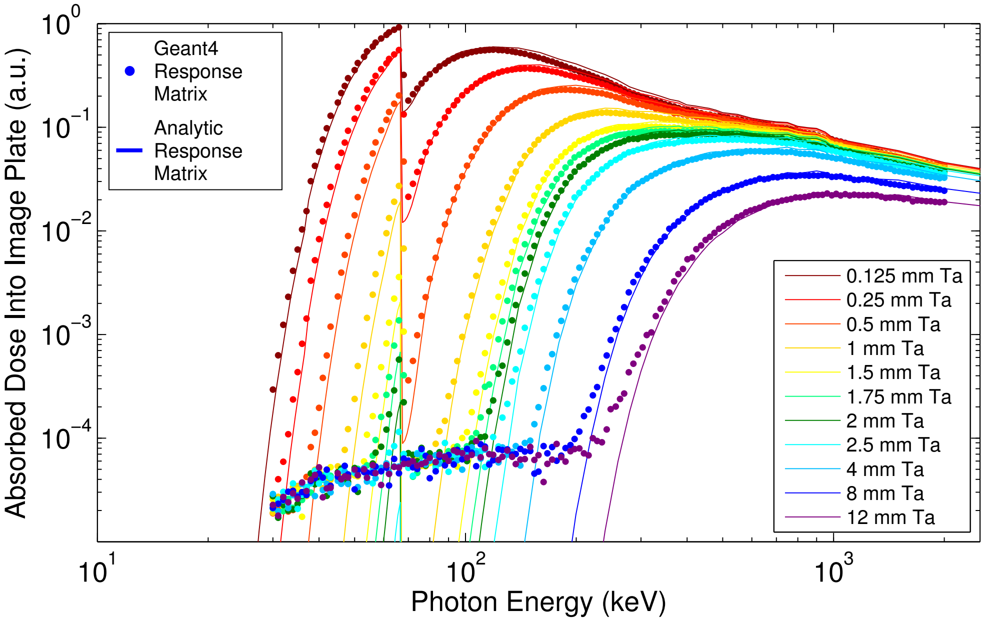

Figure 3.14: Comparison of the filter pack response matrix between the analytic calculation and Geant4 simulation. The largest deviations are seen at the low energy spectrum of all channels, where scattering and fluorescence play a significant roll in the total image plate dose for a given photon energy band.

recorded on the image plate, as a function of channel thickness and mean photon energy is shown in Fig. 3.14, along with the analogous calculation using analytic means, described above. Each discrete point represents an element of the response matrix, S^i_j. Contributions from scattering and fluorescence, originating from the inner walls of the channel and substrate, can be seen as the signal floor in the Monte Carlo results. The relative strength of this signal, however, is several orders of magnitude below the peak sensitivity of each channel. Therefore, in most cases using simple geometries, the analytic model can be used without the need for extensive modeling.

An example of the observed experimental data is shown in Fig. 3.15(a). The thinnest channels, recording the largest signal, are located at the corners of the filter grid, while the thicker channels are within the interior. The largest signals being at the four corners helps to determine the image rotation, magnification, and location of the interior channels since the remaining channels can be found through interpolation without the need for a spatial and magnification fiducial. The thin channel locations on the exterior also minimizes any signal

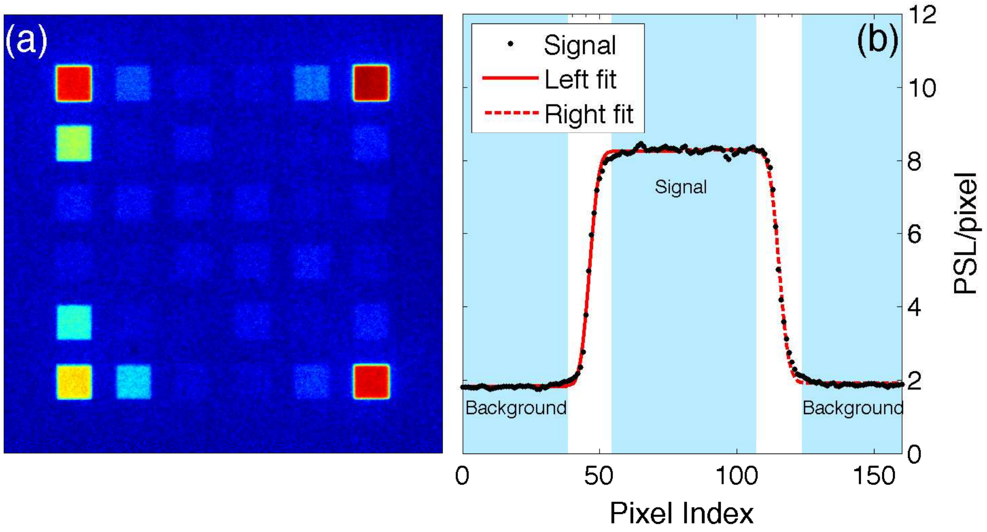

Figure 3.15: Example of (a) raw image plate signal for the step filter diagnostic and (b) the lineout of a single channel with determination of signal and background regions.

bleed into the thick-channel regions. Individual channel signals are measured by taking the mean value over the most uniform region of the square exposure. The bounds of this region are found through an edge detection technique, where a least squares fit is performed on each of the four sides of the square, fit to a cumulative distribution function for a Guassian, or error function, with the form

$$a \operatorname{erf}\left(\frac{x-\mu}{\sigma\sqrt{2}}\right)+b,$$

where a is a normalization constant, x is the pixel index, μ is location of boundary midpoint, σ is the standard deviation, or slope of the edge, and b is the background floor. An example of the line out and fit function is shown in Fig. 3.15(b) where the left and right shaded regions are taken to be the background level and the center shaded area is the region of uniform signal exposure. It was found that setting the omission boundaries to a width of $\mu \pm 3\sigma$ minimized the RMS variation of both signal and background regions. The process of determining the signal region is repeated for the four corner channels with the remaining interior and peripheral locations found by interpolation based on the position and size of the outer areas. The background signal of each channel is calculated by interpolating the surrounding 'aisles' between the channels. This compensates for any anisotropy in the background signal.

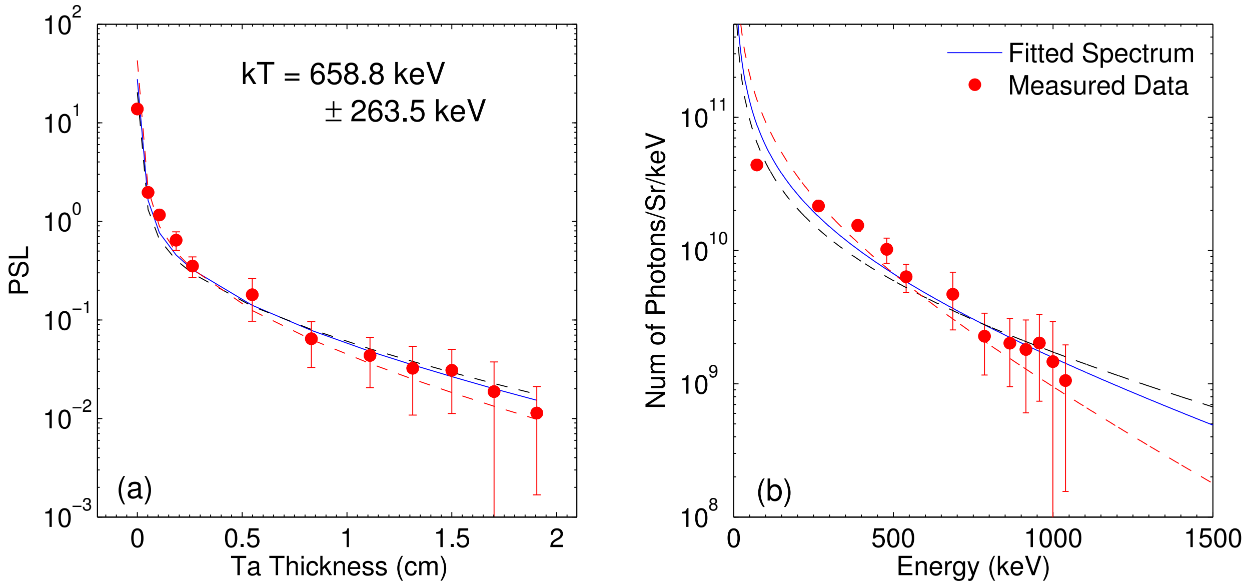

Figure 3.16: Bremsstrahlng photon reconstruction from HERBI data.
(a) Forward propagation of the best fit spectrum (solid) compared to the original data set (markers) where 20% confidence intervals nearly span the scatter in the data (dashed).
(b) Photon density spectrum where the data points have been overlaid using the relative deviation from the mean generated from the plot in (a).

The reconstructed photon density profile is generated by minimizing Eq. (3.12) using a least squares routine with a response matrix calculated either analytically or by Geant4, depending on the complexity of the geometry. Figure 3.16 shows the fitting results for the example data presented in Fig. 3.15(a). To check the validity of the process, the reconstructed photon spectrum is forward propagated using the transmissivity of the filters and compared to the original dataset, as shown in Figure 3.16(a). For this case, the best fit temperature was 650 keV, where a measure of the confidence intervals can be made by observing spectral estimate near this value. Here, the temperature is bounded by ±20% while maintaining the integrated energy of the best fit. Photon density spectrum, shown in Fig. 3.16(b), uses the relative deviation between data points and the best fit spectrum to map the data onto the vertical, physical unit scale. The energy of each channel is found by taking the mean energy of the transmitted spectrum through the channel filtration.

While the above description applies to photons specifically, the response matrix **S** can be

Filter Layer	Mask Number	Material	Thickness (mm)
0	1	None	0.0505
1	2	Au	0.006
2	3	Ag	0.036
3	4	Ta	0.008
4	5	Ta	0.0505
5	6	Ta	0.0990
6	7	Ta	0.1480
7	8	Ta	0.1955
8	9	Ta	0.2675
9	10	Ta	0.3395
10	11	Ta	0.4115
11	12	Ta	0.4825
12	13	Ta	0.6885
13	14	Ta	0.8865
14	15	Ta	1.0935
15	16	Ta	1.2975
16	17	Ta	1.5425
17	18	Ta	1.7935
18	19	Ta	2.0565
19	20	Ta	2.5865
20	21	Ta	3.1115
21	22	Ta	3.6355
22	23	Ta	4.1525
23	25	Ta	5.1905
24	27	Ta	6.2300
25	29	Ta	7.2505
Substrate		Ta	12.4255

Table 3.3: List of filter material and thicknesses for the HERBI stacks manufactured for experiments on the Orion Laser.

applied to electrons as the initial particle. In this case, numerical methods must be employed to account for the complex angle and energy dependence of bremsstrahlung. Electrons are initialized near the surface of a solid density target where the subsequent x-ray attenuation is performed as a single simulation. Iterations of this instrument have Ross pairs [88] installed for some of the filter channels, enabling an in situ calibration of the absolute photon flux.

For reference, a list of the channel filter parameters is given in Table 3.3 for a version of HERBI used at the Orion Laser Facility which uses the Ross pairs. A scale diagram of the instrument, noting the positioning of each channel, is shown in Fig. 3.17.

3.3 Pulsed Power Solenoid Coil

As noted in Chapter 2.1, positron yield predominantly scales as Z^4. For low-Z materials, a signal intensifier scheme is used to collimate divergent beams of positrons into a far field detector, which is the subject of the study presented in Chapter V. This is achieved by using an axial magnetic field acting as a convex lens.

The axial magnetic field was created using a pulsed power driven solenoid coil made from large rounds of copper. Both the coil and capacitor bank were designed for prior experimental campaigns [89] and modified for the work presented here. The coil is a Bitter-type electromagnet [90] where partial annulus rounds of conductor are butt welded together to form a continuous coil loop. The rings were laser cut from 0.5 mm copper with outer and inner diameters of 7.6 and 2.1 cm, respectively, and a 33° wedge cutout, as shown in Fig. 2 from Ref. 89. The large aspect ratio of the coil, and relatively thick plates prevent thermal distortion of the coil during high-current discharges. The final coil has 25 turns of copper with threaded connecting plates soldered and screwed onto either end. Two layers of 0.125 mm Kapton (polyimide) film are used between each copper layer for electrical insulation, with approximately 2 mm of overlap on the inner and outer diameters for a total bore thickness of 1.9 cm. The experimental geometry is such that the target is placed very close to the center of the coil and a large amount of debris and plasma blowoff is expected. As this could cause arcing between coil rounds, a 3D printed plastic inner bore protector was installed and is physically oriented by the Kapton spacers.

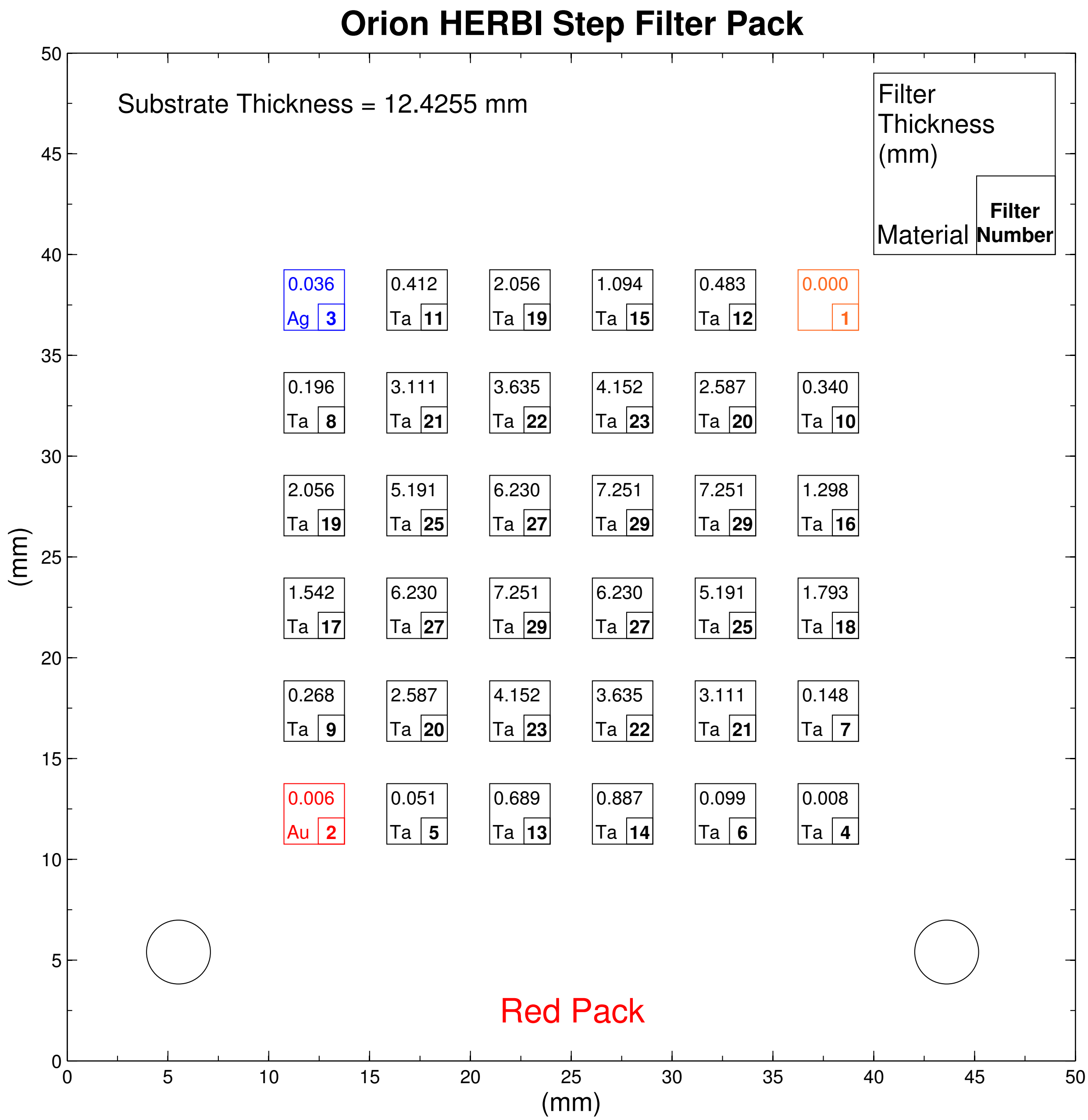
Orion HERBI Step Filter Pack
Substrate Thickness = 12.4255 mm
Filter Thickness (mm)
Material
Filter Number
0.036 Ag 3
0.412 Ta 11
2.056 Ta 19
1.094 Ta 15
0.483 Ta 12
0.000 1
0.196 Ta 8
3.111 Ta 21
3.635 Ta 22
4.152 Ta 23
2.587 Ta 20
0.340 Ta 10
2.056 Ta 19
5.191 Ta 25
6.230 Ta 27
7.251 Ta 29
7.251 Ta 29
1.298 Ta 16
1.542 Ta 17
6.230 Ta 27
7.251 Ta 29
6.230 Ta 27
5.191 Ta 25
1.793 Ta 18
0.268 Ta 9
2.587 Ta 20
4.152 Ta 23
3.635 Ta 22
3.111 Ta 21
0.148 Ta 7
0.006 Au 2
0.051 Ta 5
0.689 Ta 13
0.887 Ta 14
0.099 Ta 6
0.008 Ta 4
Red Pack
(mm)
(mm)
0
5
10
15
20
25
30
35
40
45
50

Figure 3.17: Diagram of HERBI filter locations and thicknesses. Circles on the bottom corners are orientation pinholes to align mask layers.

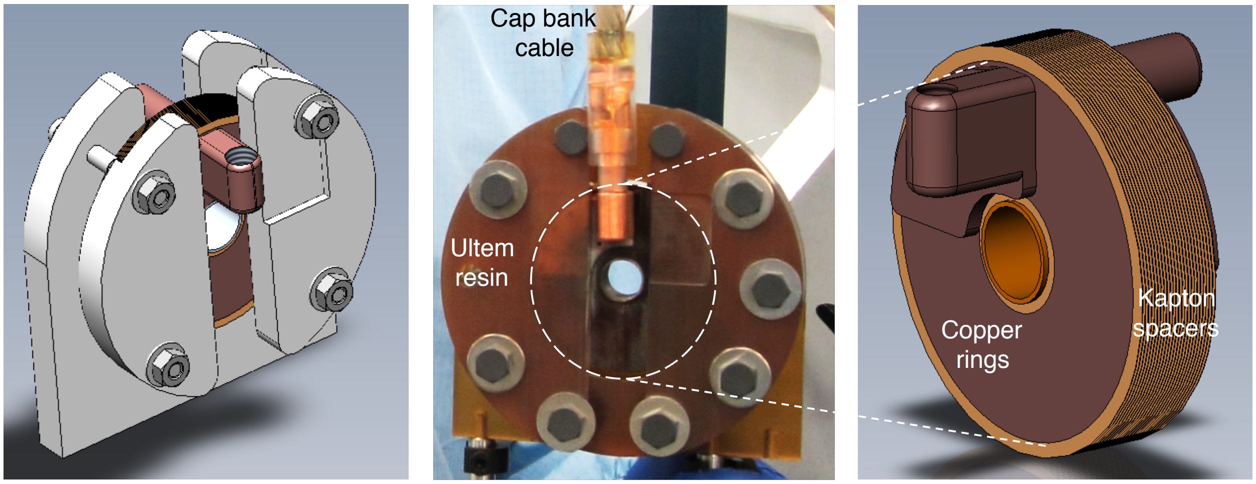

Figure 3.18: The constructed electromagnet is compression fit into a high tensile strength resin and clamped with nonconducting bolts. A CAD model of the coil (right) and assembled holder apparatus (left) are shown together with a photograph of the manufactured version just before it is installed in the Titan target chamber (center).

The coil was compression fit into an Ultem (polyimide) holder assembly made from four pieces: a horse-shoe backing plate with a beveled bore hole; a retaining ring spacer; and two half-moon front plates. The retaining ring orients the coil in the center of the holder and creates a surface to which even pressure can be applied to secure the front and back plates. Cutouts in the face plates allow for the close installation of a target and the electric leads arriving from above that deliver current from the capacitor bank. The holder assembly is fastened by insulating nylon-fiberglass bolts whose tensile strength roughly matches aluminum (∼300 MPa). Images and CAD models of the coil and holder are shown in Fig. 3.18. The largest advantage to a compression fit design is the omission of “potting,” or the process immersing the coil in epoxy for structural containment and electrical isolation.

Current is supplied by a high voltage pulsed power system comprised of three capacitors wired in parallel ($C_{\text{total}} = 144\ \mu\text{F}$), each with a 1.5 Ω resister in series to create a weakly damped circuit. An ignitron switching mechanism is triggered by a single TTL signal and reaches peak current in $\sim 60\ \mu\text{s}$, as measured by an internal Rowgowski coil. The capacitors

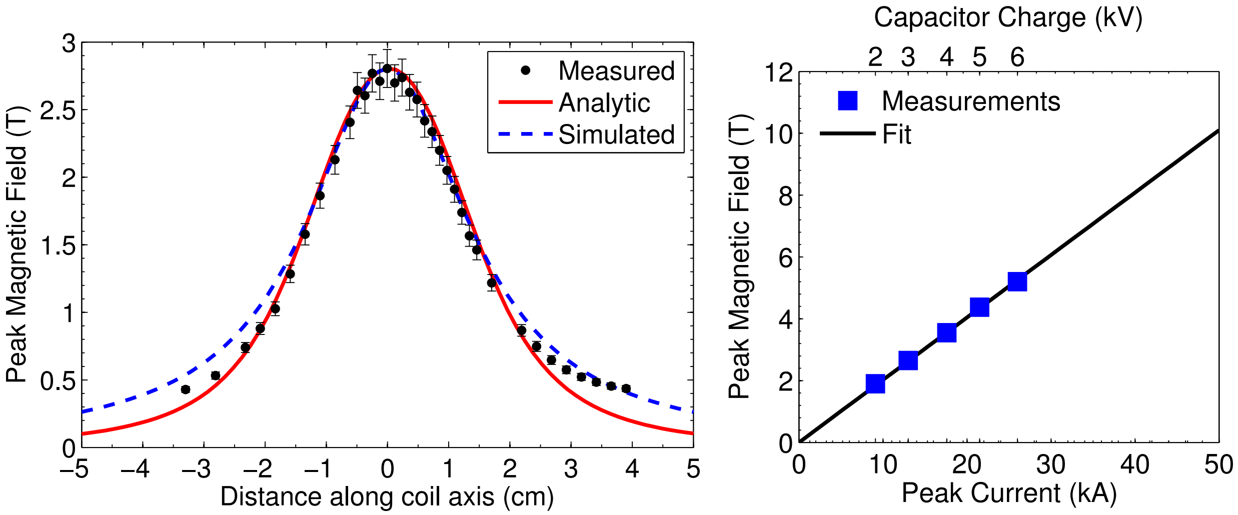

(a) (b)

Figure 3.19: (a) Measured axial magnetic field measurements along the bore of the electromagnet (dots) along with the analytical prediction of the spatial shape of the field (solid). A magnetostatic simulation (dashed) agrees best with the measured field. The analytic and modeled fields have been normalized to the peak of the measured values.
(b) Measurements of the peak magnetic field as a function of capacitor bank charge. A linear relation is shown between the peak current and magnetic field.

can be charged to 20 kV with 29 kJ of stored energy.

The magnetic field produced along the axis of a circular current loop can be expressed analytically by elliptic integrals [91] where

$$\begin{aligned} B_x(x,y,z) &= \frac{\delta x z}{a\alpha^2\beta\rho^2}\left[(a^2+r^2)E(k^2)-\alpha^2K(k^2)\right], \\ B_y(x,y,z) &= \frac{\delta y z}{a\alpha^2\beta\rho^2}\left[(a^2+r^2)E(k^2)-\alpha^2K(k^2)\right] = \frac{y}{x}B_x, \\ B_z(x,y,z) &= \frac{\delta}{2\alpha^2\beta}\left[(a^2-r^2)E(k^2)+\alpha^2K(k^2)\right], \end{aligned} \tag{3.13}$$

where, for the current coil, $a = 1.1$ cm is the radius of the loop, I is the current, $\delta = \mu_0 I/\pi$, $r^2 = x^2+y^2+z^2$, $\rho^2 = x^2+y^2$, $\alpha^2 = a^2+r^2-2a\rho$, $\beta^2 = a^2+r^2+2a\rho$, and $k^2 = 1-\alpha^2/\beta^2$. The elliptical integrals of the first and second kind are expressed as K and E respectively. A finite coil thickness, L, can then be constructed by stacking single coils and evaluating the above expression at the location of each loop.

A measurement of the axial magnetic field, $B_z(0, 0, z)$, along the coil axis was characterized using a single-turn pickup probe with a 1.975 mm diameter. Figure 3.19(a) shows a comparison between the measured and calculated peak magnetic field for capacitor discharges of 2 kV. Slight changes in the values of solenoid length and radius in the analytical calculations were made for better fit to the data at the wings, where $a_{\text{fit}} = 1.6$ cm and $L_{\text{fit}} = 2.1$ cm. The discrepancy between these can be accounted for by the finite thickness of the coils and insulating films. A 2D ($\hat{r}$-$\hat{z}$) finite element field simulation was performed to predict the steady state magnetic field produced by a current in the solenoid using the Ansoft Maxwell 3D software [92]. The result has a better agreement to the data than the modified analytic solution, particularly for the low-field wings.

The coil was tested for various discharge currents with the results shown in Figure 3.19(b). Extrapolating from the observed trend, the maximum achievable peak magnetic field for this power source is ~17.5 T. This field is well below the magnetic pressure limitation of oxygen-free copper, where for the alloy used, the tensile strength was 330 MPa corresponding to a maximum field of $B_{max} = \sqrt{2\mu_0 P_B} = 29$ T.

CHAPTER IV

Positron Generation from Laser Wakefield Electron Sources

This chapter investigates using laser-wakefield accelerated (LWFA) electrons to drive pair production in a secondary target. This platform has several clear advantages over the direct irradiation of a target with an ultaintense laser, namely that laser-wakefield systems are tabletop, are capable of a high repetition rate (up to 10 Hz), and can generate relatively high-charge electron bunches with energies of 100s of MeV up to several GeV. Since the electron acceleration mechanism is independent of the pair production target, the initial conditions of the generation process can be known with a high level of certainty as opposed to direct irradiation where the electron acceleration and pair production are integrated, occurring within the same target.

This work was motivated by a study by Sarri et al. [13] that reported a highly collimated beam of dense positrons using this experimental platform. Here, we discuss an attempt to reproduce these results, where it was found that a similar electron source did not result in a measured positron signal. Furthermore, Monte Carlo modeling indicated that a factor of 5–30 more beam charge was necessary to exceed the detection threshold and that an initially collimated electron source produces a divergent positron beam that was an order of magnitude larger than reported in Ref. 13 (100 mrad in the current study compared with 2.3 mrad in Sarri et al.). The results presented here are in stark contrast to those in Sarri et al., where it is believed that in the latter study, critical aspects of charged particle transport physics through thick, high-Z targets were not included, namely collisional scattering.

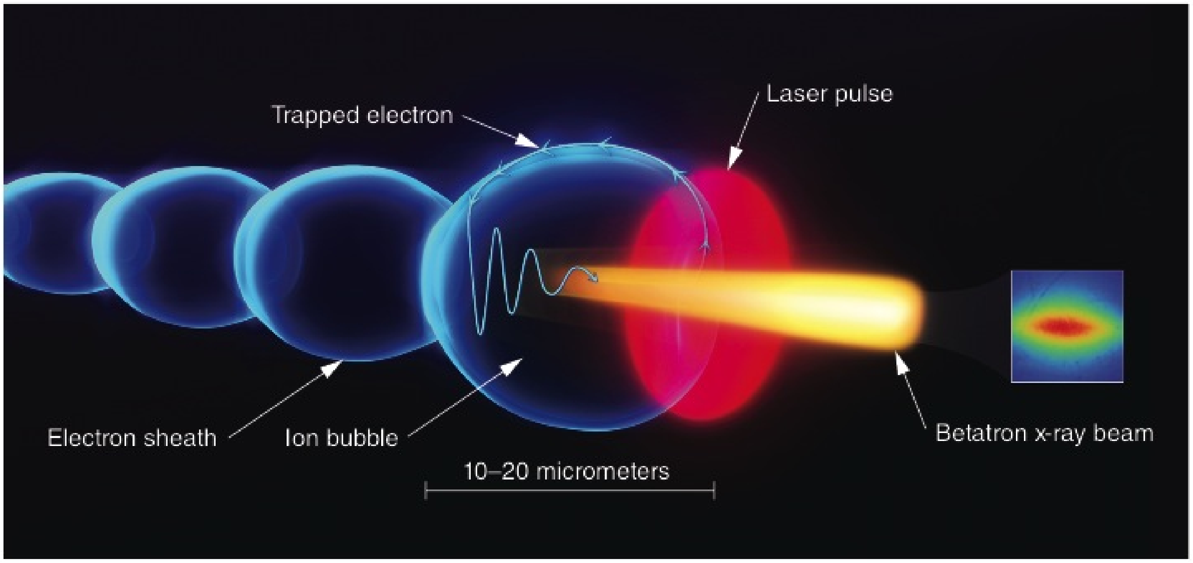

Figure 4.1: Cartoon of an ultrafast laser pulse propagating in an underdense medium with the formation of a plasma bubble in its wake. Figure courtesy of F. Albert.

The current work provides new understanding to the fundamental limitations of creating narrow-divergence, high-density positron beams from laser-wakefield platforms, which are critical for potential applications in laboratory astrophysics experiments. Portions of this chapter are in part a reprint of the material contained in the publication Williams et al. [15] where the dissertation author was the primary investigator and author of the paper.

4.1 Experimental Conditions of LWFA

As a laser pulse propagates through a low density gas, the radial ponderomotive force drives electrons in an oscillatory trajectory. The gas, typically helium with or without a dopant, is supplied by either a supersonic gas jets [93] or sub-atmospheric gas cell [94] in order to shape the spatial density profile. At the focus of an ultraintense laser, with $I > 10^{18}$ W/cm^2, the electrons are completely evacuated by the electric field forming an ion bubble in the wake of the pulse. The expelled electrons return to the laser axis where the strong Coulomb attraction of the static ions accelerate the trapped electrons at the back of the bubble structure. These accelerating gradients can reach magnitudes of a few MeV/μm,

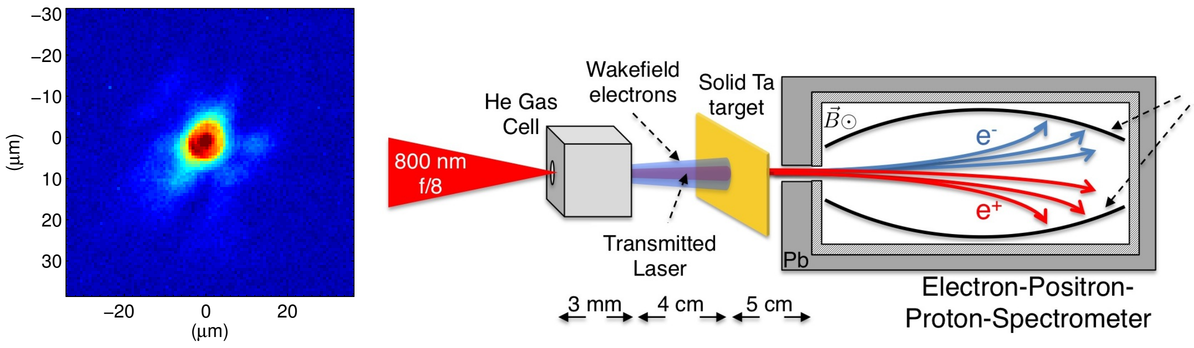

(a) (b)

Figure 4.2: Image of the Callisto focal spot (a) and experimental setup (b) at the Callisto Laser System. The 11 μm FWHM spot contains 50% of the laser energy in the beam.

efficiently producing electron beams with energies exceeding 1 GeV with charges of 10^8–10^{10} electrons per bunch [43, 46, 94–96]. The bubble-regime of LWFA, shown schematically in Fig. 4.1, is explored in more detail in Chapter 2.2.4.

A pair generation experiment using LWFA was performed in the Callisto target area at the Jupiter Laser Facility at Lawrence Livermore National Laboratory. The laser delivers an 800 nm, 60 fs pulse focused by an f/8 off-axis parabolic mirror. The focal spot shown in Fig. 4.2(a) was measured at low energy, in an equivalent plane using a CCD camera which had an effective pixel size of 0.7 μm, and measured 10 μm in the vertical direction and 12 μm in the horizontal. An 11 μm FWHM circular spot contained half of the laser energy which varied between 6.5–10 J. This is equivalent to a normalized laser amplitude between $7 < a_0 < 9$, intensities of 1.1–1.8 × 10^{20} W/cm^2, and powers of 100–170 TW. The focal position was placed 500 μm inside a 3 mm, helium-filled gas cell with a 0.5 mm and 1 mm pinhole at the entrance and exit, respectively (see Refs. 46 and 97 for details on the gas cell).

A range of gas cell backing pressures were explored in order to optimize both the mean electron energy and total beam charge, the product of which is nominally conserved [98]. The pure helium gas was puffed into the cell 50 ms before the arrival of the laser, allowing any turbulence and density inhomogenates to decay away and establishing a smooth entrance and exit density profile. A pressure of 550 Torr was found to produce the best compromise of high flux and high energy where a transverse interferogram measured the fully ionized

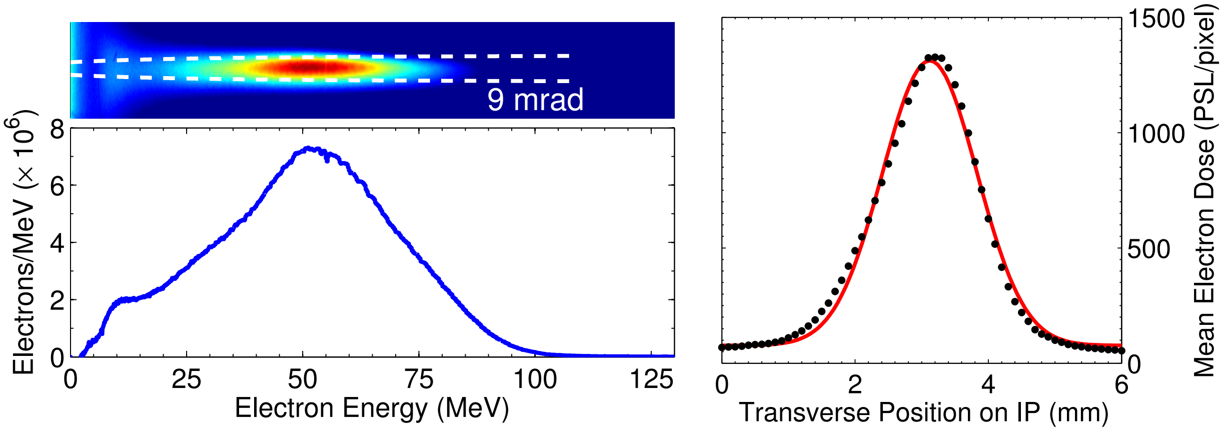

(a) (b)

Figure 4.3: (a) Raw electron image plate data (top) and analyzed data (bottom) from the Callisto laser with 6.5 J of energy on target. Image color and x-axis has been linearized where the FWHM divergence is outlined as a 9 mrad projection from the laser focal spot location.
(b) Transverse lineout of the electron spectrum taken at 50 MeV (5 cm within the EPPS slits) shows no hard-edge clipping with a FWHM of 1.7 mm.

electron density of the gas to be $n_{e^-} = 9 \times 10^{18}$ cm^{-3} where $n_e/n_c = 5.3 \times 10^{-3}$. For these conditions, the dephasing length is 1.5 mm and pump depletion length is 3.4 mm. The laser and density conditions place the acceleration mechanism into the 3D nonlinear regime or complete blowout regime of LWFA, for which we can expect to accelerate electrons up to ∼300 MeV [43, 45, 99].

The electrons were measured by the EPPS, which was positioned 9 cm behind the gas cell and equipped with a 1×2 mm^2 slit where the direction of dispersion was in the smaller dimension. A diagram of the experimental layout is shown in Fig. 4.2(b). Aluminized mylar, 1 μm in thickness, was wrapped around the Fuji BAS-SR image plate to protect against exposure from the transmitted laser light. The spectrometer was operated with and without the front 5 cm lead collimator housing in attempts to minimize background signal. A small spectrometer slit, with an angular acceptance angle of 22 mrad, was used since the positron spot size at the detector was expected to greatly overfill the aperture area. The EPPS was chosen as the particle spectrometer since the noise structures are very well understood and reduce the possibility of misinterpreting data.

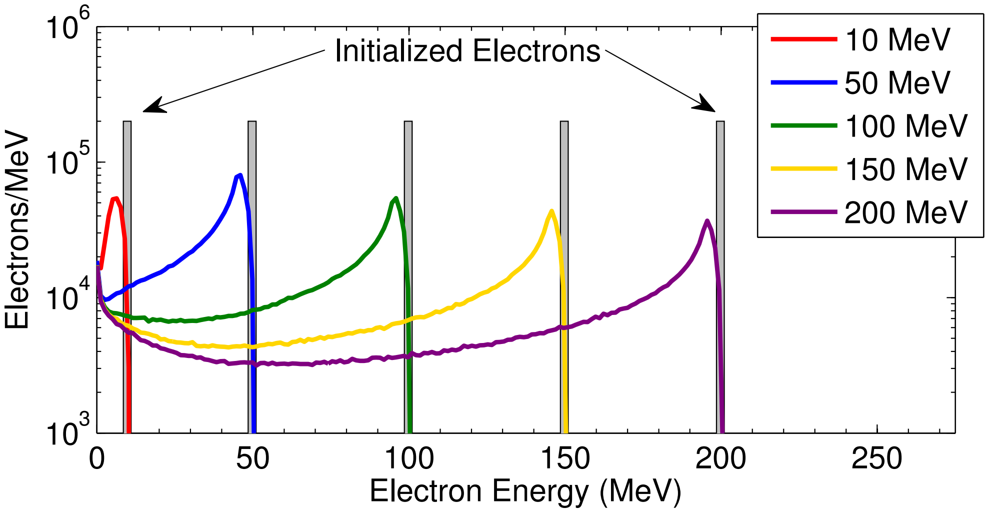

Figure 4.4: Transmitted electron spectrum from monoenergetic beam through 1.5 mm of Ta, as observed by a 22 mrad collection window in the forward direction. Initialized electrons are downshifted in energy after traversing a target and secondary electrons are generated at low energies.

Electron-to-positron converter targets made of 1.5 or 3.0 mm solid Ta ($Z = 73$), chosen for its large pair production cross section, were placed 4 cm away from the back of the gas cell. A total of 9 shots were performed with 1.5 mm Ta targets and 9 shots with 3.0 mm targets. Additional shots were conducted using targets with thicknesses from 0.25 mm to 4.2 mm; however, the largest number of shots were performed with 1.5 and 3.0 mm targets and we focus on these in the current study.

Since the blowout regime of LWFA is highly nonlinear, the electrons produced were not reproducible on a shot-to-shot basis and predominantly dependent on the laser energy and whether the laser correctly self focused without first filamenting. Electron spectra were qualitatively similar consisting of a narrow divergence and a central peaked feature at high energies. Here, we will focus on two electron spectra that represent the low and high limits of beam energy and beam charge for the campaign.

Electrons from a designated “low intensity” shot, which did not have a converter target in place, were produced with an on-target laser energy of 6.5 J and can be seen in Fig. 4.3. The beam had an average energy of 50 MeV and a total charge of 56 pC (3.5×10^8 electrons). The transverse profile of the beam has a Gaussian profile with a FWHM of 1.7 mm at a

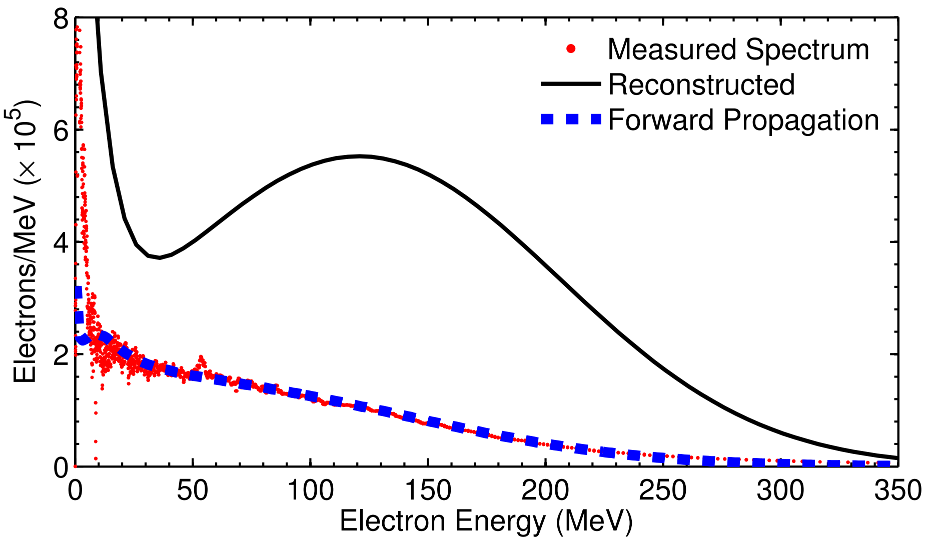

Figure 4.5: Electrons observed after first traveling through 1.5 mm Ta target (dots) for a Callisto shot with 10 J of laser energy. The results of Monte Carlo modeling to reconstruct the source electrons (solid) has a one-component exponential and Gaussian functional form. The reconstructed electrons are forward propagated to simulate the observed transmitted electrons (dashed).

distance of 5 cm inside the slit aperture, at the spatial point corresponding to the peak signal energy of 50 MeV. Projecting this back to the laser spot size, the divergence of the beam was 9 mrad and passed through the 2 mm slit without clipping, assuming an initial spot size equal to that of the laser.

At a higher laser energy of 10 J, referred to as the “high intensity” shot, electrons were observed extending out to energies above 300 MeV. However, the measured electron signal was only observed after first passing through a 1.5 mm Ta converter target where the signal overfilled the spectrometer aperture. Monte Carlo simulations were performed, using Geant4, to reconstruct the initial source electrons using a bootstrap solving method. Electrons were modeled as a collimated beam with narrow energy bands passing through a Ta target where the scattered primary and secondary electrons within the solid angle of our detector were collected for each energy band. A subset of these components are shown in Fig. 4.4 for various initial electron energies.

The spectral profile of the reconstruction, which is a free parameter of the backwards fitting procedure, was chosen to be a Gaussian plus an exponential where fit parameters

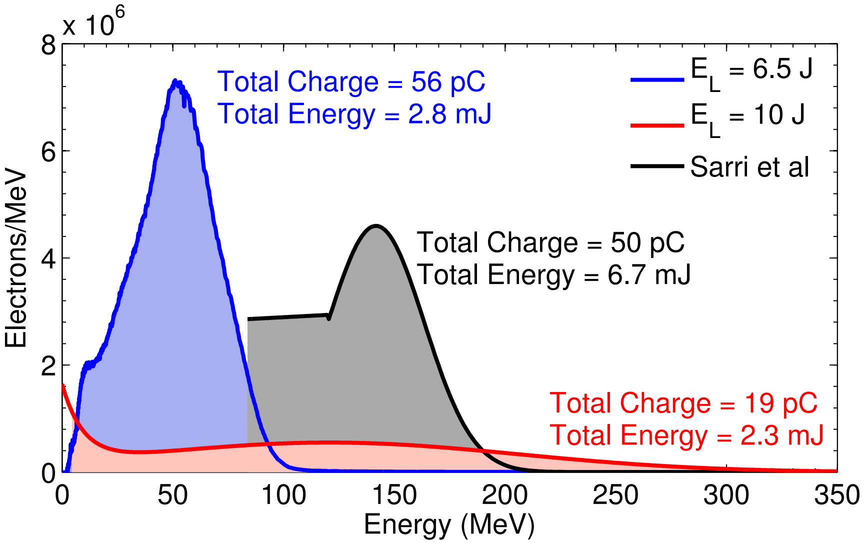

Figure 4.6: Comparison between the electron sources observed in the current study and the reported electrons from Sarri et al. [13]. Although the extremes of the two electron sources presented here span the total charge and mean energy from the Sarri et al. study, no positron generation was detected at the Callisto laser. Calculations of total charge and total energy are taken from the shaded areas of each curve.

of the distribution were solved for by inversion. This functional shape is representative of other observed electron spectra during this and previously reported blowout regime LWFA campaigns. The detected electrons from a 10 J laser shot is shown in Fig. 4.5, along with the reconstruction of the original source electron beam. As a check of the estimated initial source validity, the final reconstructed electrons were forward propagated through the target and is well matched to the observed spectrum. The reconstructed electrons have a mean energy of ∼120 MeV and total charge of 19 pC.

The reconstructed electrons represent the lower flux limit and are used as a bound on the highest energy electron source observed. Since the measured electrons overfilled the spectrometer slit, no experimental divergence measurement exists to inform the simulation, therefore, a zero-divergence initial electron source was chosen for this reconstruction. If, however, the electrons had an initial divergence, the transmitted electrons would be scattered into higher angles and experience a larger effective target thickness with greater attenuation. The total charge of such a reconstructed beam would necessarily be larger than that of the non-divergent case. It is noteworthily to mention again that the bootstrapping reconstruction method used here does not guarantee a unique solution since the choice of spectral shape is a free parameter and the spectral shape used was chosen due to the similarly shaped electron beams at lower energies.

As a verification of the beam shape and emittance characteristics, several shots measuring the LWFA electrons were performed with a dipole-style, two-screen spectrometer [100]. Shielding was placed 1 cm away from the beam axis to prevent direct line-of-sight from the image plates to the converter target and the electrons beams were found to be consistent within the range of energy, charge, and divergence when compared to data taken with the EPPS. Positrons were also not observed using this spectrometer.

The background noise signal in the EPPS, predominantly resulting from bremsstrahlung as well as fluorescence in the lead collimator, set a lower detection threshold limit of approximately 10^3–10^4 positrons/MeV, with a higher detection threshold at low energies. The detection threshold was empirically determined from the stochastic noise structure of the background signal and is shown in Fig. 4.7. Due to the Callisto laser repetition rate of one shot per 30 min, exposing image plates for consecutive shots to build statistics was impractical due to image plate fading times.

To better understand why a positron signal was not observed, analytic and Monte Carlo models were used to describe the properties and dynamics of pair production in the context of this experimental platform.

4.2 Analytic Modeling of LWFA-Produced Positrons

A simple analytic model, first described in Chapter 2.1, is used here to estimate the pair yield via the Bethe-Heitler and Trident pair production processes. An analytic expression is ideally suited for this experimental platform since the electron source function is known to a high degree of certainty. Using normalized units, the positron yield per incident electron

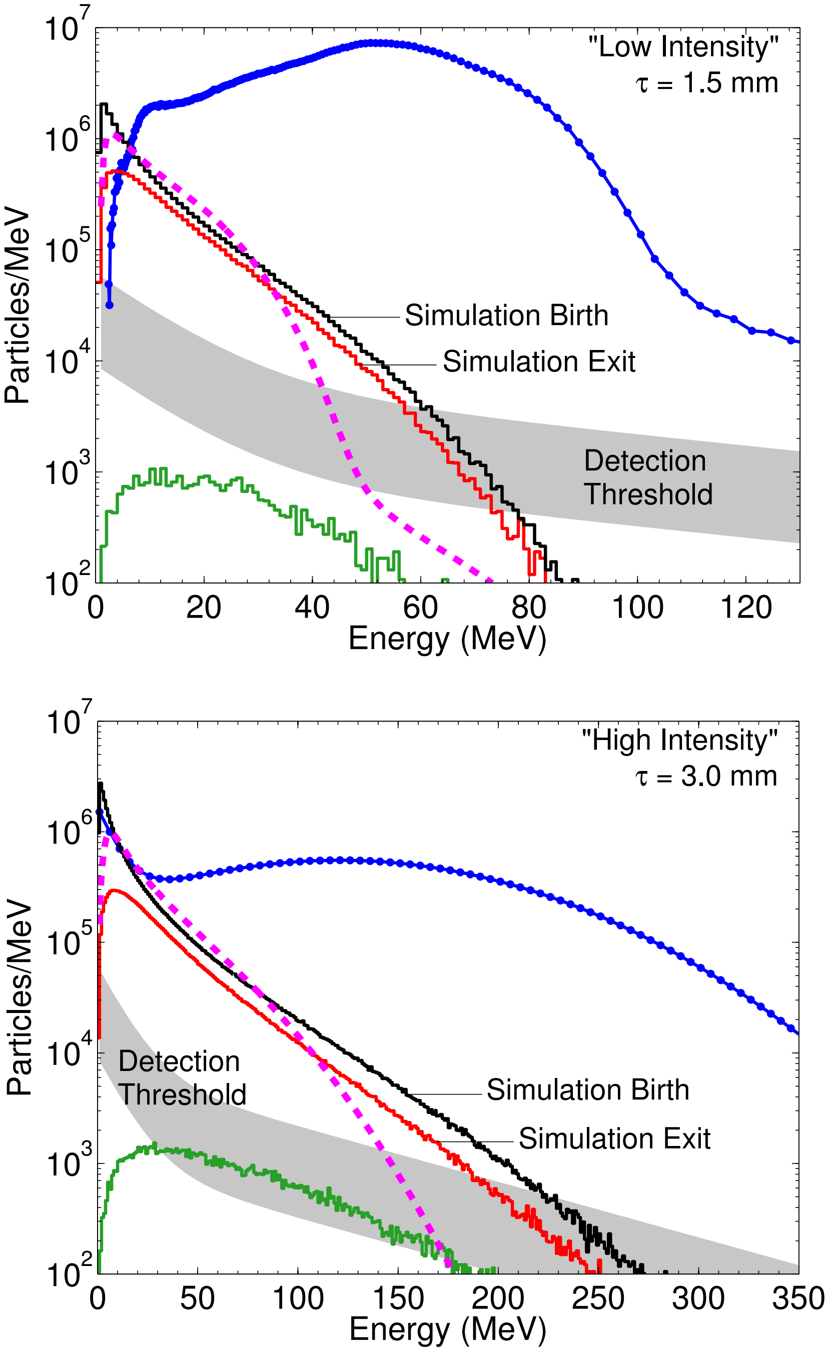

Figure 4.7: Analytic model and Monte Carlo simulation of positron production in a tantalum target using (top) a 1.5 mm target and the "low intensity" electron source from Fig. 4.3 and (bottom) a 3.0 mm target and the "high intensity" electron source from Fig. 4.5. The analytic birth positron spectrum (dashed) shows discrepancies with the birth Monte Carlo spectrum at low and high energies due to the assumed equipartitioning of the photon kinetic energy. Positrons exiting the rear of the target show attenuation at low energy and only a small fraction of the positrons are within the solid angle of the detector (lower solid). This signal level is within the measured noise threshold (shaded) of the EPPS.

can be estimated by

$$I_{e^+} = I_{e^+}^{T} + I_{e^+}^{BH} \propto \int_0^{\mathcal{T}} dt \int_{mc^2}^{E_0} I_k(E,k,t)\ \sigma_{e^+/e^-}(k) dk + \int_0^{s(E_0)} \int_0^{E_0} \sigma_T(E(\tau))\ d\tau\ dE, \tag{4.1}$$

where $\mathcal{T}$ is the target thickness in units of radiation lengths, I_k is the fractional bremsstrahlung energy distribution, σ_{e^+/e^-} is the photon pair production cross section, and E_0 is the electron initial energy. The Trident cross section σ_T is a function of electron kinetic energy which, in tern, is dependent on the CSDA range, s, of the electron within the target. The first generation bremsstrahlung spectrum (photons produced by incident electrons) can be approximated by

$$I_k = \frac{\rho}{X_0 k} \int_0^{\mathcal{T}} e^{-\mu t} dt \int_k^{E_0} \frac{4}{3} \frac{k/E}{\ln\left[(1/(1-k/E)\right]} dE. \tag{4.2}$$

With this, Eq. (4.1) can be evaluated to estimate the total number of positrons born inside a target for an arbitrary electron source. For example, using the "low intensity" electron spectrum, shown in Fig. 4.3, the expected birth yield is 1.5×10^7 and 4.8×10^7 for 1.5 and 3.0 mm Ta, respectively, where the Trident production accounted for roughly 2% of the yield (see column 3 of Table 4.1). The analytic approximation for the Bethe-Heitler process does not include pair generation from second-generation bremsstrahlung photons, which are generally only a significant contribution at very thick targets ($\mathcal{T} > 2$).

An estimate for the energy distribution of born positrons can be inferred from the energy-dependent bremsstrahlung expression, Eq. (4.2). The number of positron-electron pairs generated per incident bremsstrahlung photon is given by $n_i \sigma_{e^+/e^-} \tau$, where n_i is the nucleon number density, and τ is the target thickness in physical units. If each positron-electron pair is assumed to be created with equal kinetic energy, i.e., $E_{e^+/e^-} = (E_k - 2mc^2)/2$, an estimation of the Bethe-Heitler birth spectrum as a function of initial electron energy can be made. The results of our analytic model using the "high" and "low" intensity sources for both 1.5 and 3.0 mm Ta targets are shown in Fig. 4.7.

The energy dependence of the resulting positrons is a reasonable approximation for the central portion of the distribution and provides a first order estimate of the pair production by LWFA electron sources. At the low and high energy regions, however, the probabilistic spread in birth positron energies would be more prominent than depicted here. An assumption was made that energy is conserved between the photon and pairs yet, this is not the case, since pair production is a three-body interaction where the nuclear field is perturbed. As well, the energy-dependence of collisional stopping in the target for the Bethe-Heitler pairs was not taken into consideration. To fully incorporate these important components of pair production and account for the many physics processes involved, a Monte Carlo simulation is necessary.

4.3 Monte Carlo Modeling of LWFA-Produced Positrons

Monte Carlo modeling was performed using the particle transport code, Geant4, with all standard physics, including electron and positron ionization, bremsstrahlung, multiple Coulomb scattering, particle induced x-ray emission, photoelectric absorption, Compton scattering, and pair production via the Bethe-Heitler method. Four experimental conditions were modeled with the target thickness either 1.5 or 3.0 mm and the electron source from the 6.5 J, "low intensity" shot or the 10 J, "high intensity" shot. A total of 3×10^7 electrons were simulated in each case and scaled to the total charge for the respective source distribution. Electrons were initially collimated and uniformly distributed over a 40 μm diameter spot, representing the experimental electron spot size given a 9 mrad divergence at the location of the target. A collimated electron source represents the lower bound on total pair yield, divergence, and source size and the upper bound on pair density at the rear surface. The positron-electron pair momentum, position, and relative time was recorded for each pair birth throughout the interior of the target. Extraction planes at the exterior of the target, as well as at increasing distances from the back surface, recorded emitted positrons.

As shown in Fig. 4.7 for each of the electron sources, the numerical pair production matches well with the analytic model, except for deviations at high energies, where the anisotropic energy partitioning, not present in the model, would be most evident. The numerical simulations show that a large fraction of the lowest energy (<10 MeV) birth positrons do not make it outside the target, where the stopping power is sufficient to cause

Electron Source	"Low Intensity," $E_L = 6.5$ J		"High Intensity," $E_L = 10$ J	
τ (mm)	1.5	3.0	1.5	3.0
$N^{\text{Birth}}_{\text{Analytic}}$ ($\times 10^7$)	1.57	4.99	0.83	2.62
$N^{\text{Birth}}_{\text{MC}}$ ($\times 10^7$)	1.49	5.02	0.83	2.93
$N^{\text{Exit}}_{\text{MC}}$ ($\times 10^7$)	0.77	1.01	0.60	1.81
$N^{\text{1SR}}_{\text{MC}}$ ($\times 10^7$)	0.54	0.98	0.43	1.04
$N^{\text{Det.}}_{\text{MC}}$ ($\times 10^5$)	0.31	0.38	0.97	1.30
$\overline{\theta}^{\text{Birth}}_{\text{MC}}$ (mrad)	304	337	196	219
$\overline{\theta}^{\text{Exit}}_{\text{MC}}$ (mrad)	427	291	325	236
$\overline{\theta}^{\text{H.E.}}_{\text{MC}}$ (mrad)	127	153	55	75
$\overline{E}^{\text{Exit}}_{\text{MC}}$ (MeV)	12.1	14.7	25.9	30.8
d_{MC} (μm)	330	1490	90	310
n_{MC} ($\times 10^{12}/\text{cm}^3$)	5.2	1.1	40.0	10.0

Table 4.1: Summary of analytic model and numerical simulations for the "high" and "low" intensity electron sources and target thicknesses, τ, of 1.5 and 3.0 mm. The positron yields, N, for the birth analytic model (column 3) and Monte Carlo simulation (columns 4–7) for the total number of positrons born in the target, escaped the rear surface of target, exited in a 1 radian cone normal to the back surface, and exited within the solid angle subtended by the detector in the experiment, respectively. The positron mean divergences, $\overline{\theta}$, (columns 8–10) are given for all birth positrons, exiting positrons from the rear surface, and high energy (H.E.) positrons, respectively, where for the "low intensity" electron source $E_{\text{H.E.}} > 50$ MeV and for the "high intensity" electron source $E_{\text{H.E.}} > 100$ MeV. Column 11 is the mean energy and column 12 is the FWHM diameter spot size of the positrons exiting the rear of the target. Column 13 is the maximum density of the exiting positrons, assuming a 10 fs electron bunch duration.

the particle to come to rest within the bulk. The breakthrough energy for an electron or positron is 3.7 MeV and 15.0 MeV for 1.5 and 3.0 mm of Ta, respectively [49]. This also underscores the diminishing returns of increasing target thickness for a fixed electron source where the positrons may be trapped in the target.

While total birth pair production increases significantly between the 1.5 mm and 3.0 mm targets for the low intensity case, the number of exiting positrons and forward going positrons (those within a 1 steradian cone) see only marginal increases (see columns 4–6 in Table 4.1). For the "high intensity" electron source, the effect of stopping power is less evident as the positrons do not stop within the 3.0 mm thickness. Furthermore, these simulations show that only a very small percentage (0.5%–2%) of the total positron yield reaches the detector entrance slit and that the anticipated dose is an order of magnitude below the measured detection threshold.

4.3.1 Minimum Achievable Divergences

Despite the simulation initializing with collimated electrons, produced pairs are born with large perpendicular momentum, where bremsstrahlung and pair production each contribute to the angular divergence by $\theta = 1/\gamma$[25]. Electrons and exiting positrons also have an increased divergence due to small angle Coulomb scattering which, for Ta targets thicker than $\sim$100 μm, is the dominant divergence effect over pair production [30]. The additional increase in divergence from effects such as Compton scattering of a bremsstrahlung photon, θ^{Comp}, as well as any experimental initial electron divergence, θ_{e^-}, would add in quadrature to these effects assuming each to be approximated as a Gaussian angular distribution profile, with the total divergence given by

$$\begin{aligned}\theta^{\text{Exit}}_{e^+} = \Bigg[& (\theta_{e^-})^2 + \left(\theta^{\text{Coul}}_{e^-}(E_0,\tau')\right)^2 + \left(\frac{1}{\gamma_{\text{Brems}}}\right)^2 + \\ & \left(\theta^{\text{Comp}}_{\text{Brems}}\right)^2 + \left(\frac{1}{\gamma_{e^+e^-}}\right)^2 + \left(\theta^{\text{Coul}}_{e^+}(E',\tau'')\right)^2\Bigg]^{1/2},\end{aligned} \tag{4.3}$$

where θ^{Coul} is the divergence contribution from Coulomb scattering for an initial electron of energy E_0 traversing a distance τ' and birth positron of energy E' over a distance τ'' where

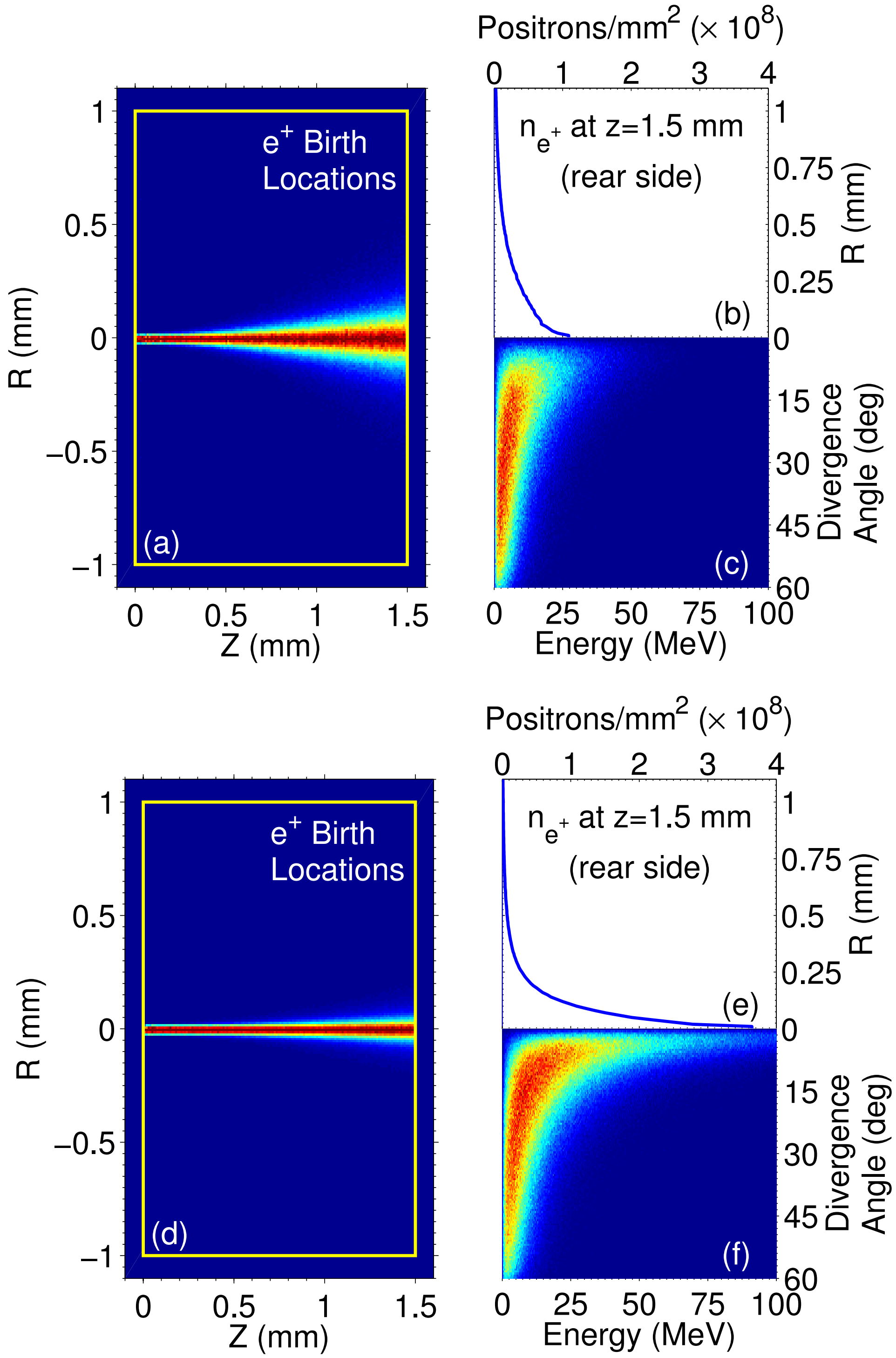

Figure 4.8: Positron trajectories within a 1.5 mm target for the 6.5 J, "low intensity" electron source (top) and the 10 J, "high intensity" electron source (bottom). Radially averaged physical location of positron birth (a, d) within the target (outlined). Time integrated positron emission spot size (b, e) on the rear side of the target. Emitted positron spectra as a function of divergence angle (c, f) from the back surface normal direction. Color scales have been normalized for all plots.

$\tau' + \tau'' < \tau$. This divergence derivation also assumes there are no cascade events, where the electron from the born pair is involved in a second pair production event. In these instances, the divergence increases as a multiple of the cascade.

For each electron source, the emergent positrons have a large spot size on the rear of the targets with an average divergence of 13°–25° (see column 12 and 9 of Table 4.1, respectively) and visualized in Fig. 4.8. These divergences are comparable to the 22°–50° divergence range that was measured from positrons emitted by direct laser-target experiments [7, 16], suggesting that inelastic scattering inside the target dominates the exiting pair directionality and that small initial source divergences are negligible for this experimental platform. For the thick, 3 mm target cases of the "low intensity" electron source, the average birth divergence is larger than the average exiting divergence, which is due to low energy positrons scattering into very high angles, stopping and annihilating inside the target, as seen by the increase in average energy of the emitted positrons for thicker targets. Positrons with the highest energies (chosen to be greater than 50 MeV for the "low intensity," 6.5 J electron source and 100 MeV for the "high intensity," 10 J electron source) are much more directional and show less, but still significant, amounts of scattering than the average positron (see $\overline{\theta}_{\mathrm{MC}}^{\mathrm{H.E.}}$ in Table 4.1).

To investigate the physical processes occurring at different energies, we consider the smallest positron divergence scenario, the "high intensity," 1.5 mm Ta target. Shown in Fig. 4.9, exiting positron divergences are plotted against the distance a positron travels in order to exit the target, τ''. While the divergences span large values for a given birth location, the trend is clearly shown; as the positron travels a longer distance in the target, it picks up an increased perpendicular momentum. For the lowest energy positrons, these divergences average 10s of degrees whereas the highest energy bins have a mean of 2°–4°. The divergence for the highest energy positrons are consistent with previous work performed at very high energies for positron sources at linear accelerators [101]. Positrons born very near the rear surface have divergences between 1.2° and 2.8° (20–50 mrad) for the high and low energy ranges, respectively. Since our simulations begin with collimated electrons, these minimum divergences are the convolved result of the contributions from bremsstrahlung and pair production, Compton scattering, and Coulomb scattering of electrons.

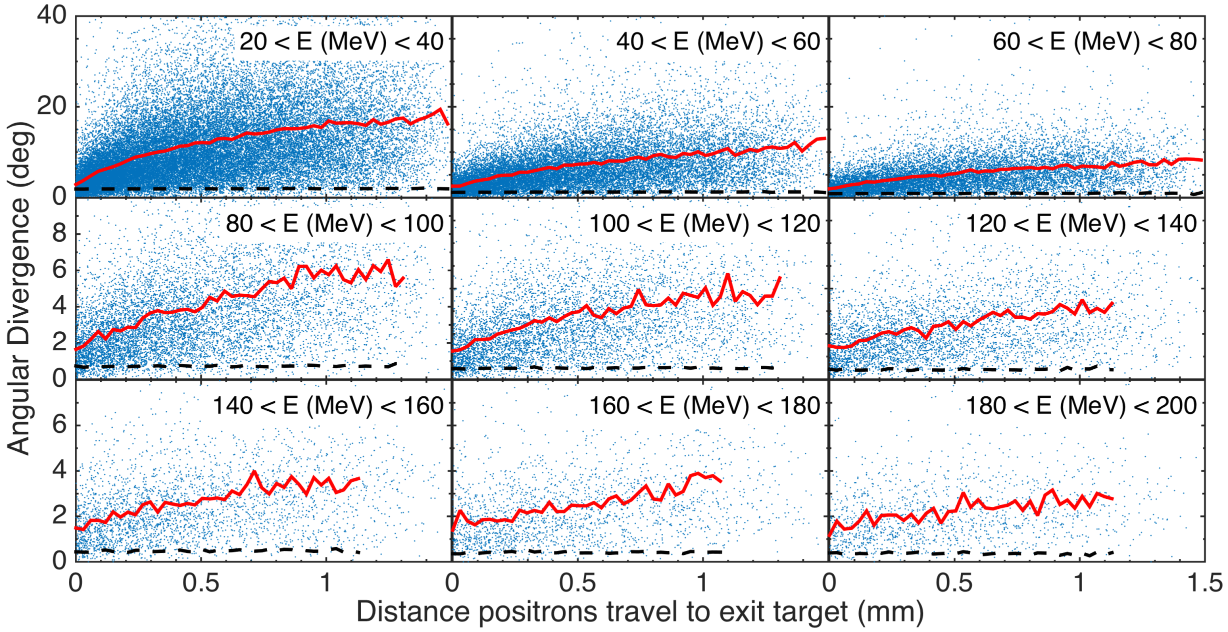

Figure 4.9: Monte Carlo simulation of the energy-resolved divergences of emitted positrons (dots) as a function of the distance between the rear surface of the target and the positron birth location from a 1.5 mm target using the “high intensity” electron source. The average divergences (solid) are shown for each energy condition. Simulations were then repeated where Coulomb scattering was omitted from the physics model (dashed).

The effects of the dominant scattering process is observed by repeating the simulations without the inclusion of positron or electron multiple Coulomb scattering physics. Shown in the dashed plot of Fig. 4.9, the positrons without Coulomb scattering have a nearly constant divergence angle for any given range of energies. This is expected since Compton scattering does not significantly contribute to divergence at these energies and the factor of $1/\gamma$ is relatively constant for each particle within the energy bin. Table 4.2 presents analytic and numerical results suggesting that the majority of the transverse momentum come directly from the two-part Bethe-Heitler process (Lorentz factor scaling) for the simulation omitting Coulomb scattering. The difference between these cases is likely due to the assumption of treating the bremsstrahlung and pair production as Gaussian angular distributions and the contributions of Compton scattering.

Particle Energy	(MeV)	30	70	110	150	190
$\left(\theta_k^2 + \theta_{e^+/e^-}^2\right)^{\frac{1}{2}} \simeq \sqrt{2}/\gamma$	(mrad)	23.7	10.2	6.5	4.8	3.8
$\overline{\theta}_{\mathrm{MC}}$ without Coulomb scattering	(mrad)	33.6	15.8	10.8	8.4	6.7

Table 4.2: Analytic approximation of the Bethe-Heitler (bremsstrahlung and pair production) divergence compared against Monte Carlo simulations without small angle Coulomb scattering included, averaged over centered a 20 MeV window, for a 1.5 mm Ta target.

4.3.2 Maximum Achievable Densities

The large number of scatters in the target also preferentially increases the temporal profile of the low energy positron beam. In simulations, all electrons are initialized at the same reference time; therefore, any spread in the positron arrival time at the back of the target measures the straggle time within. Positrons produced from the 1.5 mm Ta, "high intensity" case show a target-induced temporal spread between 4–56 fs for the highest and lowest energy ranges, respectively (see Fig. 4.10), while very low energy positrons (< 20 MeV) are emitted with a bunch duration of greater than 500 fs and, in the case of the 3 mm target, durations up to 1 ps. Simulations have shown that the highest energy LWFA electrons come from the first plasma bubble and have a duration of the half-width of the plasma frequency ($\sim$10 fs) [43]. Positron densities at the rear surface of the target are estimated by convolving the electron pulse width into the simulation time where the maximum densities were found to be on the order of 10^{12}–10^{13} cm^{-3} (see Table 4.1). As with the divergence angles, Monte Carlo simulations were repeated without Coulomb scattering included in the physics model. This revealed positron pulse spreads between 0.5 and 2.5 fs, consistent with semi-analytical models for the quantum cascades in high-Z targets [14]. The simulation analysis presented here provides strong evidence for the absence of positron data in our experiment and highlights the discrepancy between the previously mentioned studies [13]. Due to the highly divergent exiting positrons, a large increase in the source electron charge is necessary to exceed the spectrometer detection threshold.

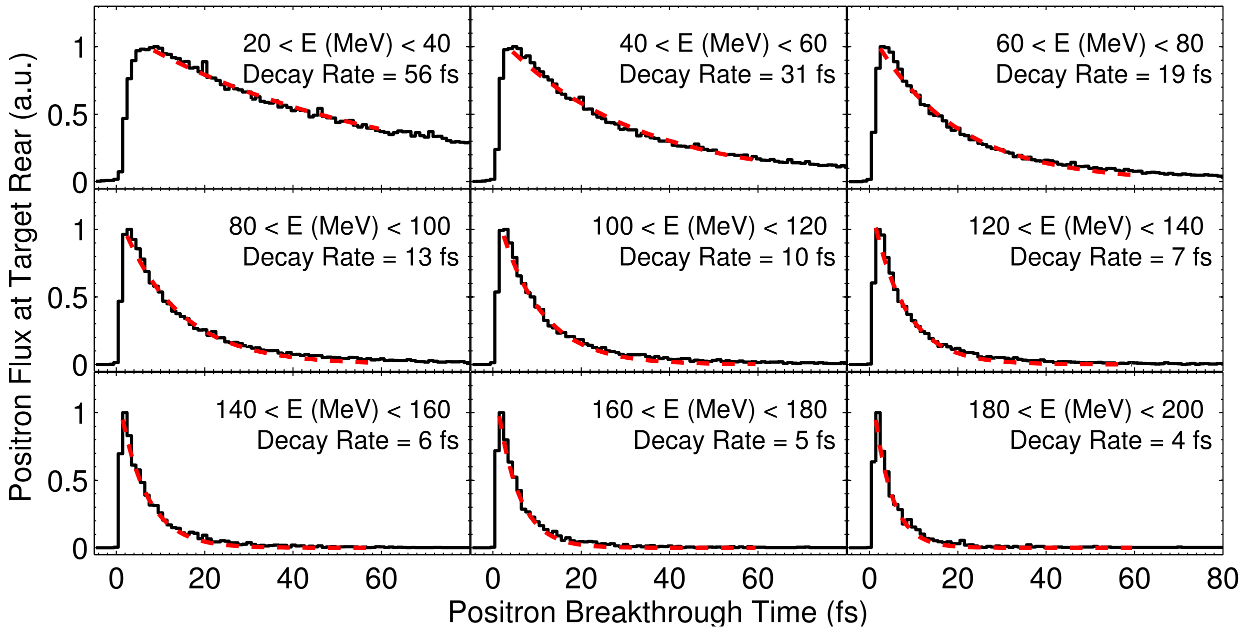

Figure 4.10: Temporal straggling of positrons arriving at the back surface of the target as a function of exiting kinetic energy (solid), given all particles are initialized together. The majority of the positrons are emitted within the first few fs while others straggle within the target delaying their arrival. The positron flux decay rate, reaching a $1/e$ magnitude, is fit to each spectral window (dashed). Modeled target was 1.5 mm Ta.

4.4 Discussion and Recommendations for Future Experiments

Experiments using LWFA electrons to produce positrons in a heavy metal target were performed. A measurable positron signal was not observed for a range of electron sources, target thicknesses, and shielding configurations. Numerical simulations show that, despite producing 10^7 pairs, the large divergence angle of the emitted positrons reduced signal levels below the detection threshold of the diagnostic. In order to observe positrons from a single-shot wakefield electron source, the "low-intensity" source would need a total charge of roughly 1.7 nC (a 30× increase) and the "high-intensity" source requires a factor of 5× increase to 100 pC. Increasing the mean energy of the positrons will improve the divergence characteristics; however, due to cascade pair production, the resulting positron beam will have the majority of its charge at low energies and subject to Coulomb scattering as discussed in this study.

Although no positron signal was observed, this experimental platform does show great potential for small laboratory scale experiments assuming the large positron flux can be controlled and limited to a small volume. Recent experiments [16], and the study presented in the following chapter, have demonstrated efficient collimation of positrons and electrons using an external axial magnetic field acting as a focusing lens that increased signal levels of a narrow energy feature by up to a factor of 40, where the collimation devices allow the pairs to maintain a mm-scale transverse profile. Coupling such a device to this experimental scheme would increase the number of positrons arriving at the detector to well above the noise floor, facilitating many of the recently proposed pair plasma experiments [10, 63, 102].

CHAPTER V

Target Material Dependence of Positron Generation from Direct Laser-Matter Interactions

This chapter seeks to provide guidance on the expected positron yield for different target materials and thicknesses using ultraintense lasers. Significant progress has been made to parameterize pair production, from the target geometry [7], laser energy [10, 63], positron emittance [8], and characterizing the photon emission and annihilation radiation [17]. A systematic study of the material dependence on positron production, however, has never been performed in the context of high intensity laser-matter interactions.

The primary obstacle to measuring positron production from various materials is the Z^4 dependence of the Bethe-Heitler process. As the atomic number of the material is reduced, the positron signal quickly drops below the instrumentation noise. Prior to this work, the lowest reported element used in direct irradiation pair production investigations has been tantalum at $Z = 73$. To be able to measure positrons from low-yield targets, a pulsed magnetic lens was used to collimate relativistic positrons, increasing the signal observed at a far field detector by more than a factor of 20. With this signal amplification, it is now possible to measure positron emission from mid-Z elements as low as Cu ($Z = 29$). From these measurements and Monte Carlo simulations, a simple power law relation was found for the target material scaling of positron production. The effective positron yield (those emitted in the forward direction) was determined to be proportional to only Z^2, yet this is still consistent with the Bethe-Heitler mechanism due to attenuation from Coulomb collisions, which act to stop or scatter positrons into high angles. An extrapolation from the

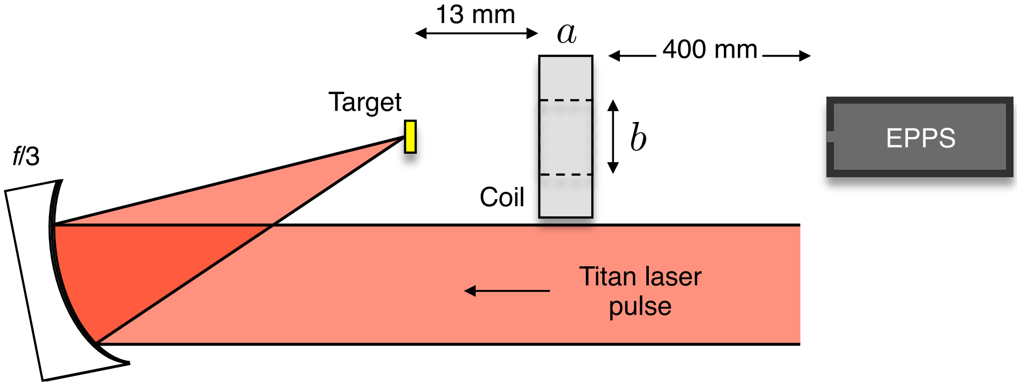

Figure 5.1: Diagram of the experimental setup. The Titan laser is incident on the target at an angle of 16° and the focusing coil axis was parallel with the target surface and in line with the EPPS. The coil had a thickness $a = 19$ mm and a bore diameter of $b = 21$ mm.

simulations provides a predictive model for arbitrary target materials and laser intensities.

5.1 Experimental Design

An experiment to measure the positron yield as a function of elemental material was performed at the Titan laser at LLNL [4]. Shown as a schematic in Fig. 5.1, a 10 ps laser pulse with wavelength $\lambda = 1054$ nm was focused by an $f/3$ off-axis parabola into a focal spot with a FWHM of 12 μm, containing 50% of the laser energy. The on-shot energy, averaging 270 J, was reproducible to within 7%, and corresponded to a peak intensity of 2.4×10^{19} W/cm^2. Targets were made of 6 materials (listed in Table 5.1) with various mm-scale thicknesses and all had a diameter of 6.3 mm. The temporal profile of the laser included a nanosecond-long pedestal originating from the intrinsic amplified spontaneous emission and had integrated energies between 35–40 mJ for the entirety of the campaign. This prepulse ionizes and ablates the front surface creating a large underdense plasma, with which the main pulse interacts, increasing the laser absorption into relativistic electrons.

Prior to employing a collimating magnetic field, several reference shots were performed under constant laser conditions to characterize the electron and positron source using 792 μm thick tantalum targets. Spectra from these shots for each species are shown in Fig. 5.2. The

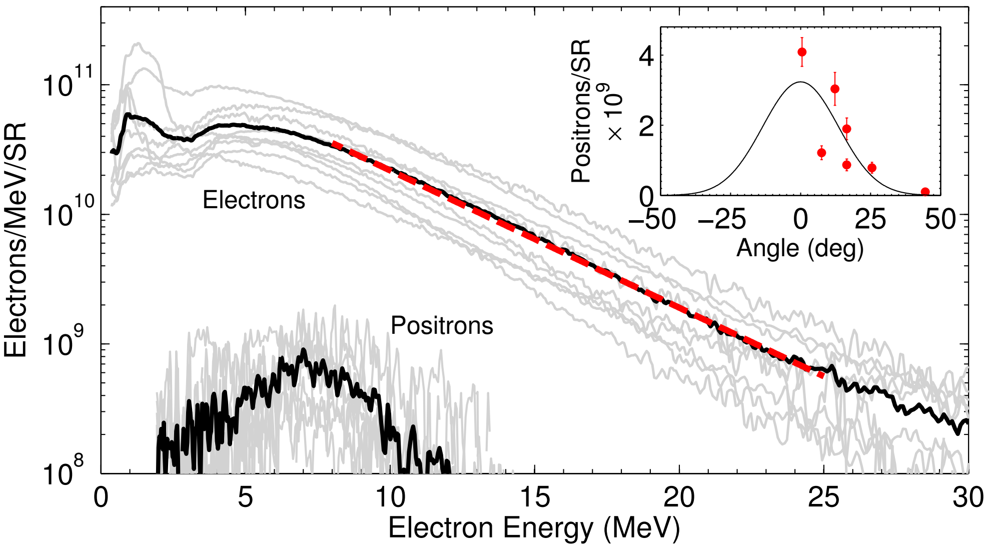

Figure 5.2: Reference electron (upper) and positron (lower) spectra from shots without externally applied magnetic field. The mean spectrum for each particle species is shown in black with individual reference shots in grey. A Maxwellian exponential fit to each of the electron spectra had an average temperature of 4.1 MeV (dashed). Angular dependence of positron yield is shown in the inset (dots) with Gaussian fit (solid). The target for all presented data was 792 μm Ta.

EPPS charged particle spectrometer was oriented perpendicular to the target rear surface at a distance of 43 cm and had a 1×1 mm^2 aperture slit installed before the magnets and used BAS-SR image plates. The high-energy portion (7–25 MeV) of the measured electron spectra had a Maxwellian-like exponential temperature of 4.1 ± 0.5 MeV, which is characteristic of stochastic acceleration mechanisms within the underdense plasma near the front surface [39]. The emitted electrons and positrons had a total integrated spectrum of $4.1(\pm 2.0) \times 10^{11}$ and

Material	Z	A (g/mol)	ρ (g/cm^3)	Target Thickness, d (mm)		
Cu	29	63.546	8.93	1.02		
Mo	42	95.940	10.22	1.15		
Sn	50	118.690	7.29	2.36		
Ta	73	180.948	16.65	0.792	0.518	0.279
W	74	183.850	19.25	0.538	0.265	
Au	79	196.966	19.28	1.00	0.254	

Table 5.1: List of targets and their parameters used in the current study. Positron yields for targets with atomic numbers or thicknesses below those listed were not observed.

$3.2(\pm 1.6) \times 10^9$ particles per steradian, respectively. The positron divergence, measured by changing the angle of the detector with respect to the target, had a FWHM of 30°, seen as an inset in Fig. 5.2. Reference positron spectra had a modest signal to noise ratio of $\sim$10. All reference shots for targets with Z less than Ta did not record positron signals above the EPPS noise threshold of 10^8 electrons/MeV/Sr.

For this study, it is assumed that the mean positron energy does not change with target material. The magnitude of the sheath potential is most directly controlled by the surface area of the target and number of free electrons created. The later of which is dependent on the electron density profile of the front surface. With a moderate prepulse of 35 mJ, the plasma scale length on the front side is expected to blowoff into subcritical densities over tens of microns. The electron conversion efficiency and characteristic spectral shape of the fast electrons reachs an upper limit as the scale length increases, saturating at $\sim$15–30 μm and consistent with the observed temperature [39].

To increase the signal observed at the detector, and measure the positron yield for these materials, a Bitter-type [90] coil magnet was used to collimate the exiting positron and electron jets. The design of this magnet closely follows previously constructed, two-coil solenoids used in magnetized plasma jet experiments [89, 103]. The details of the electromagnet and resulting axial magnetic field profile have been described in Chapter 3.3. A magnetic lens is a chromatic particle focusing optic used in many transport devices such as electron microscopes, accelerators, and medical proton therapy. A lens analogy can be made between magnetic and refractive optics where focal and objective distances are related by the lens power. Here, the strength of the lens is dependent on the magnitude and shape of the magnetic field and the energy of the particle. Predictive capabilities of the focusing geometry are critical to the accurate interpretation of positron yield measurements using such a lens. A diagram of the coil within the experimental setup is shown in Fig. 5.3.

5.2 Calculating Particle Trajectories in a Focusing Magnetic Field

Particle trajectories within an axial magnetic field can be estimated using an analogy to refractive optics [104, 105]. A cylindrically symmetric geometry reduces the necessary field

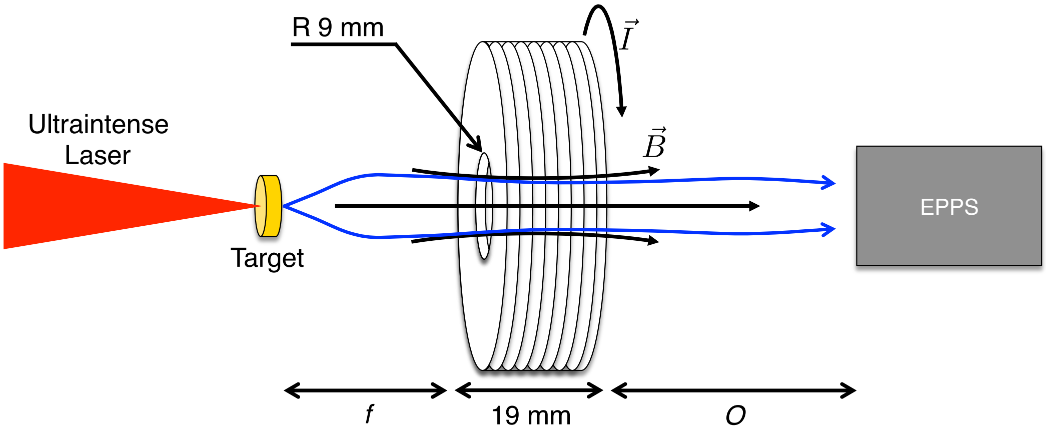

Figure 5.3: Diagram of experimental setup using a single-coil electromagnet as a focusing lens. The target is placed at the focal distance f away from the coil and the charged particle spectrometer at the object distance O.

measurements to only the axial field to calculate paraxial rays since B_r is given by Gauss's law,

$$\begin{aligned} \nabla \cdot \mathbf{B} = 0 &= \pi r^2 B_z(z) - \left[\pi r^2 B_z(z+dz) + 2\pi r B_r dz\right] \\ 0 &= 2\pi r B_r dz - \pi r^2 \frac{\partial B_z}{\partial z} dz. \end{aligned} \tag{5.1}$$

Here, the Taylor expansion of $B_z(z+dz)$ was used resulting in $B_r = -(r/2)\,\partial B_z/\partial z$. The equations of motion are given by expanding the Lorentz force to

$$\begin{aligned} F_\theta &= q\left(v_z B_r + v_r B z\right) \\ F_r &= q\ v_\theta B_z \\ F_z &= -q\ v_\theta B_r. \end{aligned} \tag{5.2}$$

Since the magnetic force does no work, $|v|$ must be conserved. A particle, with charge q, traveling along the coil axis is unaffected by the magnetic field where $\mathbf{v} \times \mathbf{B} = 0$ always. For close-to-axial trajectories, $v_z \gg v_r, v_\theta$, a positron (or electron) approaching the magnetic coil center experiences a tangential force, F_θ, from the dominant field contribution $v_z B_r$ where B_r is negative. The particle begins a spiral trajectory, where v_θ is negative (counterclockwise rotation) for positrons and positive (clockwise rotation) for electrons. The increased tangential velocity pulls the particle towards the axis by making F_r more negative (in both cases), acting like a convex lens. After passing through the coil center, the field lines begin to diverge such that B_r is positive and F_θ is negative, converting the motion of the gyroradius back to axial velocity. This shows that the focusing effect is identical for positrons and electrons since the signs cancel between q and v_θ, apart from spiraling in opposite directions. It is apparent from this that the region of the magnetic field responsible for the focusing is located in the fringe, where B_z is rapidly changing.

A simple analytic model can be used to give an intuitive picture of the particle trajectories, where Eq. (5.2) is expanded out following Reimer [104], with $\mathbf{v} = (\dot{r}, r\dot{\theta}, \dot{z})$, assuming $B_\theta = 0$ and that the trajectories of interest have small deviations from the axis (r is small and v_z is constant), the radial force on an electron is given by

$$m\ddot{r} = -eB_z r \frac{e}{2m} B_z + mr \left(\frac{e}{2m} B_z \right)^2 = -\frac{e^2}{4m} r B_z^2, \tag{5.3}$$

or

$$\frac{d^2 r}{dz^2} = \frac{e}{8 m_0 U^*} r B_z^2(r) \qquad \text{and} \qquad U^* = \frac{E}{e}\left(1 + \frac{E}{2E_0}\right), \tag{5.4}$$

where E is the total kinetic energy and $E_0 = m_0 c^2 = 511$ keV. Assuming the axial magnetic field can be expressed as a Lorentzian function, $B_z = B_0/[1+(z/\xi)^2]$, where 2ξ is the FWHM, the radial trajectory of a particle can be reduced to

$$\frac{d^2 y}{dx^2} = y'' = -\frac{k^2}{(1+x^2)^2} y, \tag{5.5}$$

where the dimensionless parameter substitutions are $y = r/\xi$, $x = r/\xi$, and a lens strength parameter

$$k^2 = eB_0^2 \xi^2 / 8 m_0 U^*. \tag{5.6}$$

The numerical solution to Eq. (5.5) is shown in Fig. 5.4 for various lens parameters, where the particle origin is set to the experimental placement of the target, and $\xi = 30$ mm, which was derived from a fit to the measured field. This model shows that for a lens strength of $k = 0.61$, a positron (or electron) will be collimated at the exit of the field. Using the mean

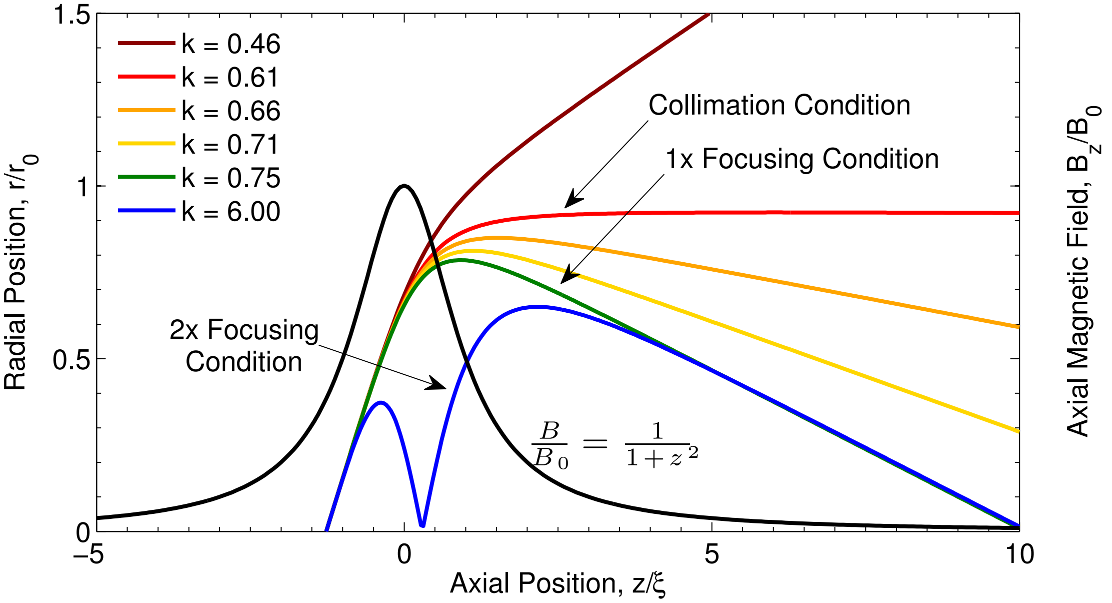

Figure 5.4: Trajectories of electrons or positrons passing through an axial magnetic field with initial divergences of 30°. As the magnetic lens parameter k increases, the electrons collimate ($k = 0.61$) as they exit the field and eventually are focused to a point along the axis ($k = 0.75$). At much higher strengths ($k = 6.0$), it is possible for the electron to pass through focus creating multiple image points.

value of the reference positrons from Fig. 5.2 of 7 MeV, this lens strength corresponds to a magnetic field magnitude of $B_0 = 2.1$ T. The focusing condition, where the particle arrives back on axis after 300 mm, occurs at a strength of $k = 0.75$, equal to $B_0 = 2.5$ T for an $E_0 = 7$ MeV. If the field strength is fixed at 2.5 T, an electron or positron can execute a double focusing trajectory if the particle energy is ∼0.5 MeV, as shown in the $k = 6.0$ case. Since the source size, divergence, and spectral properties vary significantly, a numerical ray tracing simulation was build for this application.

A ray tracing model was built that includes the full 3D description of the magnetic field constructed using the elliptical integral method described in Chapter 3.3. A fourth order Runge-Kutta numerical solver was employed to propagate particles through the field where a range of initial conditions could be explored. Figure 5.5 shows the measured field against the axial component of the calculated full field. Trajectories from particles with either 7.0 or 7.5 MeV of total energy and initial divergences of 1–10° show a scenario with the beam focused and partially focused. The sensitivity of the chromatic focusing effects can be seen

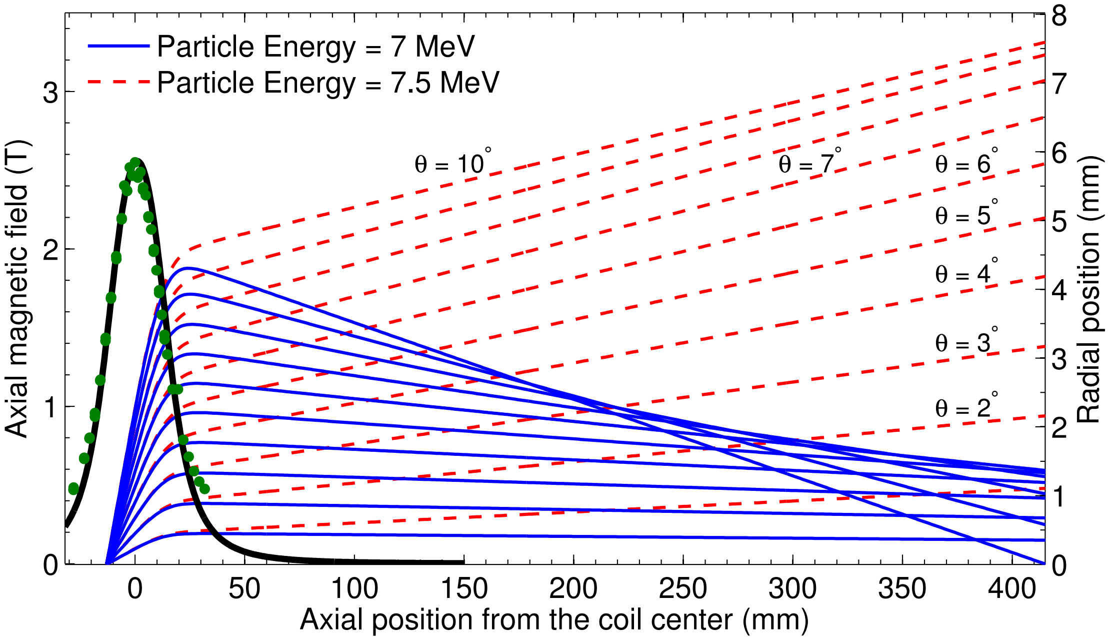

Figure 5.5: The measured axial magnetic field (dots) is reconstructed using elliptical integral calculations of the magnetic field (solid black) and used to propagate 7.0 and 7.5 MeV particles (solid and dashed, respectively). For a particular energy, the field will focus a wide range of initial divergences, here shown as rays between 1 and 10 degrees. The sensitivity of the focal condition is demonstrated where the higher energy particles focus into a finite spot.

here with the small energy difference. The spread of initial divergences demonstrates the finite focal spot, analogous to Gaussian optics, where the change in v_r/v_z dramatically affects the image distance of the lens.

The entire phase space of the focusing condition as a function of particle kinetic energy and initial divergence is plotted in Fig. 5.6. Particles were uniformly initialized with energies up to 10 MeV and initial divergences up to 10° from a point source along the coil axis. A total of 5×10^5 particles propagated through the 3D magnetic field and the beam was considered “collimated” or “focused” if the radial position, measured at a distance of 43 cm after the target, was less than 1 mm. These dimensions equate to the distance from the target and nominal acceptance geometry of the EPPS.

Low energy particles are shown here to meet the collimation condition, which was also qualitatively seen in the analytic model, at energies of ∼1.9 MeV, 1 MeV, and continuously lower. These models reveals that very low energy particles are more susceptible to the field

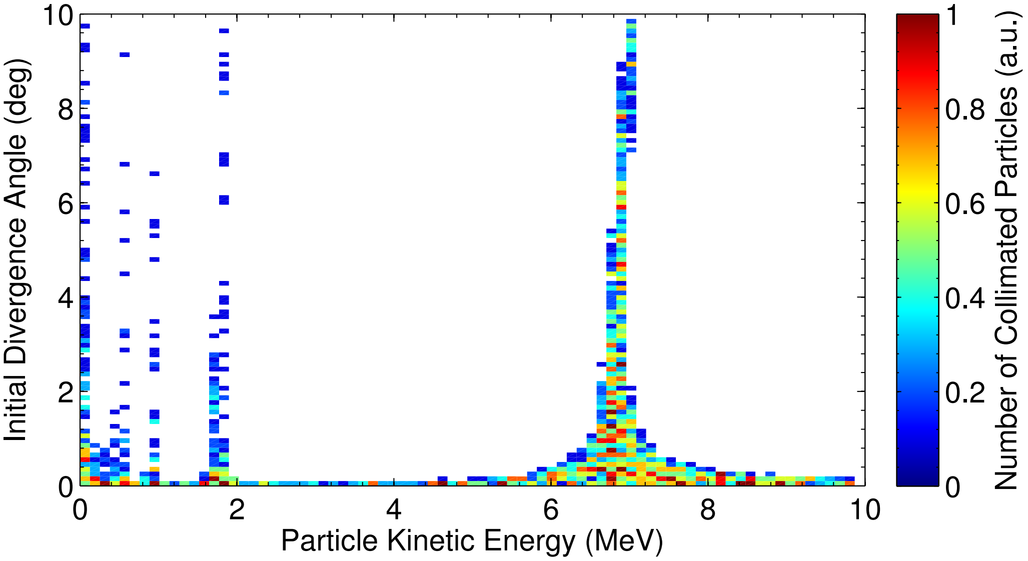

Figure 5.6: Collimation condition for a range of particle kinetic energies and divergence angles where the experimental spectrometer aperture and distance from source were used to define "collimation." Low energy particles, less than 2 MeV, reach the detector by passing through focus multiple times. Each energy and divergence bin was initialized with the same number of particles.

effects and are focused multiple times before being collimated. For each collimation condition node, the range of accepted energy narrows. Here, the primary focusing energy has a width of 100s of keV whereas the twice-focused energy is at least a factor of 2 smaller.

5.3 Experimental Results

Before measuring positron yields from different target materials, the coil magnetic field was tuned to maximize the number of positrons observed at the peak energy of the reference shots, 7 MeV. Figure 5.7(a) shows successive shots with increasing peak magnetic fields, scanning from the off (reference) condition up to 6.5 T. The positrons at the focusing criterium appear on the raw image plate as bright spots superimposed over the reference positrons and can be seen to shift to higher energy as the magnetic field is increased. The optimized field of $B_0 = 2.6$ T maximized the number of observed positrons by a factor of 20 at the peak and a factor of 6 in the integrated number of positrons compared to the reference shot, as seen in Fig. 5.7(a). Positrons observed in reference shots spanning the

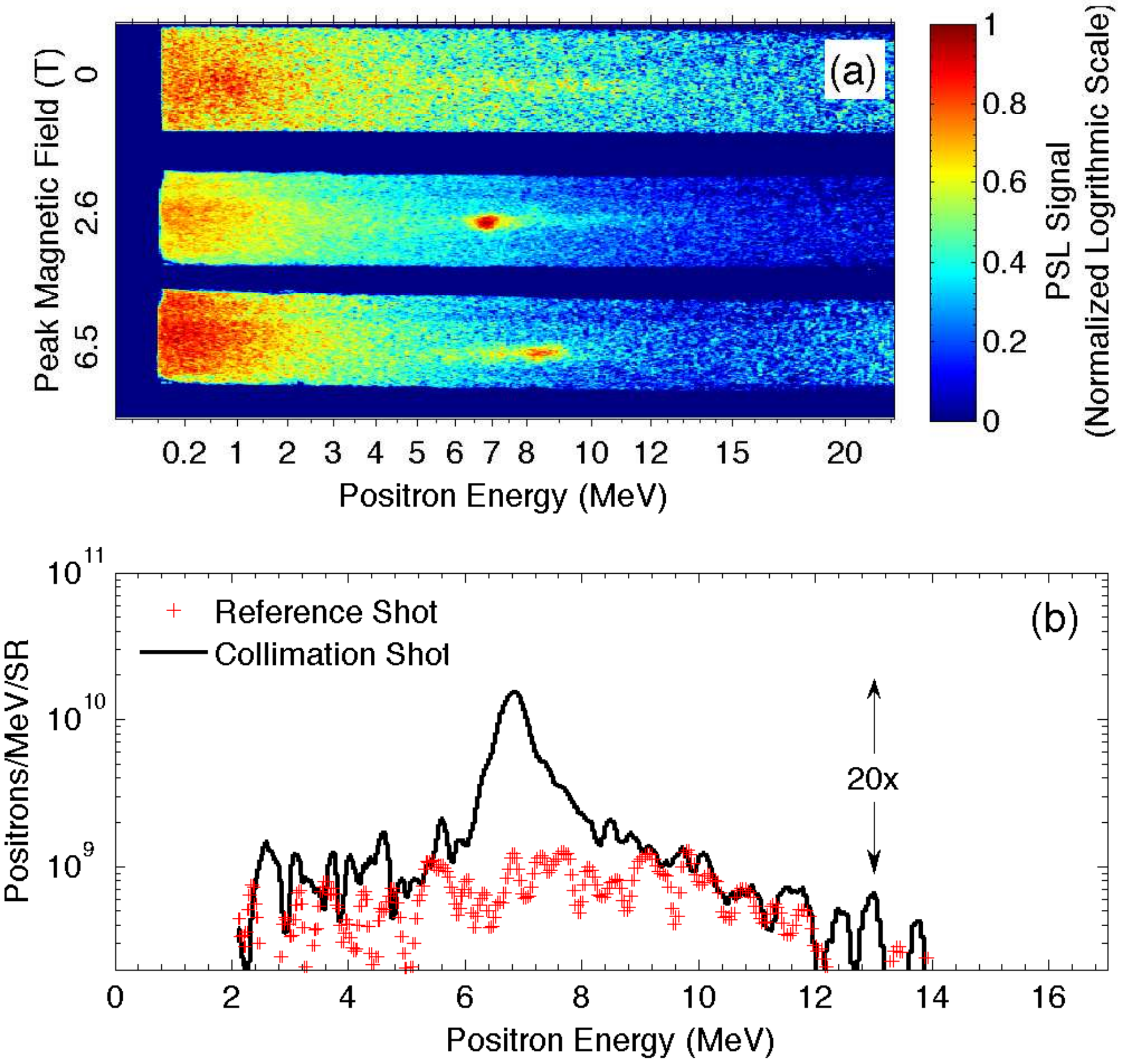

Figure 5.7: (a) Raw positron image plate data for various peak magnetic fields: off (top), 2.6 T (middle), and 6.5 T (bottom). The initial exiting positron signal can be seen just above background in the reference shot whereas the cases with focusing fields show signal significantly above background. As the magnetic field is increased, the energy at which positrons are collimated also increases.
(b) Positron spectra for the reference and 2.6 T shot shows a factor of 20 times increase in the maximum observed signal.

wide range of 5–10 MeV also appear in collimation shots since they essentially propagate along the axis and are unaffected by the focusing field. The positrons emitted at high angles and subsequently collimated appear superimposed over the on-axis particles.

The collimated positron spectrum has a larger energy spread than expected from the analytic or ray tracing models. This implies that the solenoid most likely has achromatic and spherical aberrations, which are characteristic of lenses with large bore aspect ratios, such as our coil. Using perfectly cylindrical fields to propagate the reference positrons at the optimized field strength, the ray tracing simulation predicts a maximum signal increase of ∼50 times that of the reference. The observed 20 times increase can be accounted for by imposing either small perturbations to the field symmetry (∼10%) or tilting the axis of the coil with respect to the particle beam axis (∼1–2°).

For the targets listed in Table 5.1, the emitted positron yield was measured using the collimating magnetic field and experimental platform described above. Pair yield has a complicated dependency on target parameters, which was discussed in detail in Chapter 2.1, where a brief review of these scalings is helpful to establish the correct independent variable on which to base the following yield measurements.

5.3.1 Theoretical Expectation of Material Dependent Pair Production Scaling

The cross section scaling of pair production is dependent on laser-accelerated electron energies, target atomic number, thickness, and areal density. The total cross section of the Trident process, σ_T , has been approximated [32, 33] for electron energies from the production threshold of $2mc^2$ up to 100 MeV by

$$\sigma_T = 5.22\, Z^2 \ln^3\left(\frac{2.30 + E_0}{2.53}\right) \mu\text{b}, \tag{5.7}$$

where E_0 is the kinetic energy of the incident electron in MeV. The probability of a pair being generated by the Trident process is then

$$dP_T = n_i \sigma_T d \propto N_A \left(\frac{Z^2 \rho d}{A}\right), \tag{5.8}$$

where n_i, d, and A are the ion number density, thickness, and atomic number of the target material, respectively and N_A is Avogadro's number.

The probability of generating a pair via Bethe-Heitler is the product of creating a bremsstrahlung photon,

$$dP_k = n_i \sigma_k d, \tag{5.9}$$

and creating a photo-ion positron-electron pair

$$dP_{e^+e^-} = n_i \sigma_{e^+e^-} d', \tag{5.10}$$

where σ_k and $\sigma_{e^+e^-}$ are the bremsstrahlung and photon-ion pair production cross sections and d' is the distance between the photon creation event location and the back of the target. The bremsstrahlung differential radiation cross section can be expressed by the Bethe-Heitler formula using a relativistic Born approximation and an unscreened nucleus as [23]

$$d\sigma_k = \frac{4Z^2 r_0^2}{137} \frac{dk}{k} \left[1 + \frac{E^2}{E_0^2} - \frac{2}{3} \frac{E}{E_0} \right] \left[\ln \frac{2EE_0}{k} - \frac{1}{2} \right], \tag{5.11}$$

where r_0 is the classical electron radius, k is the energy of the emitted photon, and E_0 and E are the initial and final energy of the electron, respectively. This approximation is valid for the high-energy bremsstrahlung photon tail, which is responsible for the majority of pair production in the Bethe-Heitler process. The unscreened, relativistic Bethe-Heitler formula for pair production by a photon is [26]

$$d\sigma_{e^+e^-} = 4Z^2 r_0^2 \left[\frac{E_{e^+}^2 + E_{e^-}^2 + \frac{2}{3} E_{e^+} E_{e^-}}{137 k^3} \right] \left[\ln \frac{2E_{e^+} E_{e^-}}{k} - \frac{1}{2} \right] dE_{e^+}, \tag{5.12}$$

where the total energy of the created positron and electron are E_{e^+} and E_{e^-}, respectively. In Eq. (5.11) and (5.12), the electron, positron, and photon energies are in units of mc^2. Since both σ_k and $\sigma_{e^+e^-}$ each scale as Z^2, the total Bethe-Heitler process has a birth yield of

$$dP_{BH} = dP_k \, dP_{e^+e^-} = n_i^2 \sigma_k \sigma_{e^+e^-} d d' \propto N_A^2 \left(\frac{Z^2 \rho d}{A} \right)^2. \tag{5.13}$$

The Bethe-Heitler and Trident pair generation are each proportional to the term $(Z^2\rho d/A)^n$, where $n = 1$ for Trident and $n = 2$ for Bethe-Heitler, where for thick high-Z targets, Bethe-Heitler will be the dominant process. For the case of Au, the pair production yield is balanced between the two at a target thickness of ∼20–40 μm, depending on initial electron temperature (see Fig. 2.6) [34, 106]. For the mm-scale target thicknesses in this study, the Trident contribution is estimated to be 2–12% of the total yield.

The number of emitted positrons will be reduced from the birth yield scaling by several scattering and absorption processes including ionization, below-threshold bremsstrahlung emission, photo nuclear absorption, collisional energy loss, and Compton scattering. The latter two being the dominant mechanisms that reduce the effective pair yield from the Z^4 dependence of the simple model. The collisional energy loss for electrons and positrons is linearly dependent on Z [50]. At the high energy limits ($>$ 1 MeV), the Compton scattering cross section is proportional to the number of electrons per atom, Z, where at energies near the creation threshold, Compton scattering is the dominant process. The result is an effective pair yield where the scaling proportionality is $n \ll 2$. The integrated contribution of these multiple scattering mechanisms extend beyond the simple explanation presented here. A Monte Carlo code, in which all processes can be considered in parallel, is well suited to address such a problem.

5.3.2 Comparison of Data and Monte Carlo Simulations to Derive an Empirical Scaling Relation

For each experimental target shot, the recorded positron spectrum was numerically integrated over the signal range of 5–10 MeV where the cumulative results are shown in Fig. 5.8, plotted against the normalized pair production term, $Z^2\rho d/A$. Each data point has been normalized to the laser energy delivered on target, which has a standard deviation from the mean of 6.5%. The confidence intervals on the data represents only an estimated uncertainty in the measurements where the distance between repeated data point give an approximation of the shot-to-shot variation. The full derivation of the EPPS uncertainty is given in Appendix C.

To complement the analytic model presented above, numerical modeling was performed

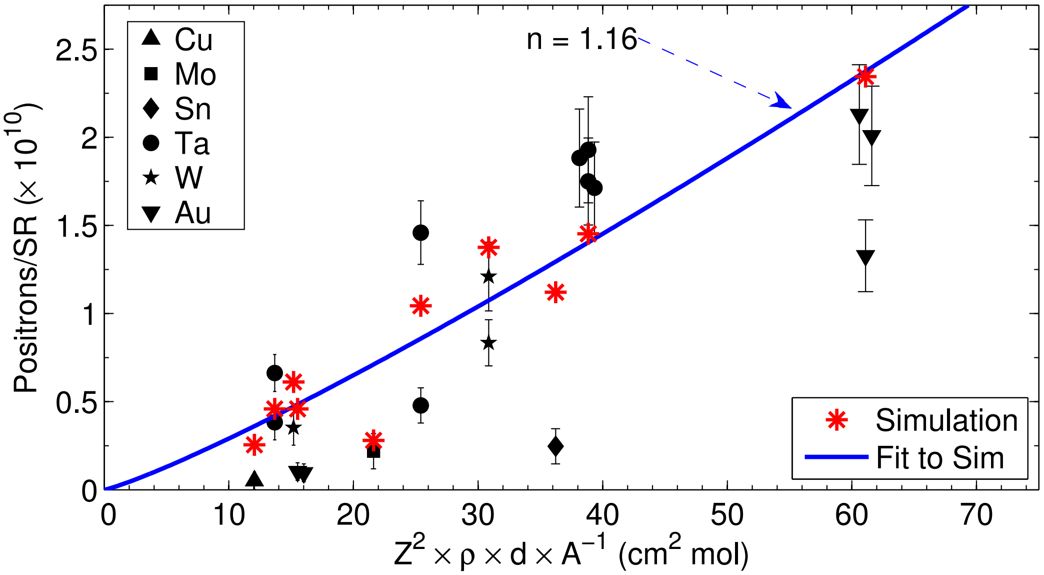

Figure 5.8: Positron yield per unit solid angle as a function of the pair production term $Z^2\rho d/A$ (markers). Monte Carlo simulations (red asterisks) show nominal agreement with the data, after the effects of sheath field acceleration and magnetic collimation are accounted for. A power law fit to the simulation (solid) has a scaling far below the Bethe-Heitler exponent of $n = 2$ due to attenuation in the target.

using the Monte Carlo particle tracking code Geant4. Simulations were initialized with 3×10^7 randomly seeded electrons in an exponential Maxwellian distributions with a 4 MeV characteristic temperature. Electrons were initially collimated and injected into simulated targets of the same material composition and dimension as in the experiment. Positrons were generated via the Bethe-Heitler method only, where the scattering and absorption mechanism included bremsstrahlung, multiple Coulomb scattering, particle induced x-ray emission, photoelectric absorption, electron and positron ionization, and Compton scattering. The energy, position, and momentum of each positron was recorded at the moment of birth and again if the particle escaped the boundary of the target. Simulations did not include self-generated or externally applied electromagnetic fields. To make a direct comparison between experiment and model, the sheath field acceleration and effective collimation from the coil must be accounted for.

Positrons with sufficient kinetic energy to escape the target are accelerated at the target-vacuum interface by a sheath electric field established by hot electrons streaming through the target. This imparts a shift in the positron energy spectrum equal to the magnitude of the sheath, which depends on the target surface area and is well described by a capacitor model [64]. The peak energy of emitted positrons was found to be 7 MeV for targets with a diameter or 6.3 mm, whereas the Geant4 calculations show a peak positron position of 2 MeV, consistent with previous numerical models [7]. In order to match data and simulation, an energy shift of 5 MeV was applied to simulated exiting positron spectrum.

From the particle ray tracing models and measured data, the estimated effective collimating conditions accept positrons with divergence angles below 10° and energies of 7.0 ± 0.7 MeV. Positrons with these parameters were collected from the energy-shifted simulation results. The total number of positrons from the simulation was then scaled by the input electron beam energy, assuming a laser-to-electron coupling efficiency of 50%. The simulation results are shown in Fig. 5.8 where, the simulation matches the data in both the magnitude and trend, given the scatter in repeated data points. A power law fit to the simulation shows that the position yield scales as $(Z^2\rho d/A)^{1.16}$. This agreement between the simulation and data supports the assumption that the pair production process is dominated by the Bethe-Heitler process for the current set of target thicknesses.

A more comprehensive survey of the positron scaling was performed by repeating the Geant4 simulations for target materials ranging from lithium ($Z = 3$) to uranium ($Z = 92$). For these simulations, the target thickness was kept fixed at a constant 1 mm and initialized electrons had a Maxwellian temperature of $kT_{e^-} = 4$ MeV where all materials used standard literature values for their densities [107]. Positrons of all energies were measured within the target when created, upon exiting the target in 4π, and exiting from the rear of the target within a 1 steradian cone. Each data set, shown in Fig. 5.9, is well described by a power law proportional to $(Z^2\rho d/A)^n$ where $n = 1.83(\pm 0.03)$, $1.26(\pm 0.06)$, and $1.13(\pm 0.05)$ for the created, exited, and 1 steradian collection regions, respectively. The positron creation scaling exponent of $n = 1.8$ is very close to the approximated expected value of 2 for the Bethe-Heitler process. This exponent is reduced by the effect of Compton scattering in the target as well as the yield scales closer to dd' instead of d^2. The difference in the exponents between created and exiting provides an order of magnitude estimate of the scattering loss due to target attenuation.

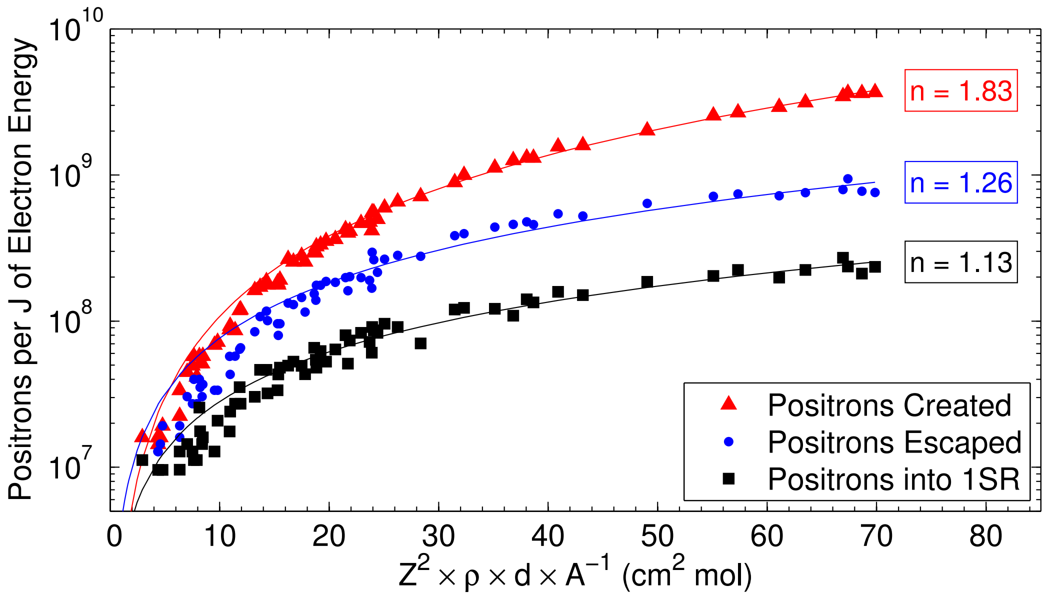

Figure 5.9: Positron yield scaling for all elemental materials of total thickness 1 mm. The total number of positrons created (triangles), exiting the target (dots), and exiting within a 1 steradian cone out the rear of the target (squares) are fit to a power law relation (solid lines) for each set of simulations. The $n = 2$ Bethe-Heitler scaling is nearly recovered for the birth yield.

If the initial electron temperature were allowed to vary, a corresponding change in the positron yield would be expected due to the energy dependence of the pair production cross sections. Shown in Fig. 5.10(a), the Maxwellian electron temperatures of the simulation were changed from $kT_{e^-} = 2$ MeV to 100 MeV where the scaling proportionality remains valid for targets of a constant thickness of 1 mm. The scaling power, determined by fitting the pair yields for each temperature and seen in Fig. 5.10(b), increases to a saturation limit of $n \approx 1.6$ at $kT_{e^-} = 100$ MeV since the pair production cross section is relatively energy insensitive above ∼50 MeV. The diminishing returns of the pair yield scaling suggests that, when designing an experiment which relies on pair production, the laser intensity should be chosen such that the produced electron temperature is of the order 20 MeV, after which it is better to increase the total laser energy to take advantage of the E_L^2 dependence demonstrated in Ref. 10.

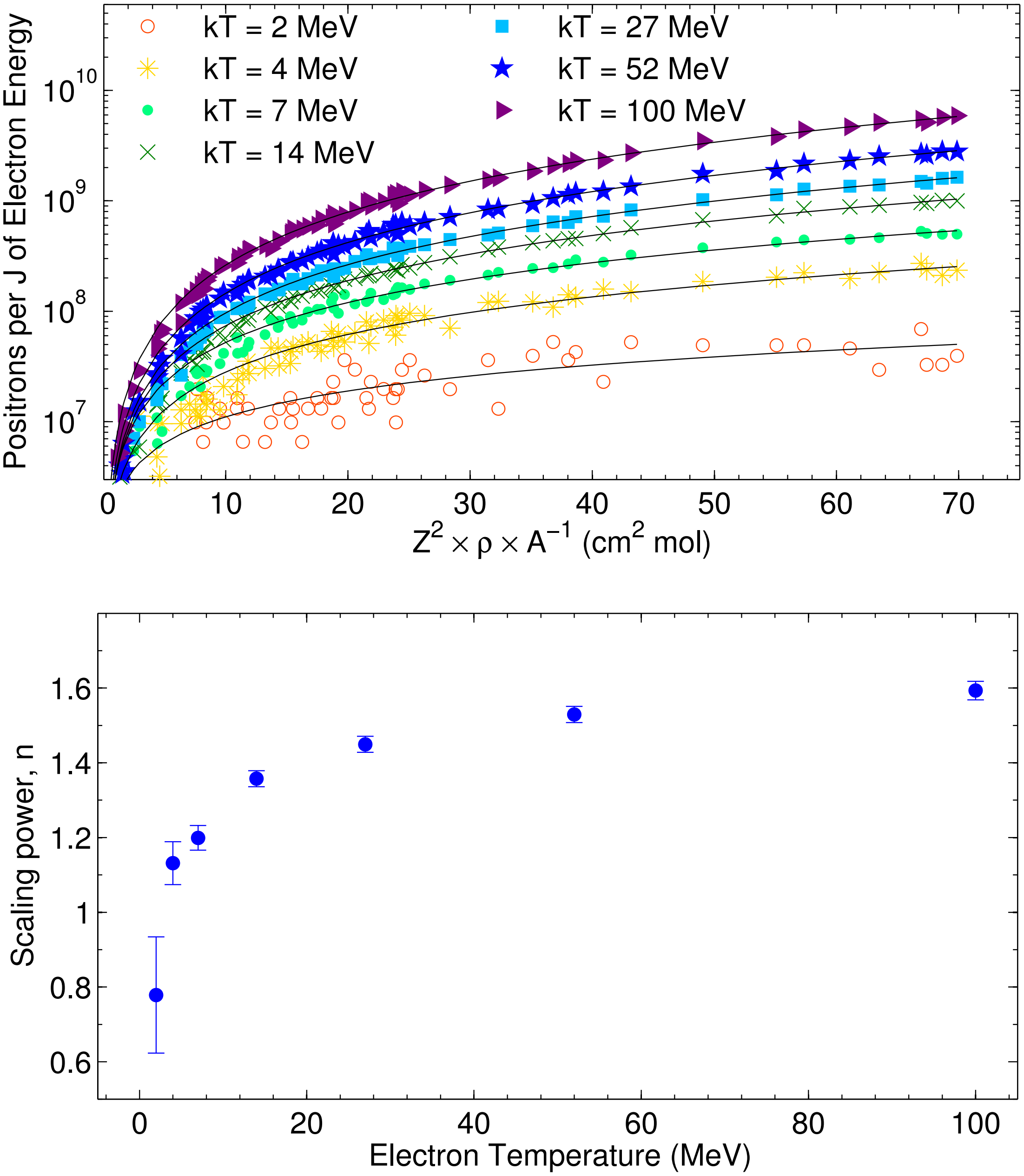

Figure 5.10: (a) Scaling of positron yield collected from a 1 steradian cone on the back surface of 1 mm targets for various materials and electron temperatures with power law fits applied to each temperature.
(b) The yield scaling, n, taken from the fits above, approaches a maximum value for the effective positron yield as a function of electron temperature.

5.4 Conclusions

In summary, we have experimentally measured the effective positron production scaling of target material in direct laser-matter interactions for a range of materials and thicknesses. The pair production mechanism is in agreement with the Bethe-Heitler method for the targets investigated; however, the positrons emitted into a jet on the rear surface only scales as Z^2 due to energy loss mechanisms in the target. A simple power-law scaling relation for the effective positron yield was established where the limitations of using ultra-hot electron distributions were determined. This work directly impacts the experimental design of future laboratory created relativistic positron jets applications such as in the injector stages of linear accelerators [8], in creating magnetically confined charge-neutral pair plasmas [16], and as a platform for astrophysically-relevant collisionless shock experiments [10, 14].

CHAPTER VI

Positron Radiography of Ignition-Relevant ICF Capsules

The unique characteristics of laser-produced positrons, namely their quasimonoenergetic and relativistic nature, offer possibilities to be used as tools to probe HED conditions. In this chapter, the feasibility of using such positrons as a radiographic tool is considered through Monte Carlo simulations. The results suggest that the currently available positron sources may be able to resolve the areal density and shell dimensions of direct-drive, ignition-relevant inertial confinement fusion (ICF) capsules or other similar warm dense volumes. The narrow bandwidth nature, short duration, small emittance, and moderate scattering cross sections of relativistic positrons provide a unique radiography platform to study high density plasmas and solids with the added capability of diagnosing dynamic electromagnetic fields. Using examples of the current ps-class petawatt lasers and the newly commissioned NIF ARC [108, 109] laser, it is demonstrated that areal densities between 0.02–0.2 g/cm^2 can be successfully radiographed. Positrons, with their low mass, are affected by electric and magnetic fields present on the surface of the capsule where it is estimate that this technique can be used with line-integrated magnetic fields of $\int B \times d\ell < 10$ T·mm.

6.1 Inertial Confinement Fusion

Nuclear fusion combines two lighter nuclei to form a heavier ion with a higher binding energy than either of the initial particles. The unconserved mass in the interaction is released in the form of kinetic energy, following Einstein's $E = mc^2$ relation. Among the highest yielding reactions occur between isotopes of hydrogen, deuterium (D) and tritium (T), to form helium. These reactions include

$$
\begin{aligned}
\mathrm{D} + \mathrm{T} &\rightarrow {}^{4}\mathrm{He} + n + 17.6\ \mathrm{MeV} \\
\mathrm{D} + \mathrm{D} &\rightarrow \begin{cases} \mathrm{T} + p + 4.0\ \mathrm{MeV} \\ {}^{3}\mathrm{He} + n + 3.3\ \mathrm{MeV} \end{cases} \\
\mathrm{D} + {}^{3}\mathrm{He} &\rightarrow {}^{4}\mathrm{He} + p + 18.3\ \mathrm{MeV},
\end{aligned}
$$

where the DT and D^{3}He reactions are most exothermic. The activation energy of these reactions, which prevents spontaneous fusion events, requires that the system kinetic energy is large enough to overcome the Coulomb repulsion. This threshold is reduced slightly due to quantum tunneling, where the kinetic energy needed for a DT reaction is 1.2 MeV and 4.7 MeV for D^{3}He.

For the purpose of energy gain, a controlled chain reaction is necessary where the released kinetic energy of the daughter particles drives further fusion reactions. However, heating the fuel to these energies while maintaining high densities to facilitate the steady-state burn is difficult; the pressure increases in the plasma as it heats, causing it to expand if not spatially confined. Inertially confining the fuel in a spherical implosion attempts to increase the density for a long enough time to allow a burn wave to propagate throughout the fuel. The burn parameter is a function of the reaction rate, fuel density, and ion temperature, given in units of areal density. For ICF temperatures, a threshold on the order of 1 g/cm^2 is required to reach conditions which will burn a majority of the fuel.

The technique of ICF [110] uses symmetrically configured lasers to ablate away the shell of a fuel capsule. The ablation pressure causes the fuel to converge to 300–1000 times solid density with stagnation radii on the order of 10–100 μm. In direct-drive ICF, lasers are focused directly on the capsule and absorbed by the shell. Indirect-drive ICF uses a gold canister, called a hohlraum, around the capsule where laser energy is first converted into x-rays. These x-rays bathe the capsule in a spatially smooth, spectrally Planckian radiation that drives the shell ablation. For each of these schemes, a number of instabilities arise on

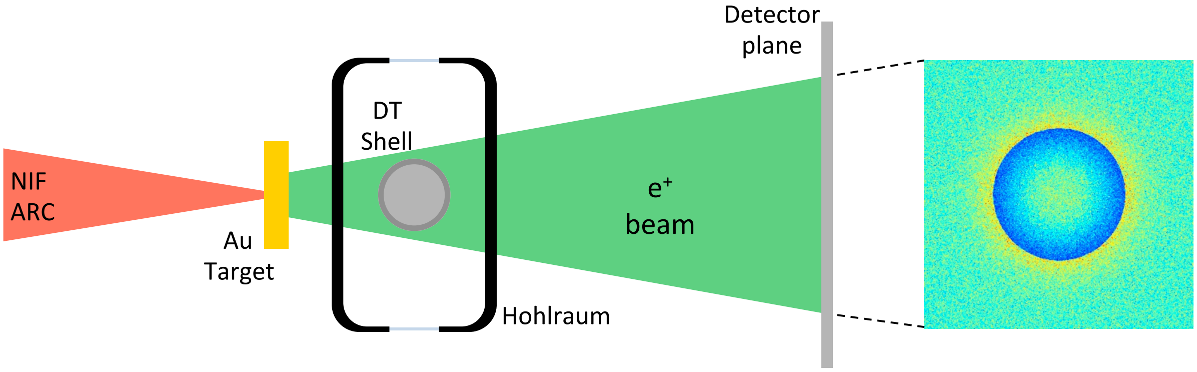

Figure 6.1: A short pulse incident on a gold target creates a positron beam that area-backlights an imploding ICF fuel capsule. A hohlraum and 2D radiograph are shown for completeness. In a full-scale experiment, considerations would need to be made to mitigate scattering from the gold hohlraum walls, if present, and to charge separate the copropagating positrons and electrons.

the vacuum-shell and shell-fuel interfaces that breaks the implosion symmetry, reducing the final areal density of the fuel core.

At the NIF at LLNL, as well as at the other ICF facilities, a great deal of effort is taken to characterize, understand, and mitigate these instabilities by measuring the in-flight shape of the fuel during the compression and deceleration phases of the implosion. Currently, x-ray diagnostics are used to quantify the fuel shape and neutron measurements to infer the fuel areal density. The addition of a new method to directly measure, or even constrain, the metrics of an ICF implosion will help to better understand these implosions, taking one step closer to bringing star power to Earth.

6.2 Positron Radiography of Fuel Capsules

An area-backlighting radiography source must have characteristics of being monoenergetic, have high brightness, and originate from a small spot size, all of which contribute to the spatial resolution of the image. The energy of the source particle and scattering amplitudes within the material of interest determines the optimal areal density where radiography can be applied. Here, we investigate the measurable range of areal densities using the parameters of current and future positron sources.

A number of assumptions are made to simplify this very complex problem to investigate the feasibility of positron radiography, where a mockup of an experimental setup is shown in Fig. 6.1. Order of magnitude estimates for all physical values have been taken for the presented simulations and analysis with ranges noted for all parameters. This ensures that the final result best represents the dominant physics mechanisms and gives a valuable first order approximation of the platform.

The final design specifications of the NIF ARC short pulse are 12 kJ of energy in a pulse duration of 1–30 ps. From the energy scaling relations presented in Ref. 10, a 10 ps laser with the full 12 kJ of energy is expected to produce 3×10^{13} positrons using a 1 mm Au target. Currently, Omega EP is the most efficient positron production laser at $N_{e^+} \simeq 10^{12}$. Assuming the divergence of the positrons follows Liouville's Theorem, as described in Ref. 63, the mean energy of the beam and its cone angle are inversely proportional where the minimum value asymptotically approaches 10°. For the presented simulations, the position beam is modeled as a spatially uniform flat top beam with a minimum divergence of 10°, overfilling the target by several times the shell radius. It is expected that the mean positron energy grows with laser energy, limited only by the maximum sheath field potential on the target surface. Currently available, 1.5 kJ lasers are capable of generating positrons with peak energies near 30 MeV [63]. As such, for these simulations, a conservative value of 30 MeV is used, with the anticipation that higher energies could be used for larger laser systems. The standoff distance between positron source and radiograph object is constrained by experimental geometry. With either direct or indirect drive ICF, the symmetry of the lasers or the hohlraum limit the minimum distance to a nominal 5 mm.

The simulated target is a simplified case of an ignition-relevant fuel capsule with a silicon doped (2%) CH plastic ablator shell and a solid DT fuel ice layer [111]. The capsule has an initial preshot radius of $\sim$1 mm where the thickness of the shell and fuel are $\sim$200 μm and $\sim$100 μm respectively. Each ICF campaign is intended to investigate a specific physics mechanism and capsules are tailored to best achieve their primary goal where complicated shell layering, dopants, and geometries are common. We have chosen to restrict the scope of this work to consider only the simplest form where the variants are constrained to fuel-only and fuel-with-ablator capsules. More complicated geometries and inhomogeneous conditions,

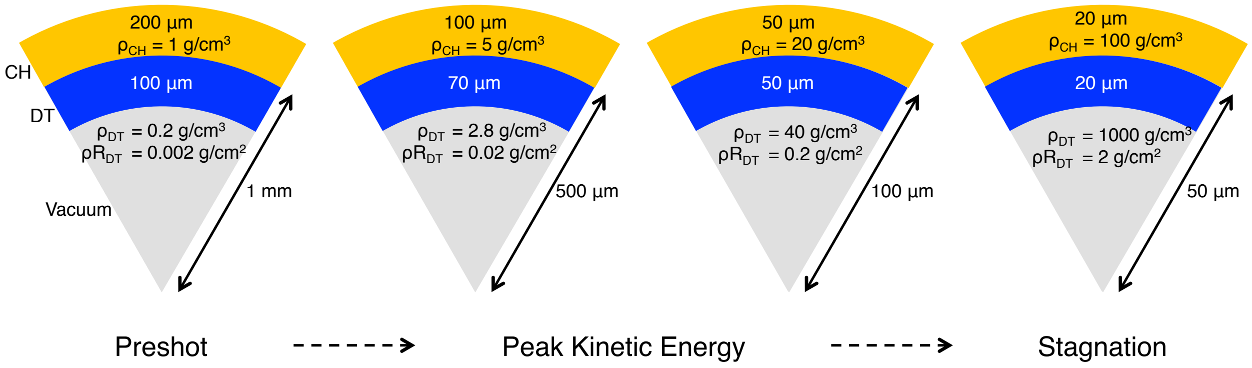
200 µm
ρCH = 1 g/cm3
CH
100 µm
DT
ρDT = 0.2 g/cm3
ρRDT = 0.002 g/cm2
1 mm
Vacuum
100 µm
ρCH = 5 g/cm3
70 µm
ρDT = 2.8 g/cm3
ρRDT = 0.02 g/cm2
500 µm
50 µm
ρCH = 20 g/cm3
50 µm
ρDT = 40 g/cm3
ρRDT = 0.2 g/cm2
100 µm
20 µm
ρCH = 100 g/cm3
20 µm
ρDT = 1000 g/cm3
ρRDT = 2 g/cm2
50 µm
Preshot
Peak Kinetic Energy
Stagnation

Figure 6.2: Simplified cross section diagrams of ICF capsules during the implosion phase. Shocks are driven through the ablator to accelerate and compress the layer of DT ice formed on the inner surface. After the driver turns off, and the fuel has acquired its maximum kinetic energy, the capsule decelerates reaching a peak compression areal density of $\sim$2 g/cm^2.

such as coronal plasmas, modulations in thickness and densities, or the hohlraum walls and windows, are not considered.

Four fuel capsule areal densities ranging from 0.002–2 g/cm^2 are investigated, which span from uncompressed to capsule stagnation densities. The fuel is a 50/50 mix of deuterium and tritium, which is typically the mix ratio for high-yield targets, modeled as a uniform, isothermally compressible gas at solid densities. The capsule ablator has densities and shell thicknesses dependent on the phase of the implosion, where at maximum compression, $\rho_{\mathrm{CH}} = \frac{1}{10}\rho_{\mathrm{DT}}$. Hydrodynamic simulations [112] show that the ablator is highly dynamic, ejecting very large (mm-scale) and relatively dense ($>10^{-2}$ g/cm^3) coronal plasmas, mainly controlled by the relative timing and intensity of the laser pickets designed to launch shock waves into the fuel. For this study, the coronal plasma is ignored and the shell is modeled with an infinitely steep density gradient. Rounded estimates for the dimensions and densities of the fuel and capsule during the implosion are shown as diagrams in Fig. 6.2. To investigate the energy loss through multiple scatter events within the target, the positron beam was modeled as either a realistic Gaussian distribution centered at 30 MeV with a 2 MeV FWHM or a monoenergetic 30 MeV spectrum. All materials were modeled as cold matter which will underestimate the stopping power and Coulomb scattering by $\sim$30% compared to other Monte Carlo codes and analytic models for warm (5 keV) dense (300 g/cm^3) matter [113, 114], which is applicable to the conditions of central implosion hot spot.

In order to overfill the target area by roughly a factor of two, the distance between source and capsule was changed accordingly, while keeping the detector plane at a constant 30 cm from the radiography target where the system magnification was between 15 and 60. The standoff distance to the detector is similar to other currently deployed diagnostics at the NIF and Omega facilities. A modeled perfect detector collects both the positron position and energy, simulating either a 2D radiograph or an EPPS-like charged particle spectrometer with an extended slit. Only positrons are collected where the dose associated with bremsstrahlung photons or Compton electrons emitted from the target are not considered.

A total of 2×10^7 positrons were modeled using Geant4 to radiograph four fuel-only capsules with the results shown in Fig. 6.3. The positron number density at the target plane ranged from $1.6 \times 10^8/\text{mm}^2$ to $4.3 \times 10^5/\text{mm}^2$ for the highest and lowest magnification, respectively. An Omega EP positron source is expected to produce positron area densities 10^3–10^4 times higher than this, reducing the statistical noise observed in the presented radiographs. Each radiograph image shows large contrast at the edges of the target where a vertically-integrated lineout of the center 10% of the shell area has modulations in positron signal varying between 50% for the uncompressed capsule to 87% for the in-flight capsules. At stagnation, positrons are scattered away from the target, leaving a completely opaque shadow of the capsule. This shows that the shell radial dimensions can always be retrieved in the high-density limit. Before stagnation, a pileup of signal can be seen surrounding the targets creating a halo of positrons. Coulomb scattering will reduce incident positron energies by only a few percent while also imparting a very small transverse momentum increase. These small angular deviation give rise to the observed ring of signal around the target for areal densities up to 0.2 g/cm^2. The density dependence of the scattered positrons provides a constraint on the recovery conditions of the target. For the stagnation case, however, the scattering strength is a limiting factor to the 2D radiographs where the positrons scatter into larger angles and the image appears uniformly illuminated with a complete shadow around the target.

Despite a lack of radial contours for the stagnation capsule, the energy spectrum of the down-scattered particle reveals density-dependent signatures. A monoenergetic source

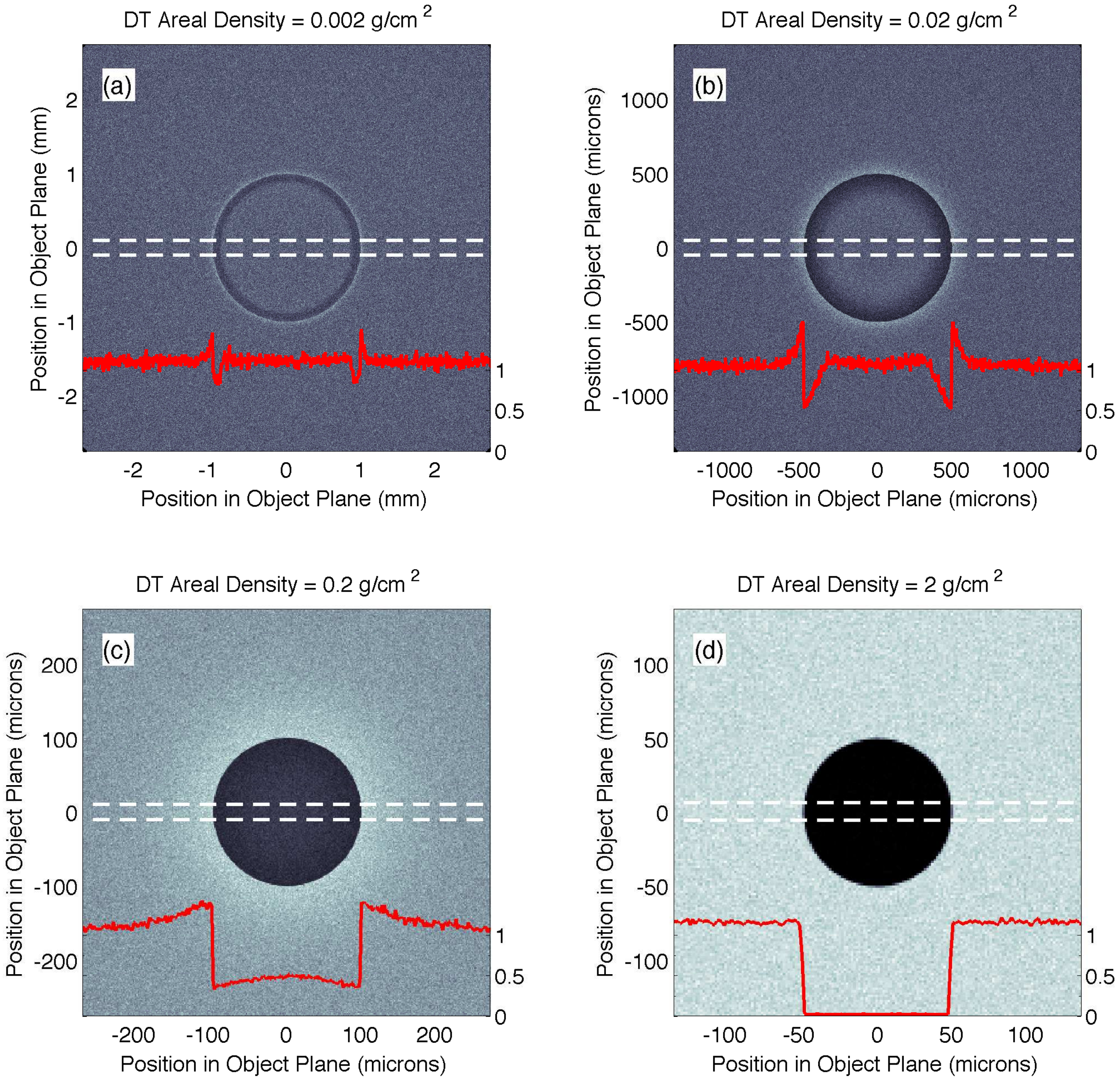

Figure 6.3: Positron radiographs of fuel-only ICF capsules at various in-flight configurations using 30 MeV Gaussian-spectrum positrons. Lineouts of positron signal are taken horizontally between the dashed lines (±5% of shell radius) and plotted below as in solid red. An arbitrary unit scale for the lineout (right axis) is normalized to the background signal. The fuel radius R_{DT}, shell thickness dR_{DT}, and system magnification, M, are as follows:
(a) Uncompressed: $R_{\mathrm{DT}} = 1$ mm, $dR_{\mathrm{DT}} = 100$ μm, $M = 15$.
(b) Inflight: $R_{\mathrm{DT}} = 500$ μm, $dR_{\mathrm{DT}} = 70$ μm, $M = 30$.
(c) Inflight: $R_{\mathrm{DT}} = 100$ μm, $dR_{\mathrm{DT}} = 50$ μm, $M = 60$.
(d) Stagnation: $R_{\mathrm{DT}} = 50$ μm, $dR_{\mathrm{DT}} = 20$ μm, $M = 60$.

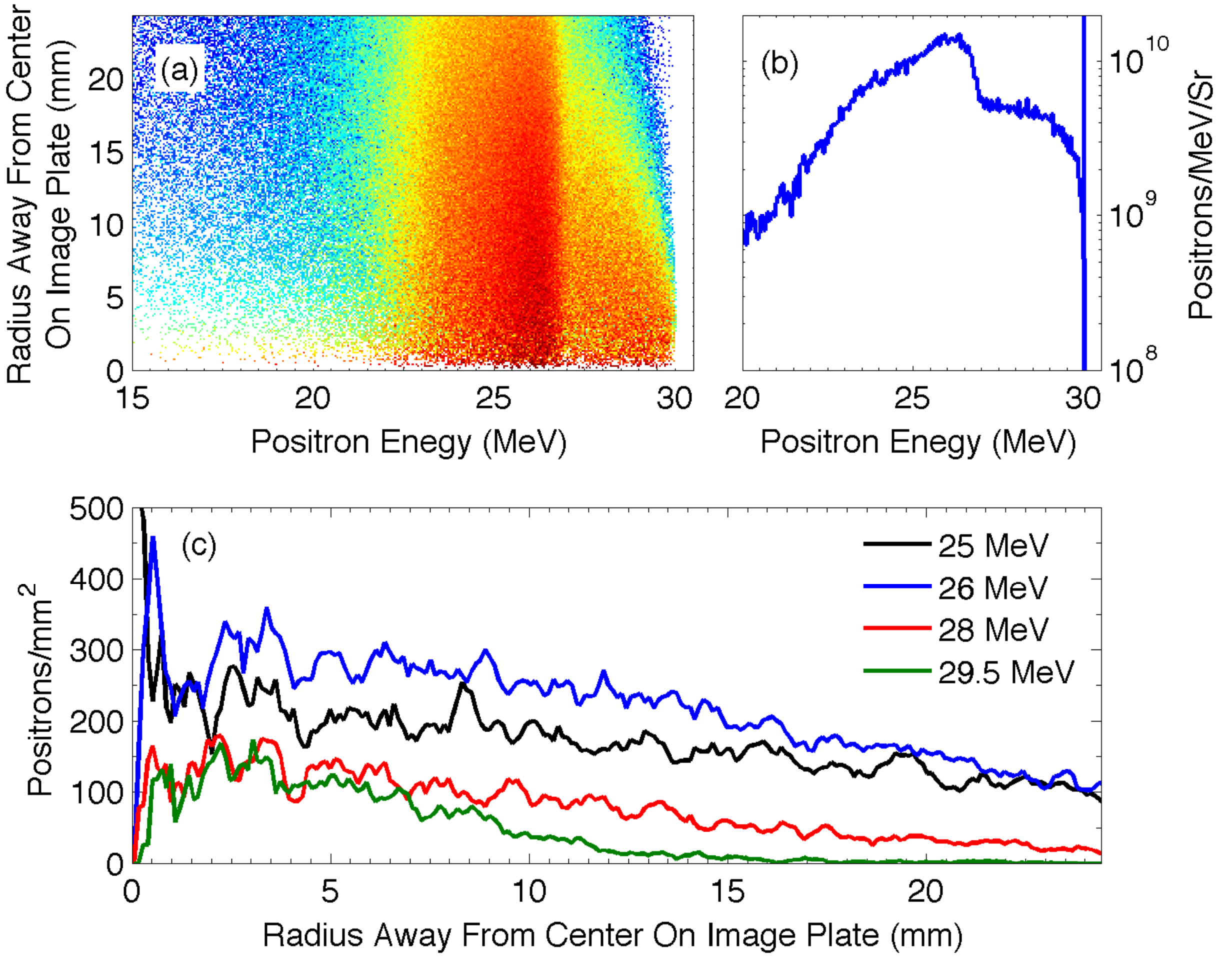

Figure 6.4: Positron spectrum after radiographing a fuel-only ICF capsule at peak areal density (2 g/cm^2) using monoenergetic 30 MeV positrons, assuming a total flux of $N_{e^+} = 3 \times 10^{13}$. Positrons that have been energy down-scattered can reveal information about the density of the material it traversed.
(a) Spatial and spectral components of scattered positrons.
(b) Energy spectrum of all positrons collected using a 1 mm slit.
(c) Radial lineouts from (b) at various energies. The highest energy positrons have a large radial dependence whereas positrons that have lost more energy are scattered into much larger angles.

was used to discriminate between initial and scattered particles, where a radially integrated positron spectrum for the stagnation case can be seen in Fig. 6.4(a) in which the colorscale denotes signal intensity. Positrons that have incurred the least energy loss, arriving at the detector with most of the initial 30 MeV energy show the strongest radial dependence. This is demonstrated further by integrating radially for various energies where positron signal falls off slightly for lower energies (see Fig. 6.4(c)). The pronounced feature in the integrated energy spectrum observed at 27 MeV in Figs. 6.4(a) and 6.4(b) is due to the hollow-core geometry of the shell. The on-axis positrons traverse significantly less material than those which take the chord length of a solid shell. The total number of positrons arriving at the detector is estimated by assuming a 1 mm entrance slit to a detector and an initial beam strength of $N_{e+} = 3 \times 10^{13}$. The maximum signal of 10^{10} positrons/MeV/Sr at 27 MeV is well above the typical noise threshold for the current design of EPPS. If the positron beam were to be produced by Omega EP, the signal strength remains above the detector threshold of 10^8 positrons/MeV/Sr. In an environment with a significantly higher background, such as a 12 kJ ARC shot, it is anticipated a signal which is 100 times the background for 1 kJ Omega EP shots (as in Fig. 6.4(c)) would remain above the noise for a well-shielded image plate charged particle spectrometer.

The radiograph simulations were repeated for the case that includes both the fuel and ablation shell with results shown in Fig. 6.5. Here, the presence of the shell is most dramatically seen in the uncompressed capsule where the density is significantly larger than the DT ice. Small perturbation, on the order of the simulation noise, exists in the intensity lineout shape for the two moderate areal densities, 0.02 and 0.2 g/cm^2. In each case, however, a high-contrast target interface exists allowing for accurate measurement of the shell size and spatial modulations, if any.

The charged nature of positrons causes them to be susceptible to electric and magnetic fields surrounding the capsule. Proton deflectometry has successfully been used to measure temporally dynamic magnetic fields driven by laser-matter interactions using a grid projection [115, 116]. Magnetic fields have been measured using this technique on the surface of ICF capsules to be on the order of and 100 T [117, 118]. Therefore, spatially uniform or slowly varying fields could, in principle be measured by protons; however, their low mass

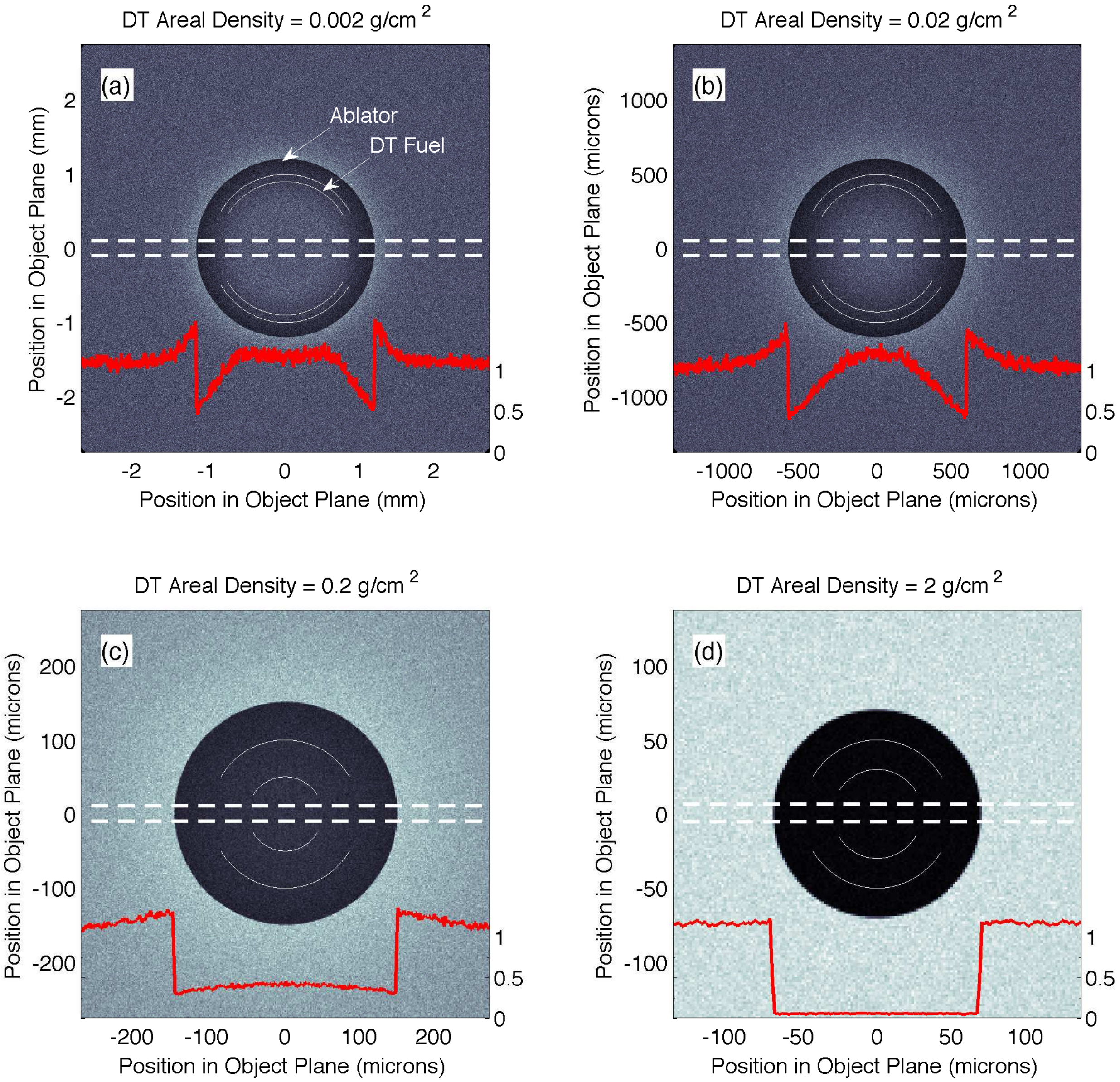

Figure 6.5: Positron radiographs of fuel and ablator ICF capsules at various in flight configurations using Gaussian 30 MeV positrons. Lineouts of positron signal are taken horizontally between the dashed lines and plotted below (solid). An arbitrary unit scale on the lineout (right axis) is normalized to the background signal. Thin lines superimposed over the radiograph show the boundary between vacuum, fuel, and ablator. The geometry of the capsules are as follows:
(a) Uncompressed: $R_{\mathrm{DT}} = 1$ mm, $dR_{\mathrm{DT}} = 100$ μm, $dR_{\mathrm{CH}} = 200$ μm.
(b) Inflight: $R_{\mathrm{DT}} = 500$ μm, $dR_{\mathrm{DT}} = 70$ μm, $dR_{\mathrm{CH}} = 100$ μm.
(c) Inflight: $R_{\mathrm{DT}} = 100$ μm, $dR_{\mathrm{DT}} = 50$ μm, $dR_{\mathrm{CH}} = 50$ μm.
(d) Stagnation: $R_{\mathrm{DT}} = 50$ μm, $dR_{\mathrm{DT}} = 20$ μm, $dR_{\mathrm{CH}} = 20$ μm.

limits the maximum fields the particle can traverse before being deflected beyond the solid angle of a practical detector.

For a geometry such as the one described here, a maximum deflection distance of 1–5 cm is tolerable. The displacement, ξ, of a particle relative to its trajectory without a magnetic field is [119]

$$\xi = -\frac{qa(A-a)}{Amv}\int \mathbf{B} \times d\ell, \tag{6.1}$$

where q, m, v are the particle charge, mass, and velocity. The geometric parameters A and a are the distance from source to detector and source to target respectively and $d\ell$ is the differential path length the particle traverses through a magnetic field $\mathbf{B}$. For the maximum magnification scenario, $A = 305$ mm, $a = 5$ mm, such that $\xi = 3\int \mathbf{B} \times d\ell$, where $\mathbf{B}$ and $d\ell$ are measured in Teslas and meters, respectively. Therefore, positron deflectometry for this geometry is limited to magnetic fields on the order of 10 T over spatial durations of $\sim$1 mm. If the detector geometry restrictions are more stringent where the field of view is on the order of 1 mm, similar to the case for the current design of the EPPS, the maximum magnetic field reduces 1 T over 1 mm.

This feasibility study concludes that currently available positron sources have the necessary energy bandwidth, mean energy, and divergence necessary to successfully radiograph a fuel-only ICF capsule. With the addition of experimental complexities, namely the ablator shell, the scattering of positrons within the fuel becomes indistinct. For indirect drive, with hohlraum walls, the signal would be obscured further. It is conceivable, that in a direct drive scenario where the laser nearly burn through the entire ablator, that positron radiography would be successful. Further work is necessary to determine the optimal parameters, where the current study was designed only to investigate the most ideal platforms. Additional uses for positrons in this regime of warm dense matter would be to allow positrons to thermalize in the volume of interest and observe the Doppler shifted annihilation radiation which is a measure of volumetric temperature. This is briefly explored in Appendix B.

CHAPTER VII

Conclusion and Future Work

Laser-produced positron-electron pair jets are unique in their capability to recreate aspects of fundamental physics involved with some of the most energetic astrophysical phenomenon in the universe. This dissertation described experiments and simulations that attempted to meet the challenge of accurately predicting, controlling, and manipulating created pairs. These results contribute to the goal of enabling novel laboratory-based studies of astrophysically-relevant shocks and collective behaviors of relativistic pair plasmas.

Laser-wakefield electron sources were explored as a compact, high repetition rate platform for high energy pairs with potential applications to the creation of charge-neutral pair plasmas. This work was partially motivated by reports of very dense, low-divergence positrons sources using only moderate LWFA beam parameters. It was found that, even for initially highly energetic and collimated electrons, energy loss and scattering mechanisms in the target create a fundamental limit to the divergence and energy spectrum of the emitted positrons. Collisional Coulomb scattering dominates over bremsstrahlung, pair production, and Compton scattering as the largest contributor to transverse momentum for even targets of 100 μm in thickness. This result shows that the initial divergence in the plasma accelerated electrons is inconsequential to the final emitted positron beam. If, however, the emitted positrons can be collimated, the LWFA electrons could be a candidate platform for future laboratory-astrophysics experiments.

An experiment investigating the effective position yield for any elemental target using picosecond-class ultraintense lasers was performed. It was found that a simple power-law scaling, derived from the Bethe-Heitler pair production process, is sufficient to describe the positron emission results for all target materials. Monte Carlo simulations further suggest that a laser intensity plateau exists where it is ideal to generate a Maxwellian electron temperature in the range of 15–20 MeV. Once this intensity is reached, positron production is best maximized with increasing laser energy. This experiment relied on an axially symmetric electromagnetic coil that was used to focus emitted pairs, increasing the effective collection angle of the detector and facilitating the measurement of positrons from mid-Z materials. A collimating coil such as the one used here shows promise as a means to maintain a pair plasma over a large distance with only moderate growth of the transverse spot size and could be easily coupled to the LWFA platform.

Finally, a future application of laser-generated pairs was considered by exploring the feasibility of radiographing an imploding inertial confinement fusion capsule for ignition-relevant conditions. For an in-flight areal density of 0.02–0.2 g/cm^2, currently available positron sources are capable of making density and spatial measurements of the compressed deuterium-tritium fuel. It was found that for higher densities the shape of the shell can be recovered, and if an imaging spectrometer were to be used, it is possible to use the radial distribution of down-scattered positrons to constrain the capsule density.

Future experiments include testing fundamental relativistic plasma physics by interacting low-divergence, high-density pair plasma jets with ambient plasma or with another jet. Although such interactions have been considered for some time, the experimental platform has never existed to compare competing models of energy transfer in single-component or two-component plasmas. Using the next generation lasers, under construction or recently commissioned, interacting jets of pair plasmas will be capable of reaching the linear regime of collisionless shock creation and near-future laser platforms could reach the nonlinear regime. The field of laser-generated positrons is very young with many questions remaining to be answered. It is the hope of the author that a meaningful step forward has been made with the contributions included in this dissertation.

APPENDICES

APPENDIX A

Quick References

This section is designed to be a quick reference to many of the equations and calculations that are either covered extensively in the body of this work or are reformulations of common expressions. The Lorentz factor, energy, and momentum of a particle are related by

$$\gamma = \frac{KE + mc^2}{mc^2} = \frac{1}{\sqrt{1-\beta^2}} = \sqrt{1 + \frac{p^2}{m_e^2 c^2}}, \tag{A.1}$$

$$\beta = \frac{v}{c} = \sqrt{1 - \frac{1}{\gamma^2}}, \tag{A.2}$$

$$E = pc, \text{ and} \tag{A.3}$$

$$p = \gamma m v. \tag{A.4}$$

The normalized laser vector potential is given by

$$a_0 = \frac{e|\mathbf{E}_L|}{m_e \omega c} = \frac{e|\mathbf{E}_L|\lambda_L}{2\pi m_e c^2} = \frac{e\lambda_L}{2\pi m_e c^2}\sqrt{\frac{2I_L}{\epsilon_0 c}} = 0.8549(I_{18}\lambda_{\mu m}^2)^{1/2}. \tag{A.5}$$

The relativistic laser regime begins when $a_0 > 1, I_L = 1.2 \times 10^{18}$ W/cm^2 for 1.053 μm laser light. The critical density is defined by the point at which the plasma frequency is equal to the laser frequency. An electromagnetic field cannot propagate in a plasma with an electron density at or above this value. The critical density is then,

$$n_c = \frac{\omega_L^2 m_e}{4\pi e^2} \simeq 1.1 \times 10^{21}\ \lambda_{\mu m}\ \text{cm}^{-3}. \tag{A.6}$$

APPENDIX B

Doppler Broadening of Annihilation Radiation

Positron and electron pairs that annihilate with a nonzero kinetic energy emit photons of energy greater than the rest mass of an electron. From a laboratory rest frame, the net momentum of the pairs at annihilation will affect the observed energy of the annihilation photons. If the pairs are moving away from the observer, the 511 keV photon will appear red-shifted, while pairs moving towards the observer will appear blue-shifted. The Doppler broadening of the annihilation radiation has potential to be used as a diagnostic of high energy density plasmas in the laboratory.

Consider a region of quasi-stable, hot, dense plasma with a temperature of the order 100 eV. If laser-generated pairs are introduced to the system, a fraction of the lowest-energy positrons, which make up the majority of the initial population, will begin to scatter from and thermalize with the background plasma. If the confinement time of the plasma is long enough, the thermalized positrons will annihilate and a measure of the Doppler width gives a direct measurement of the plasma temperature. This technique has been used to determine the plasma temperatures of solar flares [120]. Furthermore, the pair annihilation rate is density dependent with lifetimes on the order of ps after thermalizing. If the positrons could be slowed down and injected at defined times into a dynamic system, snapshots of the density and temperature are possible.

To better understand the the signal broadening, we use the frame in which the center of mass of the pair is at rest, $\mathbf{p}_+ = -\mathbf{p}_-$, where $\mathbf{p}_+$ and $\mathbf{p}_-$ are the momentum of the positron and electron respectively. A transformation from the center of mass system to a laboratory reference frame uses the Lorentz transformation,

$$\omega = \gamma \left(\omega' \pm \mathbf{k}\cdot\mathbf{v}\right) = \gamma\omega'\left(1 \pm \frac{v}{c}\cos\theta\right), \tag{B.1}$$

where ω is the frequency of the photon in the laboratory frame, ω' in the pair frame, $|\mathbf{k}| = \omega/c$ for electromagnetic radiation, and $\mathbf{v}$ is the center of mass velocity in the laboratory frame. The angle θ is defined between the center of mass momentum and the angle of observation. The choice of $\pm$ is whether the center of mass is moving towards or away from the observation point. Since ω is directly proportional to E, the photon energy, this can be rewritten for the case of a pair annihilation to be,

$$E' = \gamma mc^2\left(1 - \frac{v}{c}\cos\theta\right). \tag{B.2}$$

Here, we are considering a case in which the electrons and positrons are thermalized with the bulk, the velocities of the particles are non-relativistic and can be expressed by a Maxwell-Boltzmann distribution,

$$f(\mathbf{v}) = \left(\frac{m_e}{2\pi k_B T}\right)^{3/2}\exp\left(-\frac{\frac{1}{2}mv^2}{k_B T}\right), \tag{B.3}$$

where k_B is the Boltzmann constant and T is the thermalized temperature.

A photon emitted in the same direction as the center of mass velocity obtains the largest possible Doppler shift. It is equivalent to say $\cos\theta = 1$ resulting in $|\mathbf{v}| = c\,(E/mc^2 - 1)$. Substituting into Eq. (B.3) gives a distribution of the form,

$$f(E) = \left(\frac{m_e}{2\pi k_B T}\right)^{3/2}\exp\left(-\frac{(E/mc^2 - 1)^2}{2mc^2 k_B T}\right). \tag{B.4}$$

Comparing the above equation with the form of a Gaussian distribution, the FWHM is given by

$$\text{FWHM} = 2\sqrt{2\ln(2)}\sigma = 2\sqrt{2\ln(2)}\sqrt{mc^2 k_B T} = 1.5\ \text{keV}\sqrt{\frac{T}{10^4\ \text{K}}}. \tag{B.5}$$

For a bulk electron temperature of 200 eV (2.3×10^6 K), the expected Doppler broadened

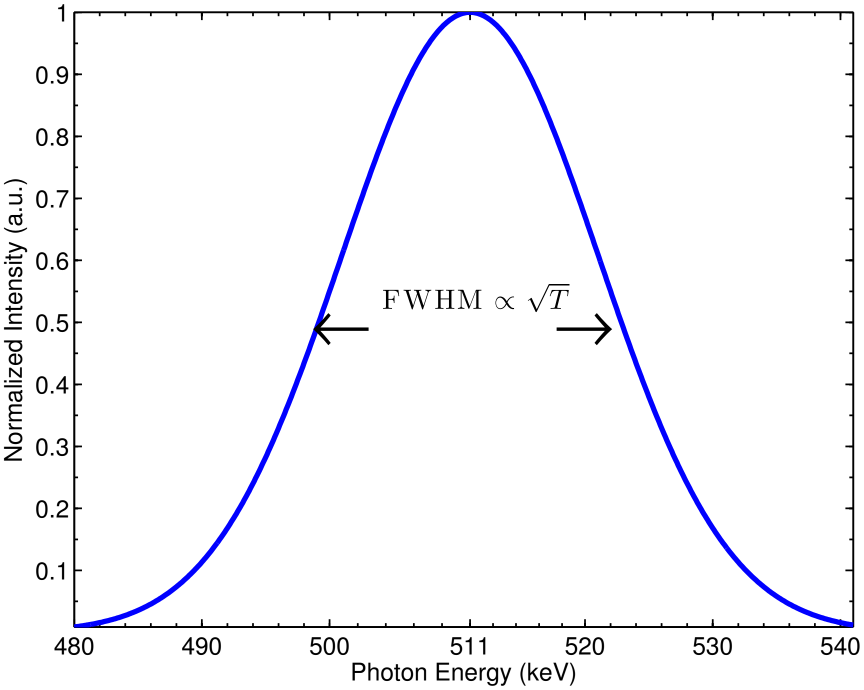

Figure B.1: Example Doppler broadening of direct annihilation of thermal positrons and electrons with a Maxwellian temperature of $100\text{eV} = 1.16\times10^6$ K. The full width at half maximum of the Gaussian distribution is related to the temperature of the bulk by Eq. (B.5).

FWHM is ∼20 keV. When thermalized, the annihilating radiation is emitted isotropically, where the maximum peak width is given by Eq. B.5. This analysis is done assuming in-flight annihilation, which depending on the densities and temperatures of the plasma, is the dominant annihilation mechanism. If the pairs first form positronium (and dependent on the singlet or triplet formation and whether charge exchange occurs, in which atomic electrons are involved), the resulting energy distribution is non-Maxwellian. These finer points should be considered depending on the intended platform for which annihilation radiation will be used as a diagnostic.

APPENDIX C

Uncertainty Propagation for EPPS data

Propagating error to the final electron spectrum is carried out in several steps. Uncertainty in the measured value of image plate was empirically determined by multiple large-area exposures of a uniform carbon-14 source. The standard deviation of the signal over a uniform area was found to scale as $R^2\sqrt{3S}$, where R is the scanner resolution and S is the measured signal in physical units of PSL [121].

The uncertainty is calculated by the generalized propagation of error for a function products and quotients, $q = (x \times \ldots \times z)/(u \times \ldots \times z)$, where

$$\frac{\delta q}{|q|} = \sqrt{\left(\frac{\delta x}{x}\right)^2 + \ldots + \left(\frac{\delta z}{z}\right)^2 + \left(\frac{\delta u}{u}\right)^2 + \ldots + \left(\frac{\delta w}{w}\right)^2}. \tag{C.1}$$

This form is appropriate to use for the EPPS since the terms are uncorrelated and relatively small. For the EPPS, we first find the uncertainty in each term where the functional form of the electron spectrum per unit energy per solid angle is

$$\frac{dN_i}{dE} = \frac{(D_i - BG_i)\Delta D_y}{(E_{i+1} - E_i) \times \Omega \times f(t) \times \Phi(E_i)} \tag{C.2}$$

where $D_i - BG_i$ is the background subtracted data of the ith pixel, E is the energy dispersion, Ω is the solid angle of the system, $f(t)$ is the time dependent fading factor of the image plate, Φ is the physical scanning unit PSL to number of electrons, and ΔD_y is the signal width in the non-dispersion direction.

The error associated with the dispersion curve is estimated to be 5%. Uncertainty in the geometric solid angle is a constant such that $\delta\Omega = \Omega\ [(\delta S_h/S_h)^2 + (\delta S_v/S_v)^2 + (\delta d/d)^2]^{1/2}$ where $S_{v,h}$ is the vertical and horizontal slit size and d is the distance between the electron source and slit. The image plate fading factor is an analytic function where the error is given by

$$\begin{aligned}
\delta f(t) &= \sqrt{\left(\frac{\partial f}{\partial y_0}\delta y_0\right)^2 + \left(\frac{\partial f}{\partial A_1}\delta A_1\right)^2 + \left(\frac{\partial f}{\partial \tau_1}\delta \tau_1\right)^2 + \left(\frac{\partial f}{\partial A_2}\delta A_2\right)^2 + \left(\frac{\partial f}{\partial \tau_2}\delta \tau_2\right)^2 + \left(\frac{\partial f}{\partial t}\delta t\right)^2} \\
&= \left[(\delta y_0)^2 + (\exp(-t/\tau_1)\delta A_1)^2 + \left(\frac{A_1}{\tau_1^2}\exp(-t/\tau_1)\delta\tau_1\right)^2 + (\exp(-t/\tau_2)\delta A_2)^2\right. \\
&\quad \left. + \left(\frac{A_2}{\tau_2^2}\exp(-t/\tau_2)\delta\tau_2\right)^2 + \left(\left\{-\frac{A_1}{\tau_1}\exp(-t/\tau_1) - \frac{A_2}{\tau_2}\exp(-t/\tau_2)\right\}\delta t\right)^2\right]^{1/2}, \qquad \text{(C.3)}
\end{aligned}$$

and the fading coefficients are given in Table 3.1.

The error associated with the conversion from PSL to number of electrons is given in Chen *et al.* [71] that also includes data from Tanaka et al. [70]. These datasets, and Monte Carlo simulations supporting their findings are summarized in Bonnet et al. [122].

Image plate data is recorded as 16-bit integers and converted to units of PSL through the following relation,

$$\mathrm{PSL} = \left(\frac{R_{\mu\mathrm{m}}}{100}\right)^2 \left(\frac{4000}{S}\right) 10^{L\left[G/(2^B-1)-0.5\right]}, \qquad \text{(C.4)}$$

where R is the pixel size in microns, S is the sensitivity setting, L is the latitude, B is the dynamic range, and G is the integer pixel value. Since the scanner uses a photon-counting photomultiplier tube, a counting statistics error estimate is used, where $\delta G = \sqrt{G}$. Propagating this uncertainty gives

$$\delta\mathrm{PSL} = \delta G \left|\frac{dPSL}{dG}\right| = \sqrt{G}\left(\frac{R_{\mu\mathrm{m}}}{100}\right)^2 \left(\frac{4000}{S}\right)\left(\frac{\ln 10}{2^B-1}\right) 10^{L\left[G/(2^B-1)-0.5\right]}, \qquad \text{(C.5)}$$

which is carried through to the measure of D_i and BG_i, where $\delta a_i = \sqrt{\delta D_i^2 + \delta BG_i^2}$.

APPENDIX D

EPPS Data Analysis Tool

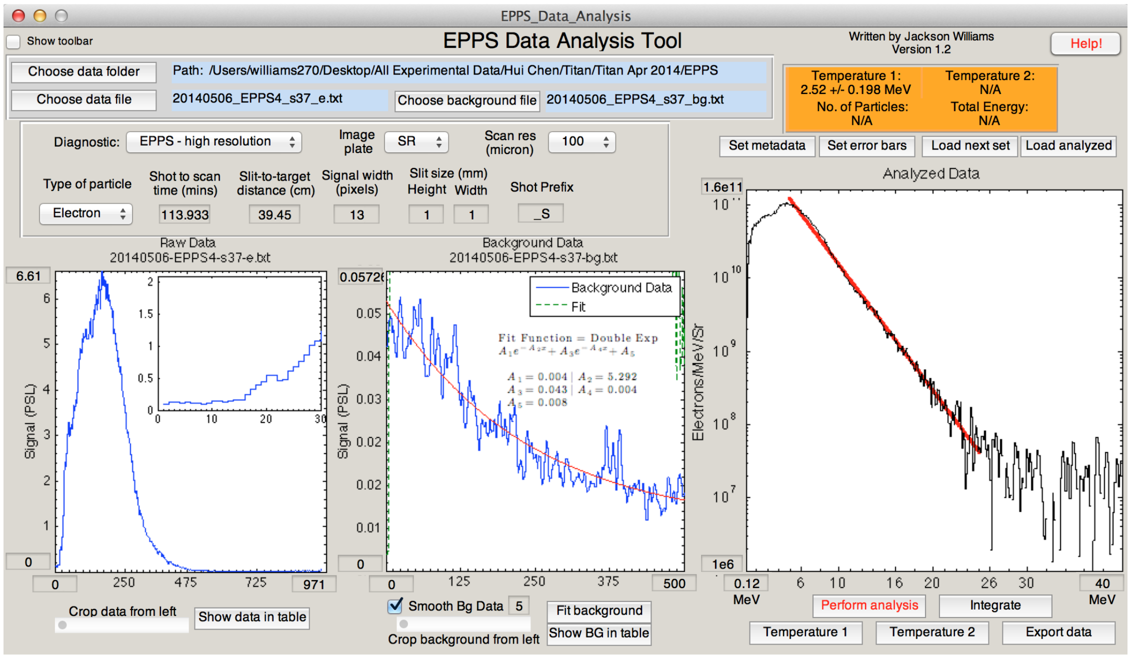

EPPS_Data_Analysis

EPPS Data Analysis Tool

Written by Jackson Williams
Version 1.2

Path: /Users/williams270/Desktop/All Experimental Data/Hui Chen/Titan/Titan Apr 2014/EPPS

20140506_EPPS4_s37_e.txt

20140506_EPPS4_s37_bg.txt

Temperature 1: 2.52 +/- 0.198 MeV

Temperature 2: N/A

No. of Particles: N/A

Total Energy: N/A

Diagnostic: EPPS - high resolution

Image plate: SR

Scan res (micron): 100

Type of particle: Electron

Shot to scan time (mins): 113.933

Slit-to-target distance (cm): 39.45

Signal width (pixels): 13

Slit size (mm) Height: 1

Slit size (mm) Width: 1

Shot Prefix: _S

☑ Smooth Bg Data: 5

Fit Function = Double Exp

$A_1e^{-A_2x}+A_3e^{-A_4x}+A_5$

$A_1=0.004 \mid A_2=5.292$

$A_3=0.043 \mid A_4=0.004$

$A_5=0.008$

☐ Show toolbar
Help!
Choose data folder
Choose data file
Choose background file
Set metadata
Set error bars
Load next set
Load analyzed
Raw Data
20140506-EPPS4-s37-e.txt
Background Data
20140506-EPPS4-s37-bg.txt
Analyzed Data
Signal (PSL)
6.61
6
5
4
3
2
1
0
0
250
475
725
971
2
1.5
1
0.5
0
0
10
20
30
0.05726
0.05
0.04
0.03
0.02
0.02
0.01
0
0
125
250
375
500
Background Data
Fit
Electrons/MeV/Sr
1.6e11
10^{11}
10^{10}
10^{9}
10^{8}
10^{7}
1e6
0.12 MeV
6
10
16
20
26
30
40 MeV
Crop data from left
Show data in table
Fit background
Show BG in table
Crop background from left
Perform analysis
Integrate
Temperature 1
Temperature 2
Export data

Figure D.1: Main GUI of EPPS Data Analysis Tool.

This guide describes how to use the EPPS Data Analysis Tool (EDAT). This Matlab GUI was designed to process batches of EPPS data and provide basic analysis information and currently supports only the analysis of electron and positron data from Dr. Hui Chen's EPPS-family of permanent magnet charged particle spectrometers. The EDAT needs several inputs:

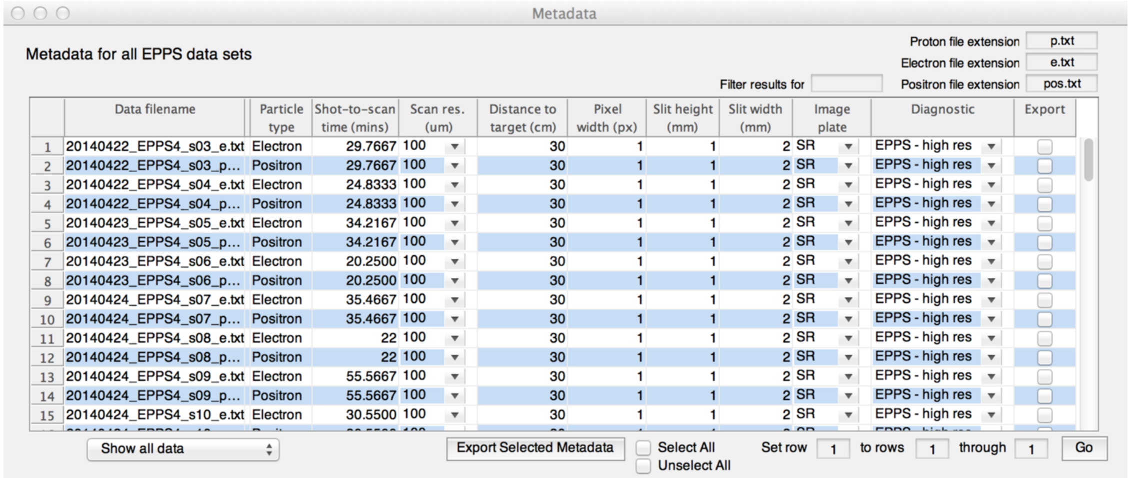

Metadata for all EPPS data sets

Proton file extension: p.txt
Electron file extension: e.txt
Positron file extension: pos.txt
Filter results for:

	Data filename	Particle type	Shot-to-scan time (mins)	Scan res. (um)	Distance to target (cm)	Pixel width (px)	Slit height (mm)	Slit width (mm)	Image plate	Diagnostic	Export
1	20140422_EPPS4_s03_e.txt	Electron	29.7667	100	30	1	1	2	SR	EPPS - high res	☐
2	20140422_EPPS4_s03_p...	Positron	29.7667	100	30	1	1	2	SR	EPPS - high res	☐
3	20140422_EPPS4_s04_e.txt	Electron	24.8333	100	30	1	1	2	SR	EPPS - high res	☐
4	20140422_EPPS4_s04_p...	Positron	24.8333	100	30	1	1	2	SR	EPPS - high res	☐
5	20140423_EPPS4_s05_e.txt	Electron	34.2167	100	30	1	1	2	SR	EPPS - high res	☐
6	20140423_EPPS4_s05_p...	Positron	34.2167	100	30	1	1	2	SR	EPPS - high res	☐
7	20140423_EPPS4_s06_e.txt	Electron	20.2500	100	30	1	1	2	SR	EPPS - high res	☐
8	20140423_EPPS4_s06_p...	Positron	20.2500	100	30	1	1	2	SR	EPPS - high res	☐
9	20140424_EPPS4_s07_e.txt	Electron	35.4667	100	30	1	1	2	SR	EPPS - high res	☐
10	20140424_EPPS4_s07_p...	Positron	35.4667	100	30	1	1	2	SR	EPPS - high res	☐
11	20140424_EPPS4_s08_e.txt	Electron	22	100	30	1	1	2	SR	EPPS - high res	☐
12	20140424_EPPS4_s08_p...	Positron	22	100	30	1	1	2	SR	EPPS - high res	☐
13	20140424_EPPS4_s09_e.txt	Electron	55.5667	100	30	1	1	2	SR	EPPS - high res	☐
14	20140424_EPPS4_s09_p...	Positron	55.5667	100	30	1	1	2	SR	EPPS - high res	☐
15	20140424_EPPS4_s10_e.txt	Electron	30.5500	100	30	1	1	2	SR	EPPS - high res	☐

Set row 1 to rows 1 through 1

Figure D.2: Metadata GUI of EPPS Data Analysis Tool.

1. Lineout of EPPS data (signal and background noise) in units of PSL
2. Geometric Setup
    (a) Distance between target and entrance slit
    (b) Entrance slit dimensions
    (c) Dispersion curve particle type
3. Image Plate Setup
    (a) Image plate type
    (b) Scanner resolution
    (c) Width of the signal
4. Time between exposure and scan

Items 2–4 on the above list are referred to here as the shot "metadata" and can be set as a batch using the "Set metadata" button (see Fig. D.1).

The Metadata GUI (see Fig. D.2) batch processes all available line outs. By highlighting the "Export" flag in the right-most column and clicking "Export Selected Metadata," a text file will be created that stores all the relevant metadata information. The shot-to-scan time will be calculated automatically, as will the scan resolution, from the available "filename.inf" image plate scan file. The diagnostic dispersion selection (e.g. "EPPS - high res") is important for the very low-energy and very high-energy signals since the dispersion for "E" and "P" is very similar for nominally 5-50 MeV.

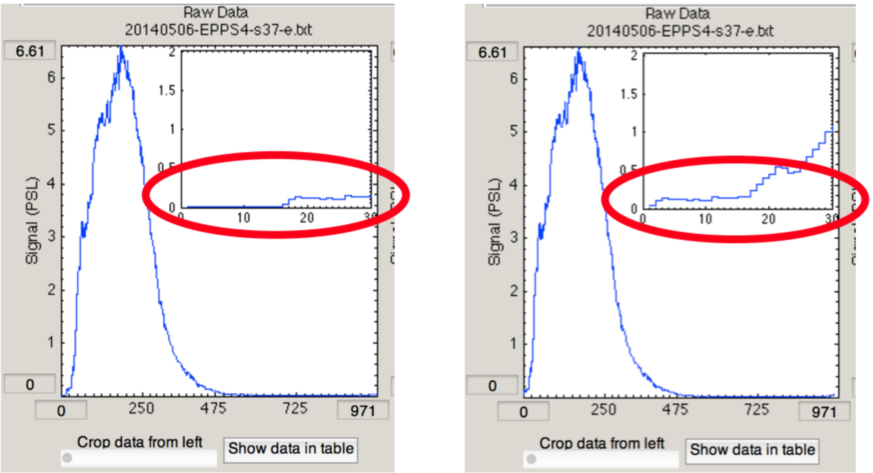
Raw Data
20140506-EPPS4-s37-e.txt
6.61
Signal (PSL)
0
250
475
725
971
Crop data from left
Show data in table
Raw Data
20140506-EPPS4-s37-e.txt
6.61
Signal (PSL)
0
250
475
725
971
Crop data from left
Show data in table

Figure D.3: Setting the front of the lineout is done by using the sliders at the bottom to remove any zero-signal pixels in the lineout.

Loading data and background lineouts is performed at the Main GUI. Once all prerequisites of use are met, lineouts can be loaded by:

1. Establishing the root directory for all lineout files (folder where lineouts are saved). *The lineout files must be included in the root directly set by the Main GUI.*
2. Clicking "Choose data file"

This will automatically load and scale the data file and background file, assuming the shot names are the same and only differ in the data file extension (_e.txt and _bg.txt). If these are different, the background will need to be added independently.

Adjusting data lineouts can be seen in Fig. D.3. It is not necessary at the lineout measurement to remove all zero-signal points. The sliders at the bottom of the "Raw Data" figure will adjust the zero-point of the lineout. The inset provides a zoomed-in view of the first 30 pixels. For the Data figure, only the left crop must be set, where the figures below show the uncropped (left) and cropped (right) data set.

The background lineout crop, shown in Fig. D.4 follows the signal crop, however, both the left and right edges must be set in order to perform a parameterized fit to the background data. The below set of figures shows the progression from the [1] original background lineout, [2] setting the left crop by omitting zero-point data, and [3] setting the right margin to the background-only region (region before the signal begins to climb again from influence of the

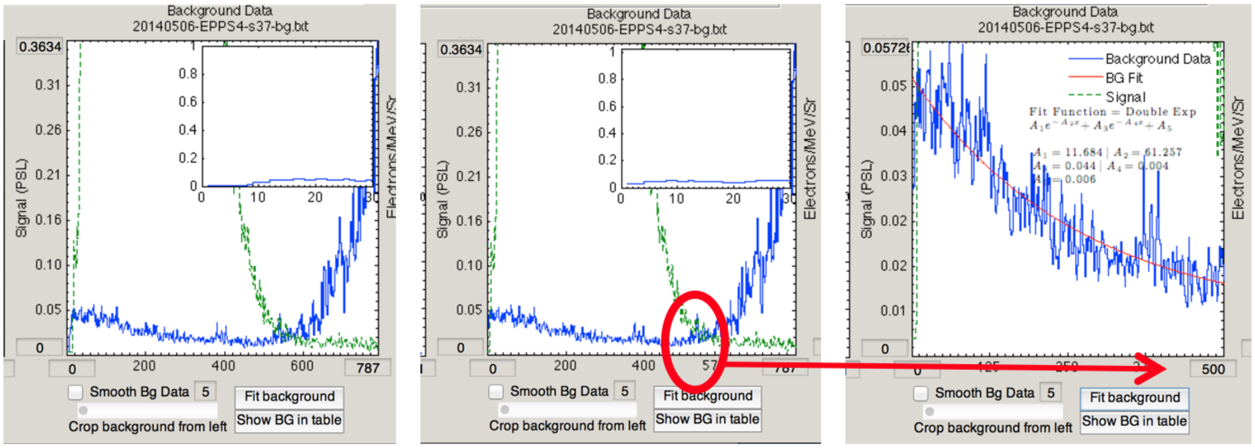
Background Data
20140506-EPPS4-s37-bg.txt
0.3634
0.31
0.26
0.21
0.16
0.10
0.05
0
Signal (PSL)
Electrons/MeV/Sr
0
200
400
600
787
Smooth Bg Data
5
Fit background
Show BG in table
Crop background from left
0.05726
0.05
0.04
0.03
0.02
0.01
500
Background Data
BG Fit
Signal
Fit Function = Double Exp
$A_1e^{-A_2x}+A_3e^{-A_4x}+A_5$
$A_1 = 11.684$ | $A_2 = 61.257$
$A_3 = 0.044$ | $A_4 = 0.004$
$A_5 = 0.006$

Figure D.4: Cropping the background lineouts removes the initial zero-signal points and crops the background to the point at which noise from the protons is evident.

protons) and fitting the data to a double-exponential profile. Options for the background fit include:

1. Fit for double-exponential profile with a constant vertical offset
2. Fit for double-exponential profile with a Gaussian superimposed
3. Fit for double-exponential profile without an offset
4. Setting background values to all zero
5. Using the unfitted background data
6. Setting a region of the background data to omit for the purposes of the fit functions
7. "Smooth BG Data" button, which sometimes is helpful with noisy data.

Before selecting Analyze Data, a double-check should be performed that includes:

1. Cropping both signal and background lineouts
2. Fitting background lineout if applicable
3. All shot metadata is correct

The beta version release of this software includes, at the time of this publication, a large list of options, buttons, and settings and following is an attempt to create a complete list:

1. "Set error bars" button — The error bars are meant to give a rough idea of the propagated uncertainty in the measurement. Use this only as a 'by-eye' view of the error where the confidence on the error values is not good enough to be cited in presenting the analysis or in publications.

2. “Load next set” button — This button works some of the time but is buggy, especially for non-standard naming conventions and sometimes for single-digit shot numbers (1-9). Use at your own risk.
3. Context Menus for Background Data Figure All functionality of the context menus on the BG data figure (right clicks options) should work, however, no guarantee is given that they will work on the first try. Use proper diligence: what you ask for is what you’re given.

BIBLIOGRAPHY

[1] A. V. Kulikov, S. D. Ecklund, and E. M. Reuter. SLC positron source pulsed flux concentrator. Technical Report SLAC-PUB-5473, Stanford Linear Accelerator Center, June 1991.

[2] T. E. Cowan, M. D. Perry, M. H. Key, T. R. Ditmire, S. P. Hatchett, E. A. Henry, J. D. Moody, M. J. Moran, D. M. Pennington, T. W. Phillips, T. C. Sangster, J. A. Sefcik, M. S. Singh, R. A. Snavely, M. A. Stoyer, S. C. Wilks, P. E. Young, Y. Takahashi, B. Dong, W. Fountain, T. Parnell, J. Johnson, A. W. Hunt, and T. Küml. High energy electrons, nuclear phenomena and heating in petawatt laser-solid experiments. *Laser Part. Beams*, 17(04):773–783, 1999. URL `http://dx.doi.org/10.1017/S0263034699174238`.

[3] C. Gahn, G. D. Tsakiris, G. Pretzler, K. J. Witte, C. Delfin, C.-G. Wahlström, and D. Habs. Generating positrons with femtosecond-laser pulses. *Appl. Phys. Lett.*, 77(17):2662–2664, 2000. doi: http://dx.doi.org/10.1063/1.1319526. URL `http://scitation.aip.org/content/aip/journal/apl/77/17/10.1063/1.1319526`.

[4] B. C. Stuart, J. D. Bonlie, J. A. Britten, J. A. Caird, R. Cross, C. A. Ebbers, M. J. Eckart, A. C. Erlandson, W. A. Molander, A. Ng, P. K. Patel, and D. F. Price. The Titan Laser at LLNL. In *Conference on Lasers and Electro-Optics/Quantum Electronics and Laser Science Conference and Photonic Applications Systems Technologies*, page JTuG3. Optical Society of America, 2006. URL `http://www.opticsinfobase.org/abstract.cfm?URI=CLEO-2006-JTuG3`.

[5] Hui Chen, S. C. Wilks, J. D. Bonlie, E. P. Liang, J. Myatt, D. F. Price, D. D. Meyerhofer, and P. Beiersdorfer. Relativistic positron creation using ultraintense short pulse lasers. *Phys. Rev. Lett.*, 102:105001, Mar 2009. doi: 10.1103/PhysRevLett.102.105001. URL `http://link.aps.org/doi/10.1103/PhysRevLett.102.105001`.

[6] L. J. Waxer, D. N. Maywar, J. H. Kelly, T. J. Kessler, B. E. Kruschwitz, S. J. Loucks, R. L. McCrory, D. D. Meyerhofer, S. F. B. Morse, C. Stoeckl, and J. D. Zuegel. High-energy petawatt capability for the Omega laser. *Opt. Photon. News*, 16(7):30–36, Jul 2005. doi: 10.1364/OPN.16.7.000030. URL `http://www.osa-opn.org/abstract.cfm?URI=opn-16-7-30`.

[7] Hui Chen, S. C. Wilks, D. D. Meyerhofer, J. Bonlie, C. D. Chen, S. N. Chen, C. Courtois, L. Elberson, G. Gregori, W. Kruer, O. Landoas, J. Mithen, J. Myatt, C. D. Murphy, P. Nilson, D. Price, M. Schneider, R. Shepherd, C. Stoeckl, M. Tabak, R. Tommasini, and P. Beiersdorfer. Relativistic quasimonoenergetic

positron jets from intense laser-solid interactions. *Phys. Rev. Lett.*, 105:015003, Jul 2010. doi: 10.1103/PhysRevLett.105.015003. URL `http://link.aps.org/doi/10.1103/PhysRevLett.105.015003`.

[8] Hui Chen, J. C. Sheppard, D. D. Meyerhofer, A. Hazi, A. Link, S. Anderson, H. A. Baldis, R. Fedosejev, J. Gronberg, N. Izumi, S. Kerr, E. Marley, J. Park, R. Tommasini, S. Wilks, and G. J. Williams. Emittance of positron beams produced in intense laser plasma interaction. *Phys. Plasmas*, 20(1):013111, 2013. doi: 10.1063/1.4789621. URL `http://link.aip.org/link/?PHP/20/013111/1`.

[9] Hui Chen, D. Meyerhofer, S. Wilks, R. Cauble, F. Dollar, K. Falk, G. Gregori, A. Hazi, E. Moses, C. Murphy, J. Myatt, J. Park, J. Seely, R. Shepherd, A. Spitkovsky, C. Stoeckl, C. Szabo, R. Tommasini, C. Zulick, and P. Beiersdorfer. Towards laboratory produced relativistic electron–positron pair plasmas. *High Energy Density Phys.*, 7(4):225 – 229, 2011. ISSN 1574-1818. doi: 10.1016/j.hedp.2011.05.006. URL `http://www.sciencedirect.com/science/article/pii/S1574181811000577`.

[10] Hui Chen, F. Fiuza, A. Link, A. Hazi, M. Hill, D. Hoarty, S. James, S. Kerr, D. D. Meyerhofer, J. Myatt, J. Park, Y. Sentoku, and G. J. Williams. Scaling the yield of laser-driven electron-positron jets to laboratory astrophysical applications. *Phys. Rev. Lett.*, 114:215001, May 2015. doi: 10.1103/PhysRevLett.114.215001. URL `http://link.aps.org/doi/10.1103/PhysRevLett.114.215001`.

[11] H. Shiraga, N. Miyanaga, J. Kawanaka, S. Tokita, T. Jitsuno, Y. Nakata, S. Fujioka, and H. Azechi. World's largest high energy petawatt laser LFEX as a user's facility. *Proc. SPIE*, 9515:95150S–95150S–6, 2015. doi: 10.1117/12.2181654. URL `http://dx.doi.org/10.1117/12.2181654`.

[12] A. S. Wan, J. Bromage, P. Datte, C. Dorrer, B. Dzenitis, E. Gaul, R. Johnson, N. Landen, and B. Stuart. Report on high-contrast advanced radiographic capability review. Technical Report LLNL-TR-665139, Lawrence Livermore National Laboratory (LLNL), Livermore, CA, 2014.

[13] G. Sarri, W. Schumaker, A. Di Piazza, M. Vargas, B. Dromey, M. E. Dieckmann, V. Chvykov, A. Maksimchuk, V. Yanovsky, Z. H. He, B. X. Hou, J. A. Nees, A. G. R. Thomas, C. H. Keitel, M. Zepf, and K. Krushelnick. Table-top laser-based source of femtosecond, collimated, ultrarelativistic positron beams. *Phys. Rev. Lett.*, 110:255002, Jun 2013. doi: 10.1103/PhysRevLett.110.255002. URL `http://link.aps.org/doi/10.1103/PhysRevLett.110.255002`.

[14] G. Sarri, K. Poder, J. M. Cole, W. Schumaker, A. Di Piazza, B. Reville, T. Dzelzainis, D. Doria, L. A. Gizzi, G. Grittani, S. Kar, C. H. Keitel, K. Krushelnick, S. Kuschel, S. P. D. Mangles, Z. Najmudin, N. Shukla, L. O. Silva, D. Symes, A. G. R. Thomas, M. Vargas, J. Vieira, and M. Zepf. Generation of neutral and high-density electron-positron pair plasmas in the laboratory. *Nat. Commun.*, 6, 04 2015. URL `http://dx.doi.org/10.1038/ncomms7747`.

[15] G. J. Williams, B. B. Pollock, F. Albert, J. Park, and Hui Chen. Positron generation using laser-wakefield electron sources. *Phys. Plasmas*, 22(9):093115, 2015. doi: http://dx.doi.org/10.1063/1.4931044. URL `http://scitation.aip.org/content/aip/journal/pop/22/9/10.1063/1.4931044`.

[16] Hui Chen, G. Fiksel, D. Barnak, P.-Y. Chang, R. F. Heeter, A. Link, and D. D. Meyerhofer. Magnetic collimation of relativistic positrons and electrons from high intensity laser–matter interactions. *Phys. Plasmas*, 21(4):040703, 2014. doi: http://dx.doi.org/10.1063/1.4873711. URL `http://scitation.aip.org/content/aip/journal/pop/21/4/10.1063/1.4873711`.

[17] Hui Chen, R. Tommasini, J. Seely, C. I. Szabo, U. Feldman, N. Pereira, G. Gregori, K. Falk, J. Mithen, and C. D. Murphy. Measuring electron-positron annihilation radiation from laser plasma interactions. *Rev. Sci. Instrum.*, 83(10), 2012. doi: http://dx.doi.org/10.1063/1.4734038. URL `http://scitation.aip.org/content/aip/journal/rsi/83/10/10.1063/1.4734038`.

[18] D. H. Perkins. *Introduction to High Energy Physics*. Addison Wesley, 3rd edition, 1987.

[19] D. J. Griffiths. *Introduction to quantum mechanics*. Pearson Education India, 2005.

[20] J. J. Sakurai. *Modern Quantum Mechanics, Revised Edition*. Addison Wesley, 1994.

[21] A. Sommerfeld. Über die beugung und bremsung der elektronen. *Annalen der Physik*, 403(3):257–330, 1931.

[22] H. A. Bethe and L. C. Maximon. Theory of bremsstrahlung and pair production. I. differential cross section. *Phys. Rev.*, 93:768–784, Feb 1954. doi: 10.1103/PhysRev.93.768. URL `http://link.aps.org/doi/10.1103/PhysRev.93.768`.

[23] H. W. Koch and J. W. Motz. Bremsstrahlung cross-section formulas and related data. *Rev. Mod. Phys.*, 31:920–955, Oct 1959. doi: 10.1103/RevModPhys.31.920. URL `http://link.aps.org/doi/10.1103/RevModPhys.31.920`.

[24] L. I. Schiff. Energy-angle distribution of thin target bremsstrahlung. *Phys. Rev.*, 83:252–253, Jul 1951. doi: 10.1103/PhysRev.83.252. URL `http://link.aps.org/doi/10.1103/PhysRev.83.252`.

[25] J. D. Jackson. *Classical electrodynamics*, volume 3. Wiley New York, 1962.

[26] J. W. Motz, H. A. Olsen, and H. W. Koch. Pair production by photons. *Rev. Mod. Phys.*, 41:581–639, Oct 1969. doi: 10.1103/RevModPhys.41.581. URL `http://link.aps.org/doi/10.1103/RevModPhys.41.581`.

[27] J. Joseph and F. Rohrlich. Pair production and bremsstrahlung in the field of free and bound electrons. *Rev. Mod. Phys.*, 30:354–368, Apr 1958. doi: 10.1103/RevModPhys.30.354. URL `http://link.aps.org/doi/10.1103/RevModPhys.30.354`.

[28] Y. S. Tsai and V. Whitis. Thick-target bremsstrahlung and target considerations for secondary-particle production by electrons. *Phys. Rev.*, 149:1248–1257, Sep 1966. doi: 10.1103/PhysRev.149.1248. URL `http://link.aps.org/doi/10.1103/PhysRev.149.1248`.

[29] Y.-S. Tsai. Pair production and bremsstrahlung of charged leptons. *Rev. Mod. Phys.*, 46:815–851, Oct 1974. doi: 10.1103/RevModPhys.46.815. URL `http://link.aps.org/doi/10.1103/RevModPhys.46.815`.

[30] K. Olive and P. D. Group. Review of particle physics. *Chin. Phys. C*, 38(9):090001, 2014. URL `http://stacks.iop.org/1674-1137/38/i=9/a=090001`.

[31] H. J. Bhabha. The creation of electron pairs by fast charged particles. *Proc. R. Soc. London, Ser. A*, 152(877):559–586, 1935.

[32] D. A. Gryaznykh. Cross section for the production of electron-positron pairs by electrons in the field of a nucleus. *Phys. At. Nucl.*, 61:394–399, Mar. 1998.

[33] D. Gryaznykh, Y. Kandiev, and V. Lykov. Estimates of electron-positron pair production in the interaction of high-power laser radiation with high-Z targets. *JETP Lett.*, 67:257–262, 1998. ISSN 0021-3640. URL `http://dx.doi.org/10.1134/1.567660`. 10.1134/1.567660.

[34] K. Nakashima and H. Takabe. Numerical study of pair creation by ultraintense lasers. *Phys. Plasmas*, 9:1505–1512, 2002.

[35] P. Gibbon. *Short pulse laser interactions with matter.* Imperial College Press London, 2005.

[36] W. L. Kruer and K. Estabrook. $J \times B$ heating by very intense laser light. *Phys. Fluids*, 28:430, 1985.

[37] S. C. Wilks, W. L. Kruer, M. Tabak, and A. B. Langdon. Absorption of ultra-intense laser pulses. *Phys. Rev. Lett.*, 69(9):1383–1386, 1992.

[38] S. Wilks and W. Kruer. Absorption of ultrashort, ultra-intense laser light by solids and overdense plasmas. *IEEE. J. Quantum Electron.*, 33(11):1954–1968, 1997.

[39] A. Pukhov, Z.-M. Sheng, and J. Meyer-ter Vehn. Particle acceleration in relativistic laser channels. *Phys. Plasmas*, 6(7):2847–2854, 1999. doi: http://dx.doi.org/10.1063/1.873242. URL `http://scitation.aip.org/content/aip/journal/pop/6/7/10.1063/1.873242`.

[40] T. Tajima and J. M. Dawson. Laser electron accelerator. *Phys. Rev. Lett.*, 43:267–270, Jul 1979. doi: 10.1103/PhysRevLett.43.267. URL `http://link.aps.org/doi/10.1103/PhysRevLett.43.267`.

[41] A. Pak, K. A. Marsh, S. F. Martins, W. Lu, W. B. Mori, and C. Joshi. Injection and trapping of tunnel-ionized electrons into laser-produced wakes. *Phys. Rev. Lett.*, 104: 025003, Jan 2010. doi: 10.1103/PhysRevLett.104.025003. URL `http://link.aps.org/doi/10.1103/PhysRevLett.104.025003`.

[42] E. Esarey, P. Sprangle, J. Krall, and A. Ting. Overview of plasma-based accelerator concepts. *IEEE Trans. Plasma Sci.*, 24(2):252–288, Apr 1996. ISSN 0093-3813. doi: 10.1109/27.509991.

[43] W. Lu, M. Tzoufras, C. Joshi, F. Tsung, W. Mori, J. Vieira, R. Fonseca, and L. Silva. Generating multi-gev electron bunches using single stage laser wakefield acceleration in a 3d nonlinear regime. *Phys. Rev. ST Accel. Beams*, 10:061301, Jun 2007. doi: 10.1103/PhysRevSTAB.10.061301. URL `http://link.aps.org/doi/10.1103/PhysRevSTAB.10.061301`.

[44] C. D. Decker, W. B. Mori, K. Tzeng, and T. Katsouleas. The evolution of ultra-intense, shortpulse lasers in underdense plasmas. *Phys. Plasmas*, 3(5):2047–2056, 1996. doi: http://dx.doi.org/10.1063/1.872001.

[45] J. E. Ralph, C. E. Clayton, F. Albert, B. B. Pollock, S. F. Martins, A. E. Pak, K. A. Marsh, J. L. Shaw, A. Till, J. P. Palastro, W. Lu, S. H. Glenzer, L. O. Silva, W. B. Mori, C. Joshi, and D. H. Froula. Laser wakefield acceleration at reduced density in the self-guided regime. *Phys. Plasmas*, 17(5):056709, 2010. doi: http://dx.doi.org/10.1063/1.3323083. URL `http://scitation.aip.org/content/aip/journal/pop/17/5/10.1063/1.3323083`.

[46] B. B. Pollock, C. E. Clayton, J. E. Ralph, F. Albert, A. Davidson, L. Divol, C. Filip, S. H. Glenzer, K. Herpoldt, W. Lu, K. A. Marsh, J. Meinecke, W. B. Mori, A. Pak, T. C. Rensink, J. S. Ross, J. Shaw, G. R. Tynan, C. Joshi, and D. H. Froula. Demonstration of a narrow energy spread, ∼0.5 GeV electron beam from a two-stage laser wakefield accelerator. *Phys. Rev. Lett.*, 107:045001, Jul 2011. doi: 10.1103/PhysRevLett.107.045001. URL `http://link.aps.org/doi/10.1103/PhysRevLett.107.045001`.

[47] B. B. Pollock. *Energy spread reduction of electron beams produced via laser wakefield acceleration.* PhD thesis, University of California, San Diego, 2012. URL `http://www.escholarship.org/uc/item/99r7c5w0`.

[48] ICRU. Radiation dosimetry: Electron beams with energies between 1 and 50 MeV. *Report 35, Bethesda, MD*, 1984.

[49] M. J. Berger, J. S. Coursey, M. A. Zucker, and J. Chang. Stopping-power and range tables for electrons, protons and helium ions, ESTAR database, NIST Physical Measurement Laboratory., 2005. URL `http://www.nist.gov/pml/data/star/index.cfm`.

[50] S. M. Seltzer and M. J. Berger. Evaluation of the collision stopping power of elements and compounds for electrons and positrons. *Int. J. Appl. Radiat. Isot.*, 33(11):1189 –

1218, 1982. ISSN 0020-708X. doi: http://dx.doi.org/10.1016/0020-708X(82)90244-7. URL `http://www.sciencedirect.com/science/article/pii/0020708X82902447`.

[51] L. Kim, R. H. Pratt, S. M. Seltzer, and M. J. Berger. Ratio of positron to electron bremsstrahlung energy loss: An approximate scaling law. *Phys. Rev. A*, 33:3002–3009, May 1986. doi: 10.1103/PhysRevA.33.3002. URL `http://link.aps.org/doi/10.1103/PhysRevA.33.3002`.

[52] M. J. Berger, J. H. Hubbell, S. M. Seltzer, J. Chang, J. S. Coursey, R. Sukumar, D. S. Zucker, and K. Olsen. XCOM: Photon cross sections database. *NIST Standard reference database*, 8:87–3597, 1998.

[53] W. Heitler. *The quantum theory of radiation*. Oxford University Press, 3rd edition, 1954.

[54] S. Agostinelli, J. Allison, K. Amako, J. Apostolakis, H. Araujo, P. Arce, M. Asai, D. Axen, S. Banerjee, G. Barrand, F. Behner, L. Bellagamba, J. Boudreau, L. Broglia, A. Brunengo, H. Burkhardt, S. Chauvie, J. Chuma, R. Chytracek, G. Cooperman, G. Cosmo, P. Degtyarenko, A. Dell'Acqua, G. Depaola, D. Dietrich, R. Enami, A. Feliciello, C. Ferguson, H. Fesefeldt, G. Folger, F. Foppiano, A. Forti, S. Garelli, S. Giani, R. Giannitrapani, D. Gibin, J. G. Cadenas, I. Gonzalez, G. G. Abril, G. Greeniaus, W. Greiner, V. Grichine, A. Grossheim, S. Guatelli, P. Gumplinger, R. Hamatsu, K. Hashimoto, H. Hasui, A. Heikkinen, A. Howard, V. Ivanchenko, A. Johnson, F. Jones, J. Kallenbach, N. Kanaya, M. Kawabata, Y. Kawabata, M. Kawaguti, S. Kelner, P. Kent, A. Kimura, T. Kodama, R. Kokoulin, M. Kossov, H. Kurashige, E. Lamanna, T. Lampan, V. Lara, V. Lefebure, F. Lei, M. Liendl, W. Lockman, F. Longo, S. Magni, M. Maire, E. Medernach, K. Minamimoto, P. M. de Freitas, Y. Morita, K. Murakami, M. Nagamatu, R. Nartallo, P. Nieminen, T. Nishimura, K. Ohtsubo, M. Okamura, S. O'Neale, Y. Oohata, K. Paech, J. Perl, A. Pfeiffer, M. Pia, F. Ranjard, A. Rybin, S. Sadilov, E. D. Salvo, G. Santin, T. Sasaki, N. Savvas, Y. Sawada, S. Scherer, S. Sei, V. Sirotenko, D. Smith, N. Starkov, H. Stoecker, J. Sulkimo, M. Takahata, S. Tanaka, E. Tcherniaev, E. S. Tehrani, M. Tropeano, P. Truscott, H. Uno, L. Urban, P. Urban, M. Verderi, A. Walkden, W. Wander, H. Weber, J. Wellisch, T. Wenaus, D. Williams, D. Wright, T. Yamada, H. Yoshida, and D. Zschiesche. Geant4 – a simulation toolkit. *Nucl. Instrum. Methods Phys. Res., Sect. A*, 506 (3):250 – 303, 2003. ISSN 0168-9002. doi: 10.1016/S0168-9002(03)01368-8. URL `http://www.sciencedirect.com/science/article/pii/S0168900203013688`.

[55] J. Allison, K. Amako, J. Apostolakis, H. Araujo, P. Dubois, M. Asai, G. Barrand, R. Capra, S. Chauvie, R. Chytracek, G. Cirrone, G. Cooperman, G. Cosmo, G. Cuttone, G. Daquino, M. Donszelmann, M. Dressel, G. Folger, F. Foppiano, J. Generowicz, V. Grichine, S. Guatelli, P. Gumplinger, A. Heikkinen, I. Hrivnacova, A. Howard, S. Incerti, V. Ivanchenko, T. Johnson, F. Jones, T. Koi, R. Kokoulin, M. Kossov, H. Kurashige, V. Lara, S. Larsson, F. Lei, O. Link, F. Longo, M. Maire, A. Mantero, B. Mascialino, I. McLaren, P. Lorenzo, K. Minamimoto, K. Murakami, P. Nieminen, L. Pandola, S. Parlati, L. Peralta, J. Perl, A. Pfeiffer, M. Pia, A. Ribon, P. Rodrigues, G. Russo, S. Sadilov, G. Santin, T. Sasaki, D. Smith, N. Starkov, S. Tanaka,

E. Tcherniaev, B. Tome, A. Trindade, P. Truscott, L. Urban, M. Verderi, A. Walkden, J. Wellisch, D. Williams, D. Wright, and H. Yoshida. Geant4 developments and applications. *IEEE Trans. Nucl. Sci.*, 53(1):270 –278, feb. 2006. ISSN 0018-9499. doi: 10.1109/TNS.2006.869826.

[56] K. Amako, S. Guatelli, V. N. Ivanchenko, M. Maire, B. Mascialino, K. Murakami, P. Nieminen, L. Pandola, S. Parlati, M. G. Pia, et al. Comparison of Geant4 electromagnetic physics models against the NIST reference data. *IEEE Trans. Nucl. Sci.*, 52 (4):910–918, 2005.

[57] K. Amako, S. Guatelli, V. Ivanchencko, M. Maire, B. Mascialino, K. Murakami, L. Pandola, S. Parlati, M. Pia, M. Piergentili, T. Sasaki, and L. Urban. Geant4 and its validation. *Nucl. Phys. B*, 150:44 – 49, 2006. ISSN 0920-5632. doi: http://dx.doi.org/10.1016/j.nuclphysbps.2004.10.083. URL `http://www.sciencedirect.com/science/article/pii/S0920563205008066`. Proceedings of the 9th Topical Seminar on Innovative Particle and Radiation DetectorsProceedings of the 9th Topical Seminar on Innovative Particle and Radiation Detectors.

[58] G. Collaboration. *Geant4 Physics Reference Manual*, Geant4 10.0 edition, December 2013.

[59] Y. Ping, R. Shepherd, B. F. Lasinski, M. Tabak, H. Chen, H. K. Chung, K. B. Fournier, S. B. Hansen, A. Kemp, D. A. Liedahl, K. Widmann, S. C. Wilks, W. Rozmus, and M. Sherlock. Absorption of short laser pulses on solid targets in the ultrarelativistic regime. *Phys. Rev. Lett.*, 100:085004, Feb 2008. doi: 10.1103/PhysRevLett.100.085004. URL `http://link.aps.org/doi/10.1103/PhysRevLett.100.085004`.

[60] S. C. Wilks, A. B. Langdon, T. E. Cowan, M. Roth, M. Singh, S. Hatchett, M. H. Key, D. Pennington, A. MacKinnon, and R. A. Snavely. Energetic proton generation in ultra-intense laser–solid interactions. *Phys. Plasmas*, 8(2):542–549, 2001. doi: http://dx.doi.org/10.1063/1.1333697. URL `http://scitation.aip.org/content/aip/journal/pop/8/2/10.1063/1.1333697`.

[61] S. P. Hatchett, C. G. Brown, T. E. Cowan, E. A. Henry, J. S. Johnson, M. H. Key, J. A. Koch, A. B. Langdon, B. F. Lasinski, R. W. Lee, A. J. Mackinnon, D. M. Pennington, M. D. Perry, T. W. Phillips, M. Roth, T. C. Sangster, M. S. Singh, R. A. Snavely, M. A. Stoyer, S. C. Wilks, and K. Yasuike. Electron, photon, and ion beams from the relativistic interaction of petawatt laser pulses with solid targets. *Phys. Plasmas*, 7(5):2076–2082, 2000. doi: http://dx.doi.org/10.1063/1.874030. URL `http://scitation.aip.org/content/aip/journal/pop/7/5/10.1063/1.874030`.

[62] R. A. Snavely, M. H. Key, S. P. Hatchett, T. E. Cowan, M. Roth, T. W. Phillips, M. A. Stoyer, E. A. Henry, T. C. Sangster, M. S. Singh, S. C. Wilks, A. MacKinnon, A. Offenberger, D. M. Pennington, K. Yasuike, A. B. Langdon, B. F. Lasinski, J. Johnson, M. D. Perry, and E. M. Campbell. Intense high-energy proton beams from petawatt-laser irradiation of solids. *Phys. Rev. Lett.*, 85:2945–2948, Oct 2000. doi: 10.1103/PhysRevLett.85.2945. URL `http://link.aps.org/doi/10.1103/PhysRevLett.85.2945`.

[63] Hui Chen, A. Link, Y. Sentoku, P. Audebert, F. Fiuza, A. Hazi, R. F. Heeter, M. Hill, L. Hobbs, A. J. Kemp, G. E. Kemp, S. Kerr, D. D. Meyerhofer, J. Myatt, S. R. Nagel, J. Park, R. Tommasini, and G. J. Williams. The scaling of electron and positron generation in intense laser-solid interactions. *Phys. Plasmas*, 22(5):056705, 2015. doi: http://dx.doi.org/10.1063/1.4921147. URL `http://scitation.aip.org/content/aip/journal/pop/22/5/10.1063/1.4921147`.

[64] A. Link, R. R. Freeman, D. W. Schumacher, and L. D. Van Woerkom. Effects of target charging and ion emission on the energy spectrum of emitted electrons. *Phys. Plasmas*, 18(5):053107, 2011. doi: http://dx.doi.org/10.1063/1.3587123. URL `http://scitation.aip.org/content/aip/journal/pop/18/5/10.1063/1.3587123`.

[65] D. Strickland and G. Mourou. Compression of amplified chirped optical pulses. *Opt. Commun.*, 55(6):447–449, 1985. ISSN 0030-4018. doi: http://dx.doi.org/10.1016/0030-4018(85)90151-8. URL `http://www.sciencedirect.com/science/article/pii/0030401885901518`.

[66] M. Sonoda, M. Takano, J. Miyahara, and H. Kato. Computed radiography utilizing scanning laser stimulated luminescence. *Radiology*, 148(3):833–838, 1983. URL `http://radiology.rsna.org/content/148/3/833.abstract`.

[67] T. Noikura, S. Suenaga, T. Sato, K. Kawano, M. Fujimura, Y. Morita, and Y. Iwashita. Digital images with fuji computed radiography (FCR) in dento-maxillo-facial radiology. *Oral Radiology*, 1:1–9, 1985. ISSN 0911-6028. doi: 10.1007/BF02350163. URL `http://dx.doi.org/10.1007/BF02350163`.

[68] J. Miyahara, K. Takahashi, Y. Amemiya, N. Kamiya, and Y. Satow. A new type of x-ray area detector utilizing laser stimulated luminescence. *Nucl. Instrum. Methods Phys. Res., Sect. A*, 246(1-3):572 – 578, 1986. ISSN 0168-9002. doi: 10.1016/0168-9002(86)90156-7. URL `http://www.sciencedirect.com/science/article/pii/0168900286901567`.

[69] Y. Amemiya and J. Miyahara. Imaging plate illuminates many fields. *Nature*, 336 (6194):89–90, 11 1988. URL `http://dx.doi.org/10.1038/336089a0`.

[70] K. A. Tanaka, T. Yabuuchi, T. Sato, R. Kodama, Y. Kitagawa, T. Takahashi, T. Ikeda, Y. Honda, and S. Okuda. Calibration of imaging plate for high energy electron spectrometer. *Rev. Sci. Instrum.*, 76(1):013507, 2005. doi: 10.1063/1.1824371. URL `http://link.aip.org/link/?RSI/76/013507/1`.

[71] Hui Chen, N. L. Back, T. Bartal, F. N. Beg, D. C. Eder, A. J. Link, A. G. MacPhee, Y. Ping, P. M. Song, A. Throop, and L. V. Woerkom. Absolute calibration of image plates for electrons at energy between 100 keV and 4 MeV. *Rev. Sci. Instrum.*, 79(3):033301, 2008. doi: 10.1063/1.2885045. URL `http://link.aip.org/link/?RSI/79/033301/1`.

[72] G. Boutoux, N. Rabhi, D. Batani, A. Binet, J.-E. Ducret, K. Jakubowska, J.-P. Nègre, C. Reverdin, and I. Thfoin. Study of imaging plate detector sensitivity to 5-18 MeV

electrons. *Rev. Sci. Instrum.*, 86(11):113304, 2015. doi: http://dx.doi.org/10.1063/1.4936141. URL `http://scitation.aip.org/content/aip/journal/rsi/86/11/10.1063/1.4936141`.

[73] A. Mančić, J. Fuchs, P. Antici, S. A. Gaillard, and P. Audebert. Absolute calibration of photostimulable image plate detectors used as (0.5–20 MeV) high-energy proton detectors. *Rev. Sci. Instrum.*, 79(7):073301, 2008. doi: 10.1063/1.2949388. URL `http://link.aip.org/link/?RSI/79/073301/1`.

[74] S. G. Gales and C. D. Bentley. Image plates as x-ray detectors in plasma physics experiments. *Rev. Sci. Instrum.*, 75(10):4001–4003, 2004. doi: 10.1063/1.1789256. URL `http://link.aip.org/link/?RSI/75/4001/1`.

[75] N. Izumi, R. Snavely, G. Gregori, J. A. Koch, H.-S. Park, and B. A. Remington. Application of imaging plates to x-ray imaging and spectroscopy in laser plasma experiments (invited). *Rev. Sci. Instrum.*, 77(10):10E325, 2006. doi: 10.1063/1.2351924. URL `http://link.aip.org/link/?RSI/77/10E325/1`.

[76] A. L. Meadowcroft, C. D. Bentley, and E. N. Stott. Evaluation of the sensitivity and fading characteristics of an image plate system for x-ray diagnostics. *Rev. Sci. Instrum.*, 79(11):113102, 2008. doi: 10.1063/1.3013123. URL `http://link.aip.org/link/?RSI/79/113102/1`.

[77] B. R. Maddox, H. S. Park, B. A. Remington, N. Izumi, S. Chen, C. Chen, G. Kimminau, Z. Ali, M. J. Haugh, and Q. Ma. High-energy x-ray backlighter spectrum measurements using calibrated image plates. *Rev. Sci. Instrum.*, 82(2):023111, 2011. doi: 10.1063/1.3531979. URL `http://link.aip.org/link/?RSI/82/023111/1`.

[78] N. Izumi, J. Lee, E. Romano, G. Stone, B. Maddox, T. Ma, V. Rekow, D. K. Bradley, and P. Bell. X-ray and neutron sensitivity of imaging plates. *Proc. SPIE*, 8850:885006–885006–8, 2013. doi: 10.1117/12.2024513. URL `http://dx.doi.org/10.1117/12.2024513`.

[79] G. J. Williams, B. R. Maddox, Hui Chen, S. Kojima, and M. Millecchia. Calibration and equivalency analysis of image plate scanners. *Rev. Sci. Instrum.*, 85(11):11E604, 2014. doi: http://dx.doi.org/10.1063/1.4886390. URL `http://scitation.aip.org/content/aip/journal/rsi/85/11/10.1063/1.4886390`.

[80] *Typhoon^{TM} FLA 7000 Control Software User Manual 28-9607-63 AA*. GE Healthcare Bio-Sciences, Oct 2009. URL `https://www.gelifesciences.com/gehcls_images/GELS/Related%20Content/Files/1314787424814/litdoc28960762AB_20110831145107.pdf`.

[81] *American Radiolabeled Chemicals, Inc.*, 2009. `http://http://www.arc-inc.com/` [Accessed: 12 January 2016].

[82] Cauchois, Y. Spectrographie des rayons x-par transmission d'un faisceau non canalisé à travers un cristal courbé - I. *J. Phys. Radium*, 3(7):320–336, 1932. doi:

10.1051/jphysrad:0193200307032000. URL `http://dx.doi.org/10.1051/jphysrad:0193200307032000`.

[83] J. F. Seely, L. T. Hudson, G. E. Holland, and A. Henins. Enhanced x-ray resolving power achieved behind the focal circles of cauchois spectrometers. *Appl. Opt.*, 47 (15):2767–2778, May 2008. doi: 10.1364/AO.47.002767. URL `http://ao.osa.org/abstract.cfm?URI=ao-47-15-2767`.

[84] R. Nolte, R. Behrens, M. Schnürer, A. Rousse, and P. Ambrosi. A tld-based few-channel spectrometer for x ray fields with high fluence rates. *Radiat. Prot. Dosim.*, 84(1-4):367–370, 1999. URL `http://rpd.oxfordjournals.org/content/84/1-4/367.abstract`.

[85] P. A. Norreys, F. N. Beg, Y. Sentoku, L. O. Silva, R. A. Smith, and R. Trines. Intense laser-plasma interactions: New frontiers in high energy density physics. *Phys. Plasmas*, 16:041002, 2009.

[86] R. H. H. Scott, E. L. Clark, F. Perez, M. J. V. Streeter, J. R. Davies, H.-P. Schlenvoigt, J. J. Santos, S. Hulin, K. L. Lancaster, S. D. Baton, S. J. Rose, and P. A. Norreys. Measuring fast electron spectra and laser absorption in relativistic laser-solid interactions using differential bremsstrahlung photon detectors. *Rev. Sci. Instrum.*, 84(8):083505, 2013. doi: http://dx.doi.org/10.1063/1.4816332. URL `http://scitation.aip.org/content/aip/journal/rsi/84/8/10.1063/1.4816332`.

[87] C. D. Chen, J. A. King, M. H. Key, K. U. Akli, F. N. Beg, H. Chen, R. R. Freeman, A. Link, A. J. Mackinnon, A. G. MacPhee, P. K. Patel, M. Porkolab, R. B. Stephens, and L. D. Van Woerkom. A bremsstrahlung spectrometer using K-edge and differential filters with image plate dosimeters. *Rev. Sci. Instrum.*, 79(10):10E305, 2008. doi: http://dx.doi.org/10.1063/1.2964231. URL `http://scitation.aip.org/content/aip/journal/rsi/79/10/10.1063/1.2964231`.

[88] P. Kirkpatrick. On the theory and use of Ross filters. *Rev. Sci. Instrum.*, 10(6): 186–191, 1939.

[89] B. B. Pollock, D. H. Froula, P. F. Davis, J. S. Ross, S. Fulkerson, J. Bower, J. Satariano, D. Price, K. Krushelnick, and S. H. Glenzer. High magnetic field generation for laser-plasma experiments. *Rev. Sci. Instrum.*, 77(11):114703, 2006. doi: http://dx.doi.org/10.1063/1.2356854. URL `http://scitation.aip.org/content/aip/journal/rsi/77/11/10.1063/1.2356854`.

[90] F. Bitter. The design of powerful electromagnets part iv. the new magnet laboratory at M. I. T. *Rev. Sci. Instrum.*, 10(12):373–381, 1939. doi: http://dx.doi.org/10.1063/1.1751470. URL `http://scitation.aip.org/content/aip/journal/rsi/10/12/10.1063/1.1751470`.

[91] J. Simpson, J. Lane, C. Immer, and R. Youngquist. Simple analytic expressions for the magnetic field of a circular current loop. Technical Report TM-2013-217919, NASA, 2001.

[92] A. Corporaton. Maxwell 3D field simulation. *Release Notes*, 2005.

[93] S. Semushin and V. Malka. High density gas jet nozzle design for laser target production. *Rev. Sci. Instrum.*, 72(7):2961–2965, 2001. doi: http://dx.doi.org/10.1063/1.1380393. URL `http://scitation.aip.org/content/aip/journal/rsi/72/7/10.1063/1.1380393`.

[94] C. Clayton, J. Ralph, F. Albert, R. Fonseca, S. Glenzer, C. Joshi, W. Lu, K. Marsh, S. Martins, W. Mori, A. Pak, F. Tsung, B. Pollock, J. Ross, L. Silva, and D. Froula. Self-guided laser wakefield acceleration beyond 1 GeV using ionization-induced injection. *Phys. Rev. Lett.*, 105:105003, Sep 2010. doi: 10.1103/PhysRevLett.105.105003. URL `http://link.aps.org/doi/10.1103/PhysRevLett.105.105003`.

[95] W. P. Leemans, B. Nagler, A. J. Gonsalves, C. Toth, K. Nakamura, C. G. R. Geddes, E. Esarey, C. B. Schroeder, and S. M. Hooker. GeV electron beams from a centimetre-scale accelerator. *Nat Phys*, 2(10):696–699, Oct. 2006. ISSN 1745-2473. URL `http://dx.doi.org/10.1038/nphys418`.

[96] X. Wang, R. Zgadzaj, N. Fazel, Z. Li, S. A. Yi, X. Zhang, W. Henderson, Y.-Y. Chang, R. Korzekwa, H.-E. Tsai, C.-H. Pai, H. Quevedo, G. Dyer, E. Gaul, M. Martinez, A. C. Bernstein, T. Borger, M. Spinks, M. Donovan, V. Khudik, G. Shvets, T. Ditmire, and M. C. Downer. Quasi-monoenergetic laser-plasma acceleration of electrons to 2GeV. *Nat. Commun.*, 4, June 2013. URL `http://dx.doi.org/10.1038/ncomms298810.1038/ncomms2988`.

[97] F. Albert, B. Pollock, J. Shaw, K. Marsh, J. Ralph, Y.-H. Chen, D. Alessi, a. Pak, C. Clayton, S. Glenzer, and C. Joshi. Angular Dependence of Betatron X-Ray Spectra from a Laser-Wakefield Accelerator. *Phys. Rev. Lett.*, 111(23):235004, Dec. 2013. ISSN 0031-9007. doi: 10.1103/PhysRevLett.111.235004. URL `http://link.aps.org/doi/10.1103/PhysRevLett.111.235004`.

[98] C. Rechatin, X. Davoine, A. Lifschitz, A. Ismail, J. Lim, E. Lefebvre, J. Faure, and V. Malka. Observation of beam loading in a laser-plasma accelerator. *Phys. Rev. Lett.*, 103:194804, Nov 2009. doi: 10.1103/PhysRevLett.103.194804. URL `http://link.aps.org/doi/10.1103/PhysRevLett.103.194804`.

[99] D. H. Froula, C. E. Clayton, T. Döppner, K. A. Marsh, C. P. J. Barty, L. Divol, R. A. Fonseca, S. H. Glenzer, C. Joshi, W. Lu, S. F. Martins, P. Michel, W. B. Mori, J. P. Palastro, B. B. Pollock, A. Pak, J. E. Ralph, J. S. Ross, C. W. Siders, L. O. Silva, and T. Wang. Measurements of the critical power for self-injection of electrons in a laser wakefield accelerator. *Phys. Rev. Lett.*, 103:215006, Nov 2009. doi: 10.1103/PhysRevLett.103.215006. URL `http://link.aps.org/doi/10.1103/PhysRevLett.103.215006`.

[100] B. B. Pollock, J. S. Ross, G. R. Tynan, L. Divol, S. H. Glenzer, V. Leurent, J. P. Palastro, J. E. Ralph, D. H. Froula, C. E. Clayton, K. A. Marsh, A. E. Pak, T. L. Wang, and C. Joshi. Two-screen method for determining electron beam energy and deflection

from laser wakefield acceleration. *Proc. 2009 Part. Accel Conf., Vancouver, Canada*, page A14., May 2009. URL `http://epaper.kek.jp/PAC2009/papers/we6rfp101.pdf`.

[101] X. Artru, V. Baier, R. Chehab, and A. Jejcic. Positron source using channeling in a tungsten crystal. *Nucl. Instrum. Methods Phys. Res., Sect. A*, 344(3):443 – 454, 1994. ISSN 0168-9002. doi: http://dx.doi.org/10.1016/0168-9002(94)90865-6. URL `http://www.sciencedirect.com/science/article/pii/0168900294908656`.

[102] E. P. Alves, T. Grismayer, M. G. Silveirinha, R. A. Fonseca, and L. O. Silva. Slow down of a globally neutral relativistic e^- e^+ beam shearing the vacuum. *Plasma Phys. Controlled Fusion*, 58(1):014025, 2016. URL `http://stacks.iop.org/0741-3335/58/i=1/a=014025`.

[103] M. J.-E. Manuel, C. C. Kuranz, A. M. Rasmus, S. R. Klein, M. J. MacDonald, M. R. Trantham, J. R. Fein, P. X. Belancourt, R. P. Young, P. A. Keiter, R. P. Drake, B. B. Pollock, J. Park, A. U. Hazi, G. J. Williams, and H. Chen. Experimental results from magnetized-jet experiments executed at the Jupiter Laser Facility. *High Energy Density Phys.*, 17, Part A:52 – 62, 2015. ISSN 1574-1818. doi: http://dx.doi.org/10.1016/j.hedp.2014.07.003. URL `http://www.sciencedirect.com/science/article/pii/S1574181814000445`. Special Issue: 10th International Conference on High Energy Density Laboratory Astrophysics.

[104] L. Reimer. *Transmission Electron Microscopy: Physics of Image Formation and Microanalysis*, volume 36 of *Springer Series in Optical Sciences*. Springer Berlin Heidelberg, 4th edition, 1997. doi: 10.1007/978-3-662-14824-2.

[105] R. Egerton. *Physical Principles of Electron Microscopy: An Introduction to TEM, SEM, and AEM.* Springer US, 2005. doi: 10.1007/b136495.

[106] J. Myatt, J. A. Delettrez, A. V. Maximov, D. D. Meyerhofer, R. W. Short, C. Stoeckl, and M. Storm. Optimizing electron-positron pair production on kilojoule-class high-intensity lasers for the purpose of pair-plasma creation. *Phys. Rev. E*, 79:066409, Jun 2009. doi: 10.1103/PhysRevE.79.066409. URL `http://link.aps.org/doi/10.1103/PhysRevE.79.066409`.

[107] W. M. Haynes, editor. *CRC Handbook of Chemistry and Physics.* CRC press, 96 edition, 2014.

[108] J. M. Di Nicola, S. T. Yang, C. D. Boley, J. K. Crane, J. E. Heebner, T. M. Spinka, P. Arnold, C. P. J. Barty, M. W. Bowers, T. S. Budge, K. Christensen, J. W. Dawson, G. Erbert, E. Feigenbaum, G. Guss, C. Haefner, M. R. Hermann, D. Homoelle, J. A. Jarboe, J. K. Lawson, R. Lowe-Webb, K. McCandless, B. McHale, L. J. Pelz, P. P. Pham, M. A. Prantil, M. L. Rehak, M. A. Rever, M. C. Rushford, R. A. Sacks, M. Shaw, D. Smauley, L. K. Smith, R. Speck, G. Tietbohl, P. J. Wegner, and C. Widmayer. The commissioning of the advanced radiographic capability laser system: experimental and modeling results at the main laser output. *Proc. SPIE*, 9345:93450I–93450I–12, 2015. doi: 10.1117/12.2080459. URL `http://dx.doi.org/10.1117/12.2080459`.

[109] Hui Chen, P. Di Nicola, M. Hermann, D. Kalantar, D. Martinez, and R. Tommasini. First NIF ARC target shot results. *Bull. Am. Phys. Soc.*, 60(BAPS.2015.DPP.TO4.4), 2015.

[110] J. Nuckolls and L. Wood. Laser compression of matter to super-high densities: Thermonuclear (ctr). *Nature*, 239:139, 1972.

[111] M. J. Edwards, P. K. Patel, J. D. Lindl, L. J. Atherton, S. H. Glenzer, S. W. Haan, J. D. Kilkenny, O. L. Landen, E. I. Moses, A. Nikroo, R. Petrasso, T. C. Sangster, P. T. Springer, S. Batha, R. Benedetti, L. Bernstein, R. Betti, D. L. Bleuel, T. R. Boehly, D. K. Bradley, J. A. Caggiano, D. A. Callahan, P. M. Celliers, C. J. Cerjan, K. C. Chen, D. S. Clark, G. W. Collins, E. L. Dewald, L. Divol, S. Dixit, T. Doeppner, D. H. Edgell, J. E. Fair, M. Farrell, R. J. Fortner, J. Frenje, M. G. Gatu Johnson, E. Giraldez, V. Y. Glebov, G. Grim, B. A. Hammel, A. V. Hamza, D. R. Harding, S. P. Hatchett, N. Hein, H. W. Herrmann, D. Hicks, D. E. Hinkel, M. Hoppe, W. W. Hsing, N. Izumi, B. Jacoby, O. S. Jones, D. Kalantar, R. Kauffman, J. L. Kline, J. P. Knauer, J. A. Koch, B. J. Koziozjemski, G. Kyrala, K. N. LaFortune, S. L. Pape, R. J. Leeper, R. Lerche, T. Ma, B. J. MacGowan, A. J. MacKinnon, A. Macphee, E. R. Mapoles, M. M. Marinak, M. Mauldin, P. W. McKenty, M. Meezan, P. A. Michel, J. Milovich, J. D. Moody, M. Moran, D. H. Munro, C. L. Olson, K. Opachich, A. E. Pak, T. Parham, H.-S. Park, J. E. Ralph, S. P. Regan, B. Remington, H. Rinderknecht, H. F. Robey, M. Rosen, S. Ross, J. D. Salmonson, J. Sater, D. H. Schneider, F. H. Séguin, S. M. Sepke, D. A. Shaughnessy, V. A. Smalyuk, B. K. Spears, C. Stoeckl, W. Stoeffl, L. Suter, C. A. Thomas, R. Tommasini, R. P. Town, S. V. Weber, P. J. Wegner, K. Widman, M. Wilke, D. C. Wilson, C. B. Yeamans, and A. Zylstra. Progress towards ignition on the national ignition facility. *Phys. Plasmas*, 20(7):070501, 2013. doi: http://dx.doi.org/10.1063/1.4816115. URL `http://scitation.aip.org/content/aip/journal/pop/20/7/10.1063/1.4816115`.

[112] S. Atzeni and J. Meyer-ter Vehn. *The Physics of Inertial Fusion: BeamPlasma Interaction, Hydrodynamics, Hot Dense Matter: BeamPlasma Interaction, Hydrodynamics, Hot Dense Matter*, volume 125. Clarendon Press, 2004.

[113] S. Atzeni, A. Schiavi, and J. R. Davies. Stopping and scattering of relativistic electron beams in dense plasmas and requirements for fast ignition. *Plasma Phys. Controlled Fusion*, 51(1):015016, 2009. URL `http://stacks.iop.org/0741-3335/51/i=1/a=015016`.

[114] D. J. Strozzi, M. Tabak, D. J. Larson, L. Divol, A. J. Kemp, C. Bellei, M. M. Marinak, and M. H. Key. Fast-ignition transport studies: Realistic electron source, integrated particle-in-cell and hydrodynamic modeling, imposed magnetic fields. *Phys. Plasmas*, 19(7):072711, 2012. doi: http://dx.doi.org/10.1063/1.4739294. URL `http://scitation.aip.org/content/aip/journal/pop/19/7/10.1063/1.4739294`.

[115] M. Borghesi, A. Schiavi, D. H. Campbell, M. G. Haines, O. Willi, A. J. MacKinnon, L. A. Gizzi, M. Galimberti, R. J. Clarke, and H. Ruhl. Proton imaging: a diagnostic

for inertial confinement fusion/fast ignitor studies. *Plasma Phys. Controlled Fusion*, 43(12A):A267, 2001. URL `http://stacks.iop.org/0741-3335/43/i=12A/a=320`.

[116] A. J. Mackinnon, P. K. Patel, R. P. Town, M. J. Edwards, T. Phillips, S. C. Lerner, D. W. Price, D. Hicks, M. H. Key, S. Hatchett, S. C. Wilks, M. Borghesi, L. Romagnani, S. Kar, T. Toncian, G. Pretzler, O. Willi, M. Koenig, E. Martinolli, S. Lepape, A. Benuzzi-Mounaix, P. Audebert, J. C. Gauthier, J. King, R. Snavely, R. R. Freeman, and T. Boehlly. Proton radiography as an electromagnetic field and density perturbation diagnostic (invited). *Rev. Sci. Instrum.*, 75(10):3531–3536, 2004. doi: http://dx.doi.org/10.1063/1.1788893. URL `http://scitation.aip.org/content/aip/journal/rsi/75/10/10.1063/1.1788893`.

[117] C. K. Li, F. H. Séguin, J. A. Frenje, J. R. Rygg, R. D. Petrasso, R. P. J. Town, P. A. Amendt, S. P. Hatchett, O. L. Landen, A. J. Mackinnon, P. K. Patel, V. A. Smalyuk, T. C. Sangster, and J. P. Knauer. Measuring E and B fields in laser-produced plasmas with monoenergetic proton radiography. *Phys. Rev. Lett.*, 97:135003, Sep 2006. doi: 10.1103/PhysRevLett.97.135003. URL `http://link.aps.org/doi/10.1103/PhysRevLett.97.135003`.

[118] C. K. Li, F. H. Séguin, J. A. Frenje, M. Manuel, D. Casey, N. Sinenian, R. D. Petrasso, P. A. Amendt, O. L. Landen, J. R. Rygg, R. P. J. Town, R. Betti, J. Delettrez, J. P. Knauer, F. Marshall, D. D. Meyerhofer, T. C. Sangster, D. Shvarts, V. A. Smalyuk, J. M. Soures, C. A. Back, J. D. Kilkenny, and A. Nikroo. Proton radiography of dynamic electric and magnetic fields in laser-produced high-energy-density plasmasa). *Phys. Plasmas*, 16(5):056304, 2009. doi: http://dx.doi.org/10.1063/1.3096781. URL `http://scitation.aip.org/content/aip/journal/pop/16/5/10.1063/1.3096781`.

[119] C. K. Li, F. H. Séguin, J. A. Frenje, J. R. Rygg, R. D. Petrasso, R. P. J. Town, O. L. Landen, J. P. Knauer, and V. A. Smalyuk. Observation of megagauss-field topology changes due to magnetic reconnection in laser-produced plasmas. *Phys. Rev. Lett.*, 99:055001, Aug 2007. doi: 10.1103/PhysRevLett.99.055001. URL `http://link.aps.org/doi/10.1103/PhysRevLett.99.055001`.

[120] R. J. Murphy, G. H. Share, J. G. Skibo, and B. Kozlovsky. The physics of positron annihilation in the solar atmosphere. *Astrophys. J. Suppl. Ser.*, 161:495, 2005.

[121] B. R. Maddox and G. Stone. GE Typhoon FLA7000 software equivalency with Fuji. Private Communication, LLNL Internal Presentation, January 2012.

[122] T. Bonnet, M. Comet, D. Denis-Petit, F. Gobet, F. Hannachi, M. Tarisien, M. Versteegen, and M. M. Aléonard. Response functions of imaging plates to photons, electrons and ^{4}He particles. *Rev. Sci. Instrum.*, 84(10):103510, 2013. doi: http://dx.doi.org/10.1063/1.4826084. URL `http://scitation.aip.org/content/aip/journal/rsi/84/10/10.1063/1.4826084`.